STRUCTURAL ENHANCEMENT UTILIZING SMART MATERIALS: EXPERIMENTS AND APPLICATIONS INVOLVING PIEZOELECTRIC ACTUATORS AND SHAPE MEMORY ALLOYS

A Thesis
Submitted to the Graduate Faculty
of the
North Dakota State University
of Agriculture and Applied Science

By

Thomas Charles Schanandore

In Partial Fulfillment of the Requirements
for the Degree of
MASTER OF SCIENCE

Major Department:
Civil and Environmental Engineering

April 2015

Fargo, North Dakota

North Dakota State University
Graduate School

Title

STRUCTURAL ENHANCEMENT UTILIZING SMART MATERIALS:
EXPERIMENTS AND APPLICATIONS INVOLVING PIEZOELECTRIC
ACTUATORS AND SHAPE MEMORY ALLOYS

By

Thomas Charles Schanandore

The Supervisory Committee certifies that this ***disquisition*** complies with North Dakota State University's regulations and meets the accepted standards for the degree of

MASTER OF SCIENCE

SUPERVISORY COMMITTEE:

Yail (Jimmy) Kim
Co-Chair

Mijia Yang
Co-Chair

Xiangfa Wu

Frank Yazdani

Approved:

4/13/2015
Date

Dinesh Katti
Department Chair

ABSTRACT

Smart materials, within the realm of structural engineering, are mainly used as either sensoric mechanisms or as structural damping mechanisms. For the most part, structural enhancement utilizing smart materials is not seen in main stream structural engineering practices.

Piezoelectric ceramics and shape memory alloys are two smart materials that are explored. In comparison shape memory alloys have far greater actuation strain (2% - 7%) than piezoelectric (0.08% - 0.11%) ceramics.

Piezoelectric actuators are employed as surface actuators. Shape memory alloys are also explored in this manner, but the analysis is taken a step further where shape memory alloys are explored as beam and column retrofit elements.

Because of the low mechanical range of the piezoelectric material, the potential for stress reduction is bound to lower stress applications. The general conclusion for shape memory alloys is that it would be suitable for high stress applications which include main stream steel applications.

ACKNOWLEDGMENTS

I would like to thank my advisors Dr. Yail Kim and Dr. Mijia Yang for all the much appreciated insight and guidance through the research and thesis writing process. Along with my advisors, I would like to thank all my professors with in the College of Engineering that instructed me through my entire college career. Thank you for your vocations as teachers and mentors.

Thank you also to North Dakota EPSCoR for funding my research and to the Civil and Environmental Engineering Department for allowing me to pursue a graduate degree.

Lastly I would thank my parents for instilling in me a desire for learning and for teaching me to do things for the right reasons. Thank you also for raising me in the Catholic faith and teaching me that at every moment in my life God is always near. This has helped me through the difficult and sometimes confusing times during my college career. I love you both so much.

DEDICATION

This thesis is dedicated to my family. To my wife Andrea who supports me always. Andy, your love strengthens me like you wouldn’t believe. To my kids, Noah and Lila, who help to keep me grounded and childlike. I love you all very much.

TABLE OF CONTENTS

LIST OF TABLES

LIST OF FIGURES

LIST OF SYMBOLS

A_f	Austenite finish temperature
A_s	Austenite start temperature
A_{SMA}	Area of SMA retrofit
E_A	Elastic modulus of actuator
$E_{Aust.}$	Elastic modulus of austenite
$E_{Detw.Mart.}$	Elastic modulus of detwinned martensite
E_{Ratio}	Ratio of the elastic modulus of SMA to the elastic modulus of steel
E_S	Elastic modulus of substrate
E_{SMA}	Elastic modulus of SMA
$E_{TwMart.}$	Elastic modulus of twinned martensite
F_{SMA}	Force enacted upon beam bottom flange resulting from the actuation strain of the SMA retrofit
M_A	Moment at beam ends caused by SMA actuation
M_f	Martensite finish temperature
M_s	Martensite start temperature
r_b	Width ratio of actuator compared to width of substrate
r_L	Length ratio of actuator compared to length of substrate
t_s	Thickness of substrate
δ_A	Deflection (camber) in beam caused by the actuation of the SMA retrofit
$\delta_{ANSYS-A}$	Deflection (camber) recorded through ANSYS finite element simulation
$\delta_{ANSYS-Total}$	Total deflection recorded through ANSYS finite element simulation
δ_P	Deflection (downward) caused by external load P

δ_{Total}	Total deflection (sum of δ_A & δ_P)
ε_A	Actuation strain ability of PZT or SMA actuator
ε_{AVG}	Average strain recorded at critical cross section discussed through figure 3.4 and complementary text
ε_L	Detwinning strain length
σ_{AVG}	Average stress recorded at critical cross section discussed through figure 3.4 & complimentary text
σ_{Af}	Austenite finish stress
σ_{As}	Austenite start stress
σ_f	Detwinning finish stress
σ_{found}	Stress found (recorded) at location of recorded stress reduction
σ_i	Stress induction (stress induced upon the substrate with no actuators present) brought about through external loading
$\sigma_{induced}$	Induced stress
σ_{Mf}	Martensite detwinning finish stress
σ_{Ms}	Martensite detwinning start stress
$\bar{\sigma}_R$	Stress reduction percentage
σ_s	Detwinning start stress

CHAPTER 1. INTRODUCTION

1.1. Introduction to Smart Materials

Smart materials are materials that exhibit changes in their mechanical properties when subjected to external stimuli such as stress, temperature, moisture, pH, or electric and magnetic fields. This unique characteristic has allowed for a wide variety of uses for smart materials in recent years especially in the applications of sensorics and mechanical actuation. Some examples of smart materials are shape memory materials (induced by temperature stimuli), piezoelectric materials (induced by voltage stimuli), pH sensitive materials (induced by pH stimuli), chromic materials (stimuli induces change in color), and photomechanical materials (induced by light). These examples can show that a great advantage of smart materials is their response to stimuli that can be subtle and rather undetectable in some situations. This gives smart materials a unique perspective in the area of sensorics.

Most smart materials have the capacity to be implemented as a sensor or an actuator. Smart materials that exhibit both these capabilities are characterized as the so called active materials. Active materials have the special ability to both detect and respond to external stimuli. This ability is referred as the coupling effect. This coupling effect describes the behavior of the active material for which a non-mechanical stimuli produces a mechanical response and reversely, a mechanical stimuli produces a non-mechanical response. This unique two-way response can be seen in shape memory materials, for which temperature is the stimuli, and piezoelectric materials, for which electric voltage is the stimuli.

Within the area of structural engineering, piezoelectric and shape memory materials have been implemented and utilized in applications involving health monitoring (sensorics) and structural damping. There has been much success in the research and development of these materials for structural applications. What is explored in this paper is the capability and effectiveness of piezoelectric and shape memory materials as stress mitigation mechanisms in structural applications. The actuation mechanism of these materials is explored through material testing and finite element simulations.

Piezoelectric and shape memory materials can be compared through what is called mechanical range. The mechanical range describes the range of the actuation strain and actuation stress of the material. Most piezoelectric materials exhibit high actuation stress and low actuation strain. The resulting actuation forces are generated by small strains with large stresses associated. Shape memory materials exhibit high actuation strain and have a large range of actuation stress. Shape memory materials are broken down into shape memory polymers (SMP), magnetic shape memory alloys (MSMA), which have low actuation stress, and temperature shape memory alloys (SMA), which have high actuation stress. The specific materials used for experiment and finite element simulation in this paper are piezoelectric ceramics (PZT) and shape memory alloys (SMA). Mechanical range of active materials is discussed further in chapter 2.

1.2. Scope of Research

The overall scope of this research will involve three areas. The first is the area of smart materials. The scope with-in this study is to understand the material characteristics of piezoelectric actuators and shape memory alloys, as well as the methods and procedures for the electrical powering of these materials. The piezoelectric effect is explored in detail and the material and crystalline makeup of piezoelectric materials is studied to insure the mechanical potential of the material is optimized for the numerical simulation. The pseudoelastic and shape memory effect (SME) is explored for shape memory alloys. These phenomena are considered in the development of the numerical simulations. The second is in the area of composite materials. The scope with-in this study is to understand the mechanics and implementation of composite materials. Specific interests involve the understanding of epoxy matrix characteristics and functions. The third is the area of finite element simulation. The scope with-in this study is to implement numerical simulation of piezoelectric materials and shape memory alloys. The finite element software used for the simulations conducted in this paper is ANSYS Mechanical.

A general understanding of these three areas of study is used to explore the specific application of stress mitigation within the field of structural engineering. The combination of knowledge gathered through the research of smart materials and composite materials and the examination of the behavior of these materials through the finite element method is beneficial to understanding possible structural applications utilizing these materials.

1.3. Objectives

The main objective of this research is to understand the potential and viability of piezoelectric and shape memory materials as stress reduction mechanisms for structural applications. This main objective is supported by three preliminary objectives. The first preliminary objective is to develop an understanding and practical knowledge of smart materials, specifically piezoelectric ceramics and shape memory alloys. This general understanding of these materials includes current applications that these materials have been used for and the history of their development. This objective is supported by Chapter 2 of this thesis.

The second preliminary objective is to develop finite element models involving both piezoelectric actuators and shape memory alloys to support a theoretical analysis of stress reduction. These models are used to represent the basic condition for which stress mitigation is examined. Both models support similar geometry but are implemented using the material models that are supported by ANSYS for piezoelectric and shape memory alloy simulations. As these models are used to develop a theoretical understanding of the specific material behavior, the definition of stress reduction itself is stated in this objective. This objective is supported by Chapter 3 of this thesis.

The third preliminary objective is to gain a real life understanding of the behavior and implementation of smart materials through experimental testing. Experimental testing is conducted with shape memory alloy wires only. The testing of shape memory alloy wires allows for understanding of and comparison with research of shape memory alloys. Through experimental understanding of shape memory alloys, the viability and potential for the material to be used as a stress reduction mechanism can be better seen. Due to time and lack of equipment, experimental testing with piezoelectric material is not conducted. This objective is supported by Chapter 4 of this thesis.

The main objective is supported by Chapter 5 which discusses the possible applications for shape memory alloys. With the support of the preliminary objectives Chapter 5 discusses the main objective in the way of two structural applications for which shape memory alloys may be used. Through the discussion and finite element simulations conducted in Chapter 3, piezoelectric material is deemed to be inadequate for large structural applications. However it is largely studied for the understanding of stress reduction in the parametric study conducted in Chapter 3. The purpose of this paper as a thesis is to explore the main objective and its feasibility in being utilized as a structural mechanism for stress reduction.

1.4. Modeling and Design Considerations

Theoretical modeling is conducted using ANSYS Mechanical finite element software. The piezoelectric and shape memory alloy material models are supported by ANSYS. The materials simulated in these models are representative of actual materials and material properties used for input are determined through experimental results and supplied by manufacturer specifications.

Experimental tests involving shape memory alloy wires are designed following the experiments detailed in the book "Shape Memory Alloys: Modeling and Engineering Applications" (2008) by Dimitris C. Lagoudas. This work shows the specific process that is required to experimentally determine the material properties of shape memory alloys. Data collected from the conducted experiments is used to support material properties for finite element simulations.

1.5. Thesis Outline

This thesis contains six chapters followed by appropriate appendices. The first chapter is a short introduction to smart materials as stress reduction mechanisms. The second chapter is a literature review which summarizes the research conducted on the subject of smart materials, particularly piezoelectric and shape memory materials. The third chapter contains finite element simulations that support the parametric studies performed for piezoelectric actuators and for shape memory alloys. The fourth chapter contains the results of experimental testing conducted with shape memory alloy wires. The fifth chapter looks into two structural applications using shape memory alloys. The sixth chapter is a summary of the main body of the thesis and draws conclusions on the effectiveness and overall merit in using smart materials and piezoelectric materials as stress reduction mechanisms and the practical implementation of the materials.

CHAPTER 2. LITERATURE REVIEW

2.1. Introduction

This chapter summarizes the current research status of smart material used as stress mitigation mechanism in literatures. It is divided into four sections. The first section discusses smart materials as a whole and defines the concept of mechanical range which can be used as a stress mitigation mechanism and a comparison of different smart materials that are made. The second section concentrates solely on piezoelectric materials and discusses its history and development. The section also includes a short glimpse into the different piezoelectric properties and crystalline categories and how they change the functions of piezoelectric materials. Applications of piezoelectric material are also included in the section.

The third section concentrates solely on shape memory alloys. The section includes discussion on the phase transformation of nitinol (NiTi-alloy) and its pseudoelastic behavior. The fourth section includes commentary on common critical stress locations in structures.

2.2. Smart Materials

2.2.1. History and Development

The history of smart materials is short in comparison to conventional engineering materials. They have been promoted in recent years due to the need for technological advancement. One area that smart materials are actively utilized is the area of sensorics. These advanced materials have great benefit when used to detect small amounts of its particular stimuli. As discussed in the introduction each smart material has a particular stimulus that triggers an active change in its material properties. This advantage of detecting small changes in environmental makeup, not normally detectable by the human senses, is of great interest in the area of material science and engineering as a whole.

For some smart materials the history of their development dates back to the 19th century where, in the 1880s, quartz crystals were discovered to generate electric potential when subjected to mechanical pressures. This discovery helps to develop and create what is known today as piezoelectric materials. Shortly after, in 1890s, another material phenomenon called martensite was discovered in steels and eventually led to the discovery of shape memory alloys. This discovery of the martensite transformation sparked great interest and research in the area of metallurgy.

Other smart materials have only been recently developed and pursued, but have long histories of development, are pH sensitive polymers, chromic materials and photomechanical materials. These materials show that there is a wide variety of smart materials with a wide variety of stimuli. With these materials the stimuli are of a non-mechanical nature being pH level, acidity or light, proving that smart materials have a great potential for future application and advancement.

2.2.2. Active Materials

As discussed in the introduction some smart materials can be classified as active materials. These materials exhibit a direct and inverse effect associated with its particular stimuli. For example, piezoelectric materials exhibit the direct piezoelectric effect, which is a change in electric potential when subjected to a mechanical strain, and the inverse piezoelectric effect, which is the change in mechanical strain when subjected to an electric potential. This active characteristic allows for a smart material to be used as both a sensor and a force actuator.

The two active materials that are of interest in this thesis are piezoelectric ceramics and shape memory allows.

Active materials can also be divided into two categories, active materials that exhibit the direct coupling effect and indirect coupling effect. The direct coupling effect refers to those active materials that allow for both the mechanical and non-mechanical component to be used as the input or stimuli. Piezoelectric materials and shape memory alloys exhibit the direct coupling effect.

2.2.3. Mechanical Range

Mechanical range refers to the ranges of actuation stress, actuation strain and the actuation energy density of active materials. Figure 2.1 shows a comparison of several active smart materials and their differences in actuation stress, actuation strain and ultimately their actuation energy density. Actuation energy density is the work outputted per unit volume of material and has the unit (J/m^3). When comparing piezoelectric material and shape memory alloys, Figure 2.1 (referenced from Shape Memory Alloys – Modeling and Engineering Applications by Lagoudas, D.) shows that the range of actuation stress and actuation strain for shape memory alloys are greater than that of piezoelectric materials. Shape memory alloys have an actuation range around 2-7% while piezoelectric ceramics have an actuation strain around 0.05-0.15%. Shape memory alloys also have greater actuation stress than piezoelectric ceramics do. The actuation stress of shape memory alloys is around 100-300 MPa, while piezoelectric actuation stress is around 10-20 MPa.

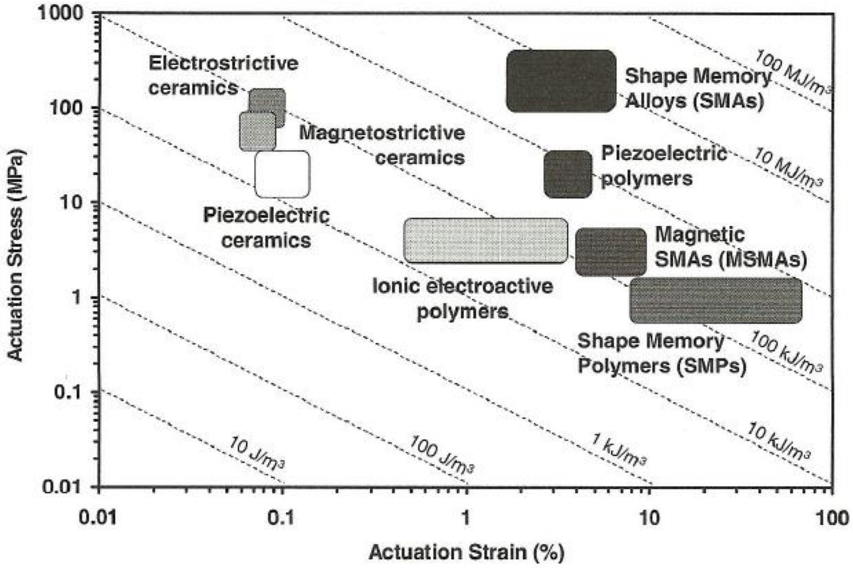

Figure 2.1: Actuation Energy Density of Active Materials

The overall comparison between shape memory alloys and piezoelectric materials is made through the actuation energy density. The average actuation energy density of shape memory alloys is around 10 MJ/m^3 and the average actuation energy density of piezoelectric ceramics is around 0.02 MJ/m^3. When comparing the actuation energy densities it is clearly seen that shape memory alloys have a greater potential for force actuation even while subjected to high stress. This is not to say that piezoelectric materials are of no use. Even though shape memory alloys have greater mechanical capabilities their actuation strain occurs at a non-linear rate and occurs rather quickly at the temperature of transformation. This makes the precision actuation of shape memory alloys difficult. Piezoelectric materials on the other hand have a proportional relationship between its stimuli (electrical voltage) and its change in mechanical strain. This linear actuation strain, combined with its small level of actuation (micro strain), allows piezoelectric materials to be used in nano-positioning applications, where small accurate displacements are need. Some applications of nano-positioning are discussed in this chapter.

Overall the actuation energy density of active materials can best describe and orientate the development of active materials for appropriate applications. In this thesis, both piezoelectric ceramic and shape memory alloys are considered for actuation applications. Actuation energy density can be considered a potential for actuation capabilities. The higher the actuation energy density the higher the predicted actuation capability of the material is. With this said the potential for actuation is greater for shape memory alloys than that for piezoelectric ceramics. The conclusions of this thesis are consistent with this statement.

2.3. Piezoelectric Materials

2.3.1. History and Development

The piezoelectric effect is the reciprocal characteristic of a material that when mechanically loaded produces an electric polarization and reversely, when an electric field is applied to the material a mechanical displacement is produced. Materials that exhibit this unique effect are designated piezoelectric. In order to distinguish between the two, the former has been term the “direct piezoelectric effect” and the latter has been termed the “inverse piezoelectric effect”. The direct piezoelectric effect was discovered by Pierre and Jacques Curie in 1880; where they witnessed electric charges develop on the surface of crystalline material, while subjected to external pressures. This direct effect was the first to be discovered, but a year later, in 1881, MG Lippmann predicted the inverse effect in his work, Principle of the Conservation of Electricity. This was confirmed the same year by Pierre and Jacques Curie in which a simple experiment was able to produce small mechanical displacements while subjected to an electric field.

Some natural occurring materials that were found to have piezoelectric characteristics were crystalline materials such as tourmaline, quartz and topaz. These natural occurring materials produce the piezoelectric effect in small amounts, but through years of research and development many man-made piezoelectric materials have surfaced to serve a variety of applications. These man-made materials are able to exhibit greater effect in terms of displacement and voltage output. There are many types of man-made piezoelectric materials. One common and very well utilized material category is piezoelectric ceramics. Barium titanate ($BaTiO_3$) and lead zirconate titanate ($PbZrO_3$) are two common piezoelectric ceramics that have been in use since the 1950s. These ceramic materials are designated as PZT (Piezoelectric Transducer) material. PZT is the piezoelectric material that is used in the finite element simulations described later in the thesis.

PZT exhibits both behaviors of the piezoelectric effect and can be used in various mechanical practices. By utilizing the direct effect, PZT can be used as a sensor, detecting disturbances in the surrounding environment by relating voltage output to a precise force, pressure or vibration acting on the PZT. The inverse effect can be divided into two types of applications, resonant and non-resonant. Resonant applications use the PZT to create resonant frequencies used in applications involving resonant sensors and radio engineering and non-resonant applications use the PZT mainly as an actuator. Actuator applications include nano-positioning of precision instruments where small and very accurate displacements are needed, vibration control and stress alleviation. The PZT patch implemented as an actuator is the focus of the work conducted in this thesis.

One advantage of PZT ceramics is that the ceramic can be manufactured with a multitude of shapes. Some common actuator shapes are stack, surface, plate, shear and tube actuators. The shape of the PZT is crucial to the application that it is used in. Stack actuators are generally used in applications where large amount of displacement is needed. Surface or plate actuators are used in applications where a force needs to be generated along a surface. Shear actuators are used when two material planes need to move opposite each other in a shearing motion. These three examples show different types of movements generated by the PZT. The movement of the PZT is determined mainly by the manner in which it is designed, but ultimately all movement is associated with the axis of polarization. The axis of polarization acts as a reference along which the crystalline structure aligns itself. The polarized axis and orientation of the PZT is important in understanding the dynamics of the material.

PZT actuation involves the inverse piezoelectric effect where an applied voltage potential produces a mechanical displacement. This displacement is seen as the actuator either contracts or expands. Contraction or expansion of the PZT is controlled by either a positive or negative voltage potential and can be applied to alleviate either a positive or negative stress. This positive and negative voltage potential applied to two opposite surfaces creates polarization within the material when the voltages are applied in a coupling manner, one being positive and the other being negative. Depending on the orientation of the polarized axis of the PZT the coupling voltage potential will either cause a contraction or expansion within the material.

2.3.2. Piezoelectric Properties

2.3.2.1. Anisotropic Stiffness Matrix

Piezoelectric materials exhibit purely anisotropic behavior, meaning that the material property is directional independent. Elastic material has generally 3 symmetrical planes. Piezoelectric material being anisotropic has different material properties in all 3 directional planes. This is different from an isotropic material where all 3 directional planes have the same material properties. PZT can also be referred to as an orthotropic material.

An orthotropic material has the potential to have three different elastic moduli, three different shear moduli, three different Poisson's ratios and, in the case of piezoelectric material, three different electric permittivity constants. The material properties are described in a stiffness matrix [$\mathbf{c}$]. The stiffness matrix is generated through the inverse of its compliance matrix [$\mathbf{s}$]. The elastic modulus (**E**), Poisson's ratio ($\boldsymbol{\upsilon}$) and the shear modulus (**G**) make up nine total components that describe this orthotropic behavior. The subscripts refer to the particular directional plane that they pertain to. Subscript "1" refers to the plane along the x-axis, "2" the plane along the y-axis and "3" the plane along the z-axis.

$$\boldsymbol{C}=\begin{bmatrix} C_{11} & C_{12} & C_{13} & 0 & 0 & 0 \\ C_{21} & C_{22} & C_{23} & 0 & 0 & 0 \\ C_{31} & C_{32} & C_{33} & 0 & 0 & 0 \\ 0 & 0 & 0 & C_{44} & 0 & 0 \\ 0 & 0 & 0 & 0 & C_{55} & 0 \\ 0 & 0 & 0 & 0 & 0 & C_{66} \end{bmatrix} \Rightarrow \boldsymbol{C}^{-1}=\boldsymbol{S}=\begin{bmatrix} \frac{1}{E_1} & \frac{-\nu_{21}}{E_2} & \frac{-\nu_{31}}{E_3} & 0 & 0 & 0 \\ \frac{-\nu_{12}}{E_1} & \frac{1}{E_2} & \frac{-\nu_{32}}{E_3} & 0 & 0 & 0 \\ \frac{-\nu_{13}}{E_1} & \frac{-\nu_{23}}{E_2} & \frac{1}{E_3} & 0 & 0 & 0 \\ 0 & 0 & 0 & \frac{1}{G_{23}} & 0 & 0 \\ 0 & 0 & 0 & 0 & \frac{1}{G_{31}} & 0 \\ 0 & 0 & 0 & 0 & 0 & \frac{1}{G_{12}} \end{bmatrix}$$

2.3.2.2. Piezoelectric Coefficient Matrix

The piezoelectric matrix is the governing matrix that expresses, as the name suggests, the piezoelectric effect and the properties pertaining to it. There are three components that make up the matrix and they each correspond to one of the three types of mechanical outcomes of the piezoelectric effect. These three mechanical actions, as discussed before, are displacement parallel to the polarized axis 3 ($\boldsymbol{e}_{33}\ or\ \boldsymbol{d}_{33}$), displacement perpendicular to the polarized axis 3 ($\boldsymbol{e}_{13}\ or\ \boldsymbol{d}_{31}$) and shearing rotation perpendicular to the polarized axis 3 ($\boldsymbol{e}_{42}\ or\ \boldsymbol{d}_{15}$).

The piezoelectric matrix can be expressed in two ways. The stress form (**e**) or the strain form (**d**). The strain form is the most common way that piezoelectric properties are given. The strain form (**d**) is referred to as the piezoelectric strain coefficients and has units of coulombs per newton (**C/N**). The PZT strain coefficients give a direct relationship between electrical gain in the system and its corresponding mechanical force.

Another way to look at the strain coefficient is as an electrical strain, an electrical force per mechanical force. In the same way the PZT stress coefficient (**e**) can be viewed as an electrical stress, for when the strain coefficient ($\mathbf{d^T}$) is multiplied by the compliance matrix(**c**) the resulting units become coulombs per meter squared ($\mathbf{C/m^2}$), an electrical force distributed over an area. Both the electrical stress and strain coefficients combined with the mechanical material properties, supports a unique occurrence where both mechanical and electrical stress and strain can be seen in the PZT system.

$$\boldsymbol{PZT\ Stress\ Matrix = e = cd^T =} \begin{bmatrix} \mathbf{0} & \mathbf{0} & \boldsymbol{e_{13}} \\ \mathbf{0} & \mathbf{0} & \boldsymbol{e_{13}} \\ \mathbf{0} & \mathbf{0} & \boldsymbol{e_{33}} \\ \mathbf{0} & \boldsymbol{e_{42}} & \mathbf{0} \\ \boldsymbol{e_{42}} & \mathbf{0} & \mathbf{0} \\ \mathbf{0} & \mathbf{0} & \mathbf{0} \end{bmatrix} \boldsymbol{C/m^2}$$

$$\boldsymbol{PZT\ Strain\ Matrix = d^T = ec^{-1} =} \begin{bmatrix} \mathbf{0} & \mathbf{0} & \boldsymbol{d_{31}} \\ \mathbf{0} & \mathbf{0} & \boldsymbol{d_{31}} \\ \mathbf{0} & \mathbf{0} & \boldsymbol{d_{33}} \\ \mathbf{0} & \boldsymbol{d_{15}} & \mathbf{0} \\ \boldsymbol{d_{15}} & \mathbf{0} & \mathbf{0} \\ \mathbf{0} & \mathbf{0} & \mathbf{0} \end{bmatrix} \boldsymbol{C/N}$$

2.3.2.3. Piezoelectric Permittivity Matrix

The electrical permittivity of PZT can be analyzed when the PZT system is considered as an electrical component. A PZT actuator has a capacitance that corresponds to the dimensions and permittivity of the material. Permittivity ($\boldsymbol{\epsilon}$) describes a materials ability to transmit an electric field through a medium. Stated differently, it is the amount of resistance met when forming an electric field in a medium. With this said, it is the permittivity that governs the rest of the piezoelectric properties within a material. The general piezoelectric formulation for permittivity is expressed by the dielectric constant (K). The K constant is the ratio of the permittivity of the material ($\boldsymbol{\epsilon}$) to the permittivity of free space ($\boldsymbol{\epsilon_0} = 8.9 \times 10^{-12}$farad per meter (**F/m**)).

The capacitance can then be calculated by the following equation that relates the dimensions and permittivity of the material. The capacitance of a PZT system is dependent on the size of the actuator. The simplified form can be expressed, when canceling the free space permittivity.

$$\boldsymbol{C = \frac{K\epsilon_0 A}{t}},$$

$$\boldsymbol{where: K = \frac{\epsilon}{\epsilon_0}\ , A = Area\ of\ actuator\ , t = thickness\ of\ actuator}$$

$$\boldsymbol{C = \frac{\epsilon A}{t}}$$

PZT has the capability to store electric energy; hence it can act as a capacitor. The capacitance of the system plays a role in the functionality of the piezoelectric actuator. The capacitance can be used to relate between the strain coefficient (**d**) and what is call the voltage coefficient (**g**). The voltage coefficient is another property that is given as basic PZT material properties and has units of volt meters/Newton (Vm/N). As seen in the equations below the strain coefficients can be found by multiplying the voltage coefficients by the permittivity of the material.

$$\boldsymbol{d_{33} = K_3\epsilon_0 g_{33} = \epsilon_{33} g_{33}}$$

$$\boldsymbol{d_{31} = K_3\epsilon_0 g_{31} = \epsilon_{11} g_{31}}$$

Electrical Permittivity and voltage coefficients also are directionally independent. Electrical permittivity generally has two directions of electric flow, parallel to the polarized axis 3 and perpendicular to the polarized axis 3. When parallel to the polarized axis the permittivity is different than the permittivity when perpendicular to the polarized axis. Parallel flow is associated with normal directional expansion and contraction along axis 3. Perpendicular flow is associated with shear and normal directional expansion and contraction pertaining to axes 1 and 2.

$$\boldsymbol{Permittivity = \epsilon = \begin{bmatrix} \epsilon_{11} & 0 & 0 \\ 0 & \epsilon_{11} & 0 \\ 0 & 0 & \epsilon_{33} \end{bmatrix}}$$

2.3.3. Applications of Piezoelectric Materials

Piezoelectric materials, having a longer history of development than most smart materials, have been utilized in many applications throughout the last century. One of the first applications of piezoelectric material was sonar. The First World War prompted the development of an instrument that could detect submarines. The resonant ability of piezoelectric material was able to emit a resonant chirp underwater for which the time of the returning echo was measured. This allowed for the detection of objects along the sea floor. Some other early applications which utilized piezoelectric or, at that time, quartz crystals were radio engineering and ultrasonics. These applications have been improved over the years and have become common in the modern world. Many common consumer products utilize piezoelectric materials, such as: modern ultra sound equipment in hospitals, depth finders for marine vehicles, ignition starters for vehicles and disc drives.

One very common modern application for piezoelectric material is nano-positioning applications. These are applications that require small and accurate displacements. Some applications include electronic precision microscopes and linear motors. As discussed before the actuation ability of piezoelectric materials occur at the nano scale. Low voltage potential can be used to induce a displacement of several nanometers, which can aid the exact positioning of precision instruments.

Within the realm of structural engineering, there has been development of applications utilizing piezoelectric materials. The most common use of piezoelectric material is as a sensor. This application area is called structural health monitoring. Within the area of structural health monitoring there are many types of sensing materials that are used, but piezoelectric materials offer a unique ability. The direct coupling characteristic of piezoelectric materials offers a large range of frequencies for resonant actuation. This ability to detect fine changes in vibrations provides many benefits. Evaluation of the dynamic integrity of bridges and structures is one important application.

Another application that is being researched is the integrity of concrete. Piezoelectric actuators are embedded into concrete and act as both sensors and actuators. The actuation of the piezo creates energy transfer through the concrete as vibrations. These vibrations are detected by the surrounding piezo acting as sensors. The energy transferred through the concrete is monitored and compared as the concrete is subjected to degradation through impact. As the concrete begins to deteriorate and crack the vibration energy felt by the piezo sensors diminishes. Without taking core samples the structural integrity of the concrete can be determined.

Structural damping is also a utilized application for piezoelectric actuators. Some structural materials that are created to be light weight are often susceptible to vibrations. Piezoelectric actuators have been used to act as a damping point on these structures. When a piezoelectric actuator is powered it acts a stiffener. The actuators place in series or at connection point of a structural system offers as a way not only to diminish vibrations but to diminish them rather quickly.

Structural applications involving piezoelectric actuators as components for increasing structural performance are few. This thesis will examine the effect that piezoelectric actuators have on reducing stress and its viability of being used to increase structural performance.

General knowledge and understanding of piezoelectric functions and characteristics is taken from the following referenced materials: Claeyssen, et al. (2007), Gaul, et al. (2007), Kamada, et al. (1197), Newman (1992), Nguyen-Van, et al. (2008), Piefort (2001), Song, Ma and Li, (2006), Tichỳ, et al. (2010), Tripathi, Prashant and Gangadharan (2012) and Bhalla and Soh (2003).

2.4. Shape Memory Alloys

2.4.1. History and Development

In the 1890s Adolf Martens discovered the martensitic transformation in steel as it cools. The higher temperature phase, called austenite, transforms into the martensite phase as the steel cools. The rapid cooling of steels was used to trap carbon atoms in the material which allowed for stronger metals. This discovery led to a rapid advancement of metallurgy in the early part of the 20th century. It wasn’t until 1960s that the reversible martensitic transformation of certain metal alloys was discovered.

In 1963 William Buehler and Frederick Wang discovered the reversible martensitic transformation when experimenting with a nickel titanium alloy (NiTi) at the Naval Ordnance Laboratory (NOL). What they discovered was that NiTi was able to be deformed under loading and when heated the alloy would recover its original shape. This effect was called the shape memory effect (SME). They name the alloy “NiTiNOL” after the elements it was comprised of and the laboratory it was discovered at. From this discovery the development of shape memory alloys began.

Shortly after, several other alloys that exhibited the shape memory effect were discovered. Copper based alloys such as copper zinc (CuZn) and copper aluminum (CuAl) were developed and showed the same shape memory effect but showed less hysteresis between the loading and unloading paths. The two most common forms of the cooper based alloys are CuZn and CuAl and from these there are a multitude of third element alloys that have been developed. Also developed were iron based alloys, allowing for higher transformation temperatures. Low temperature transformations were seen in Cobalt based alloys that exhibit transformation temperatures that are below 0℃. Through the development of the above shapes memory alloys a new shape memory alloy that exhibits magnetic capabilities was also discovered. This alloy was (NiMnGa) and was the first kind of the magnetic shape memory alloys (MSMA). Since this initial discovery there has been several other alloys that exhibit the magnetic shape memory effect including iron, cobalt and nickel based alloys.

Concentrating on NiTi based shape memory alloys, there are many alloys that are based on the original “NiTiNOL” design, but what was discovered was that varying the concentration of Ni to Ti and also combining other elements such as Cu, gave very different properties to the shape memory effect of the material. A concentration of $Ni_{50\%}$ and $Ti_{50\%}$ is the basic “NiTiNOL” design and it has a martensite temperature around room temperature and the transformation temperature or austenite finish temperature is around 80℃ to90℃. It was discovered that by varying this concentration by half a percent and supplying special heat treatments a significant drop in the transformation temperatures were accomplished. A concentration of $Ni_{50.5\%}$ and

$Ti_{49.5\%}$ achieved a martensite final temperature of well below $0℃$ and an austenite final temperature around $40℃$ to$50℃$. Also the addition of a third element into the design, such as zirconium or platinum, achieved high transformation temperatures well into and beyond $200℃$ and $300℃$ ranges.

Any application that utilized the shape memory effect, takes advantage of two functions. These functions are the phase transformation and the pseudoelastic behavior of SMA. The phase transformation function deals with the shape memory effect of initially deformed SMA. This function can act as a damage repair or as an actuation mechanism. The pseudoelastic function is the non-linear behavior of the material under loading. Pseudoelasticity also deals with the hysteresis of the unloading path. This pseudoelastic function usually operates the SMA above its austenite finish temperature in order to gain full and immediate recovery detwinning strains.

2.4.2. Shape Memory Effect

The shape memory effect is realized in the shape memory cycle. The shape memory cycle begins with the twinned martensite phase and when subjected to loading or impact the phase changes to the stress induced detwinned martensite phase. It is from this phase that an introduction of a temperature above the high temperature transformation transforms the detwinned martensite into austenite. Once full transformation to austenite is achieved and the temperature is decreased below the low temperature transformation, the material transforms back into twinned martensite and the full shape memory effect is achieved.

The shape memory effect supports a high level of strain recovery. Typical strain recovery ranges from 1 to 7%. Even with high levels of strain recovery there is still permanent plastic deformation of the SMA under loading. This permanent deformation brings to light a fatigue factor for which the deformation and potential shape recovery cannot be accurately predicted. In order to fix this uncertainty, a training of the SMA is implemented. This training of the SMA involves the cyclic loading beyond martensite detwinning followed by the shape recovery of the SMA. The cycling allows for all the potential permanent plastic deformation to occur. After sufficient training of the SMA a full recovery of the detwinned martensite is achieved.

Actuation of shape memory alloys does not only happen when the material is in the detwinned martensite phase. Twinned martensite when brought above the transformation temperature can achieve actuation since the shifting of the atoms from martensite to austenite still occurs. The strain of transformation from twinned martensite to austenite is less than that of the strain transformation from detwinned martensite to austenite.

The effectiveness of SMA as an actuation mechanism is dependent of the cross sectional area of the SMA in the direction of actuation. The shifting of atoms when martensite transforms to austenite is consistent no matter the amount of material that is being transformed. The only factor that changes when the amount of material increases is the amount of energy needed to bring about a temperature change through the entire material. As the cross sectional area of the SMA increases so does the induced stress caused by the shape memory effect. The force caused by the actuation of a wire of SMA is significantly lower than the force caused by the actuation of a large block of SMA.

The induction of the shape memory effect through temperature stimuli can be done in two ways. The first way is by changing the temperature of the surrounding environment. The second is to electrically induce temperature change. The latter of the two is the fastest way to induce forward temperature change in SMA material. SMA is highly resistive and can build up temperatures of 120℃ in 1 second when subjected to high electrical current. Because of its high electrical resistance, the electrical powering of SMA has its limits. The powering of a large block of SMA may not be feasible due to high voltage required to overcome the resistance of the entire block of SMA.

2.4.3. Phase Transformation

There are three forms of NiTi shape memory alloys. These three forms are twinned martensite (M^t), detwinned martensite (M^d) and austenite (A). The two martensite variants are associated with low temperature transformation and austenite is associated with high temperature transformation. Each form has a particular arrangement of the Ni and Ti element and each arrangement is mechanically different than the other. Figure 2.2 shows the three forms of NiTi.

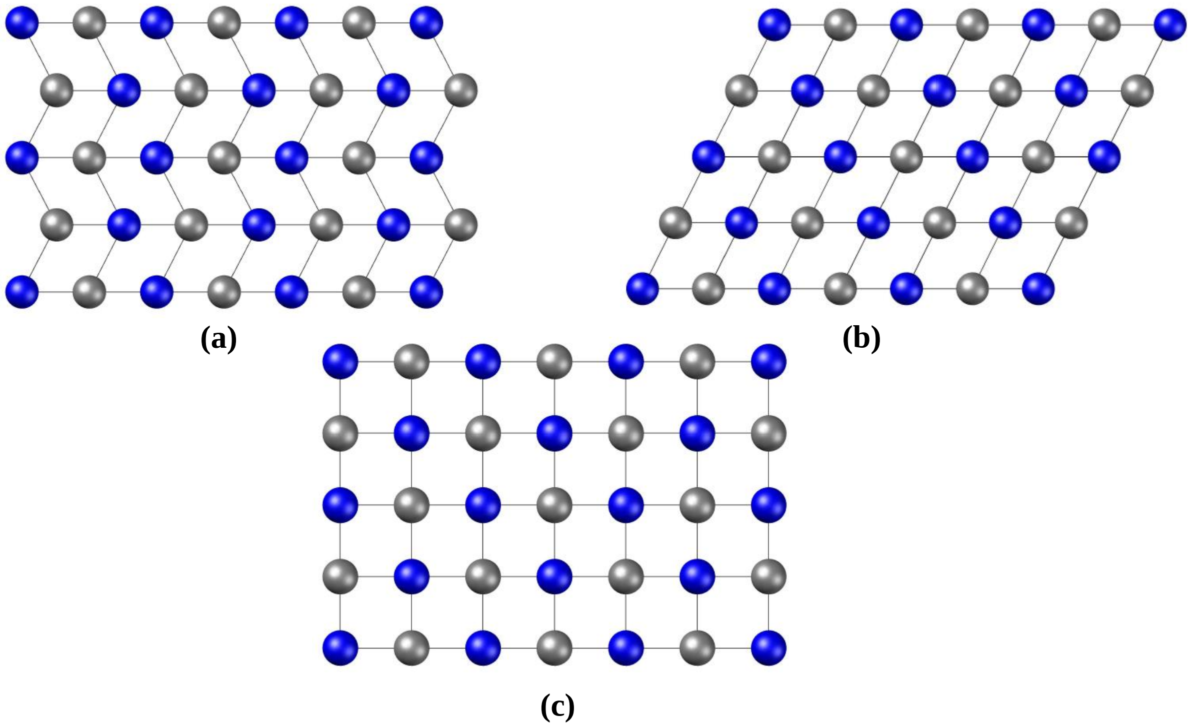

Figure 2.2: NiTi (SMA) Transformation Forms: (a) Twinned Martensite, (b) Detwinned Martensite, (c) Austenite

There are four types of phase transformations associated with the three forms of NiTi shape memory alloys. The first is the stress induced transformation from twinned martensite to detwinned martensite. This transformation is referred to as ‘detwinning’ and supports long plastic strain of the SMA. The second is the transformation from detwinned martensite to austenite through heating the material beyond the high transformation temperature. The third is the transformation of austenite to twinned martensite achieved through cooling the material to the low transformation temperature. The fourth is the transformation of austenite to detwinned martensite. This special transformation is achieved through high levels of stress while the material is above the high transformation temperature.

The phase transformations of any SMA material are described by four temperatures. These temperatures designate when transformations between austenite and martensite begin and end. As the SMA material is heated the forward transformation from martensite to austenite begins at the austenite start temperature (A_s) and is fully transformed into austenite at the austenite finish temperature (A_f). As the SMA material is cooled back down to its original temperature the backward transformation from austenite to martensite begins at the martensite start temperature (M_s) and is fully transformed into martensite at the martensite finish temperature (M_f).

The forward and backward transformations do not follow the same path. Upon cooling of the material the backward transformation exhibits hysteresis. Martensite transformation temperatures from the backward transformation are lower than the austenite transformation temperatures and retain the strains made through the higher temperature forward transformation at lower temperatures. The strain that is achieved through the forward shape memory effect can be referred to as thermal strain (ε_T). This forward and backward transformation can be seen in Figure 2.3.

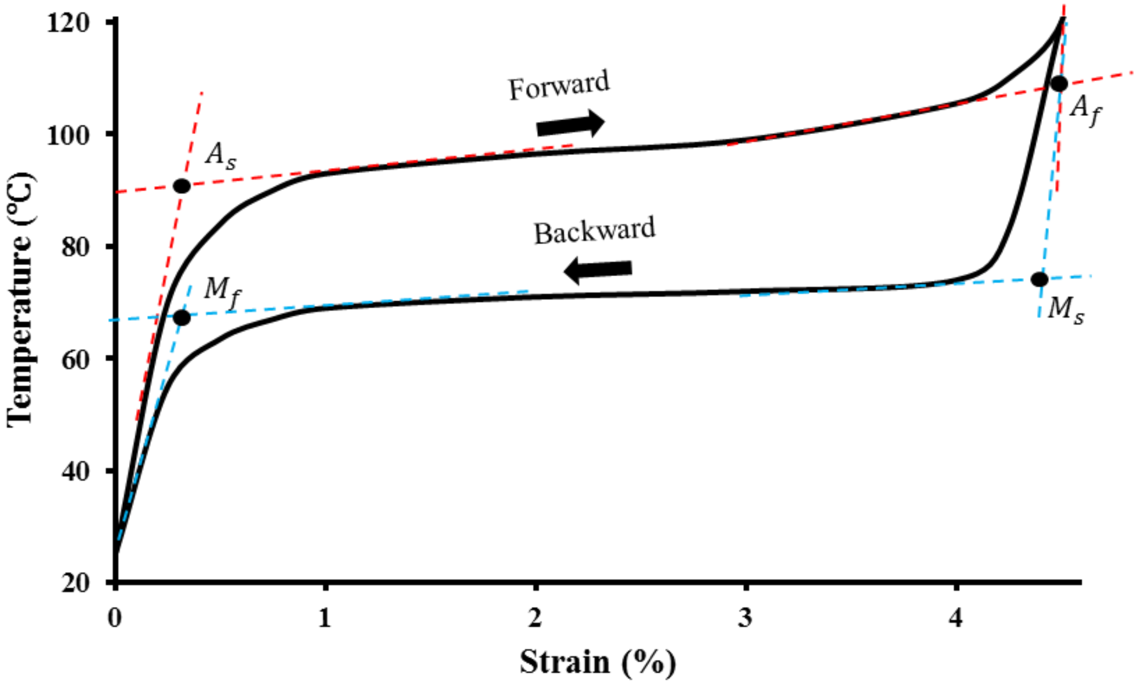

Figure 2.3: Forward and Backward Transformations of the Shape Memory Effect

2.4.3.1. Twinned Martensite ⇒ Detwinned Martensite

The transformation from twinned martensite to detwinned martensite is achieved through stressing NiTi (SMA) beyond the detwinning start stress (σ_s) and the detwinning finish stress (σ_f). The σ_s is the point at which the twinned martensite arrangement of the NiTi begins to displacement. The σ_f is the point at which the twinned martensite arrangement is completely displaced and has been transformed into the detwinned martensite state. The stress-strain path from σ_s to σ_f has large plastic strains and is called “detwinning”. The plastic strain achieved through the detwinning process remains and is the deformed state of the NiTi (SMA). Figure 2.4 shows the detwinning of martensite at room temperature.

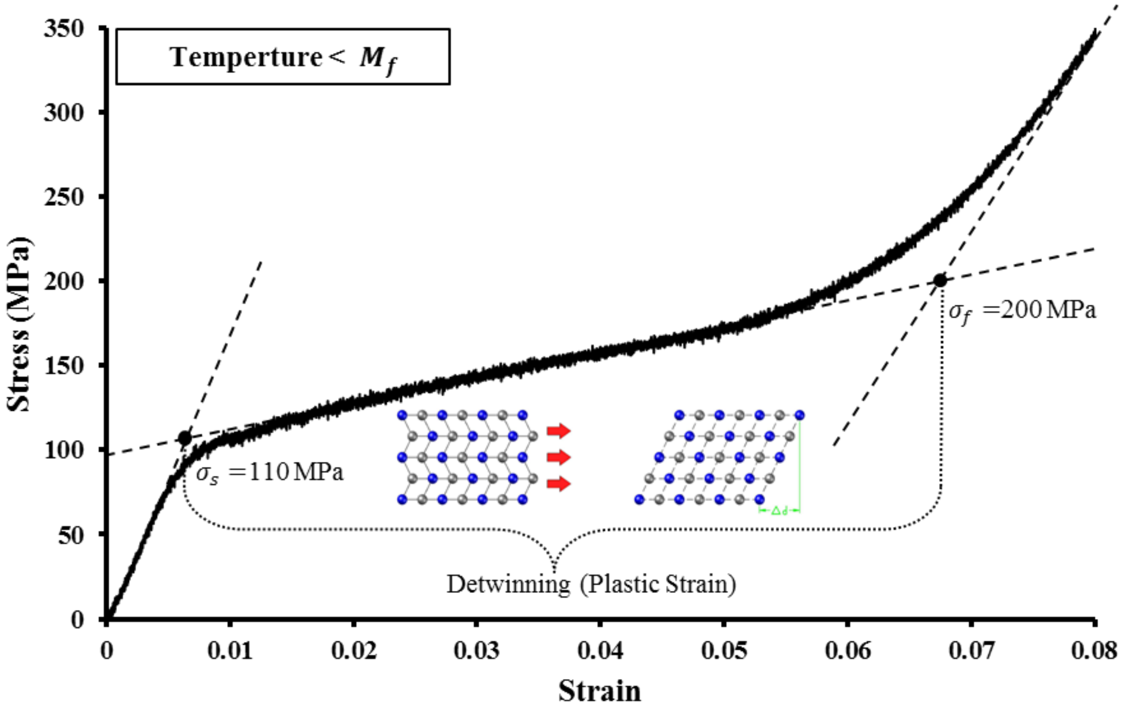

Figure 2.4: Martensite Detwinning

2.4.3.2. Detwinned Martensite ⇒ Austenite

The transformation from detwinned martensite to austenite begins when the NiTi (SMA) is heated to the austenite start temperature. At this point the tetragonal arrangement of martensite begins to transform into the cubic arrangement of austenite. This transformation not only retains the twinned martensite variant but also transforms the crystalline structure of the NiTi (SMA). This type of transformation is the shape memory effect of the deformed state of the material. The strain recovered by the transformation may be more than 100%. This is due to the fact that the original form was twinned martensite and the transformation to austenite supports a more compact structure than twinned martensite and hence supports more strain through the shape memory effect. Figure 2.5 shows this transformation from detwinned martensite to austenite.

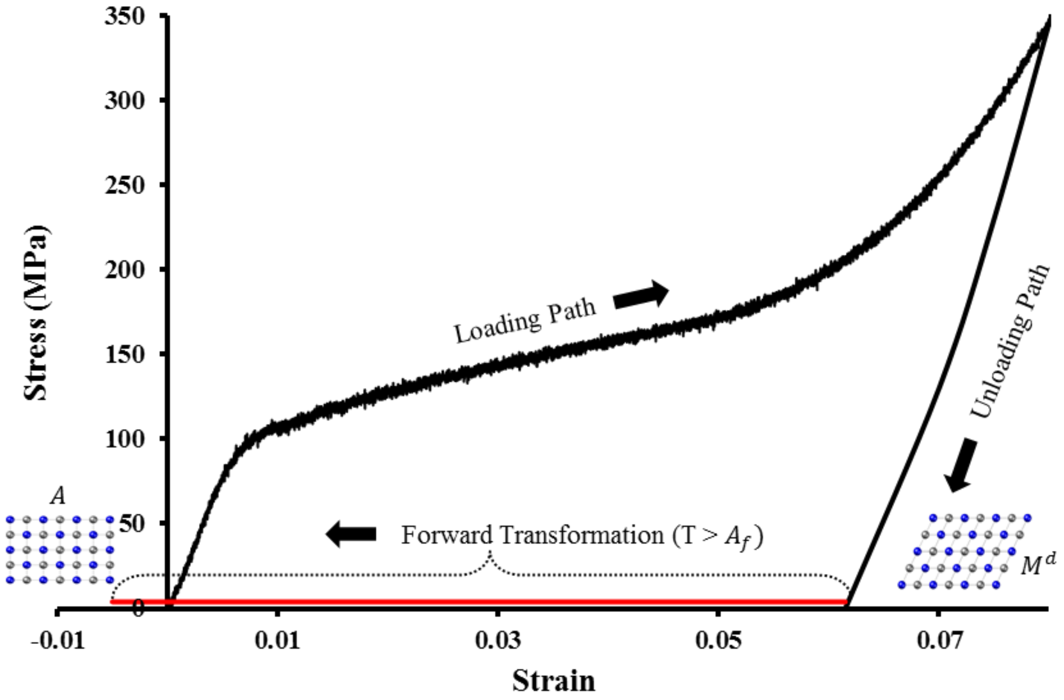

Figure 2.5: Detwinned Martensite to Austenite

2.4.3.3. Austenite ⇒ Twinned Martensite

The transformation from austenite to twinned martensite is achieved through the backward transformation. This happens when the currently heated and austenitic NiTi (SMA) is cooled below the martensite finish temperature. When this happens the strain recovered by the austenite phase is not completely retained. This is due to the transition from the cubic austenite structure to the tetragonal martensite structure. This transformation completes the shape memory cycle from deformed state to original state. The main difference between the martensite phase and the austenite phase is the mechanical capability. Figure 2.6 shows the transformation from austenite to twinned martensite.

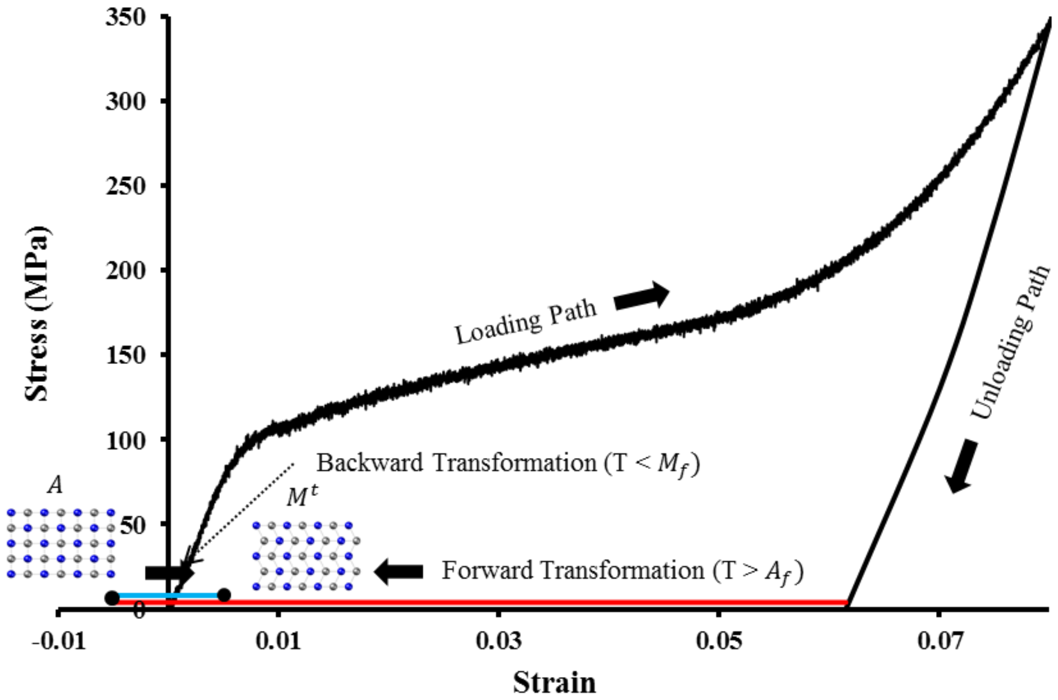

Figure 2.6: Austenite to Twinned Martensite

2.4.3.4. Austenite ⇒ Detwinned Martensite

The transformation from austenite to detwinned martensite is a special condition upon which the NiTi (SMA) in the austenite form can actually be detwinned. As discussed before the detwinning of NiTi (SMA) involves stressing the material beyond the detwinning start stress. Twinned martensite to detwinned martensite can be achieved through rather low stress levels, but austenite, having a higher stiffness than martensite, requires more stress to be detwinned. This detwinning for deforming of the initial austenite phase is associated with the pseudoelastic characteristics of shape memory alloys. Figure 2.7 shows the transformation from austenite to detwinned martensite.

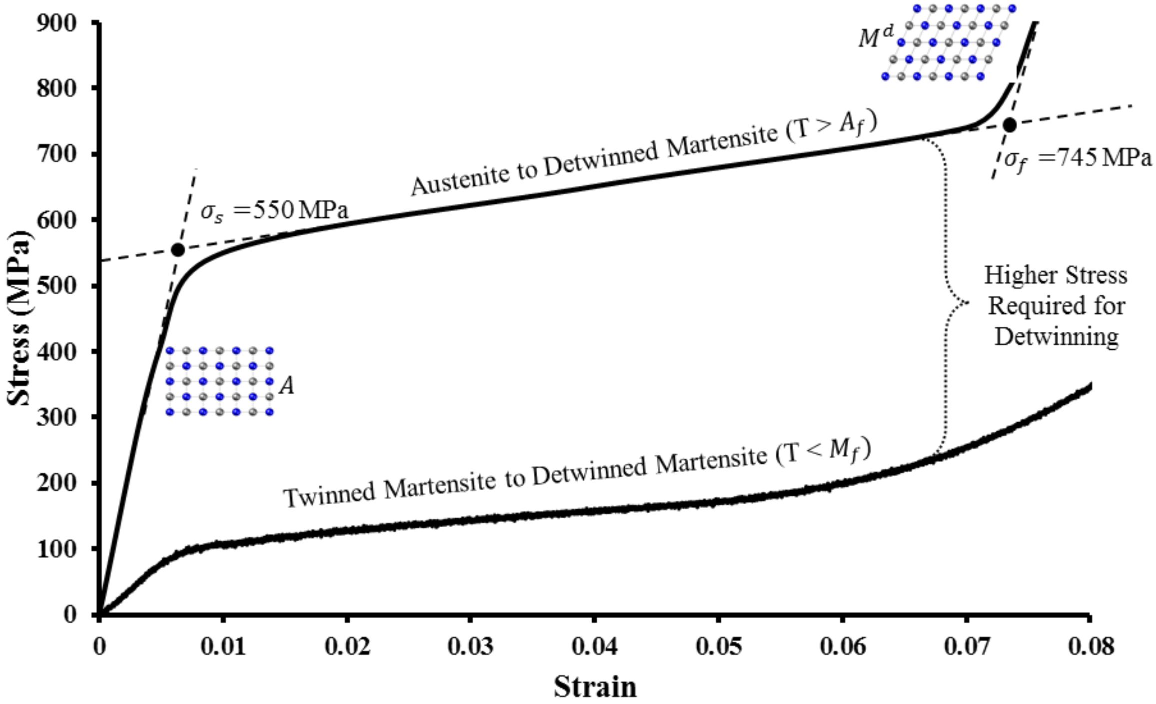

Figure 2.7: Austenite to Detwinned Martensite

The transformation from martensite to austenite and austenite to martensite is dependent on stress and temperature. As the stress on the material increases so do the temperatures of transformation and reversely as the temperature of the material increases so does the stress required for detwinning. This increase of both stress and temperature is a linear relationship upon which the mechanical and thermal loading paths can be combined to achieve the desired phase change of NiTi (SMA). It is here that the pseudoelastic behavior of NiTi (SMA) can be examined. Figure 2.8 is a phase diagram that illustrates the phase transformation of martensite (both variants) and austenite through mechanical and thermal loading.

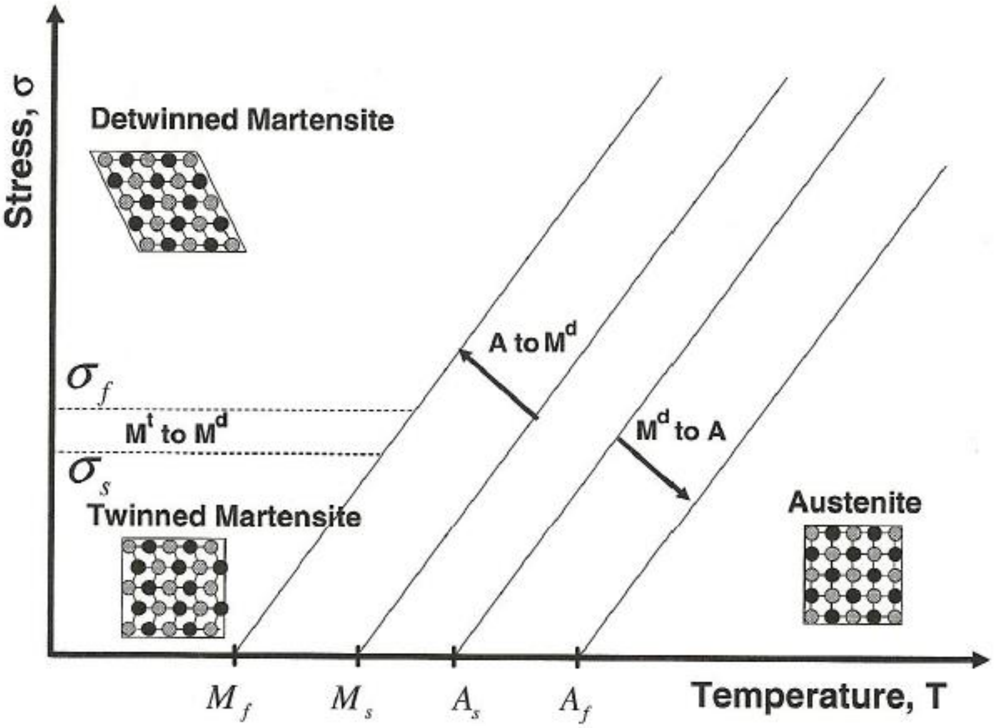

Figure 2.8: Phase Diagram for Martensite Variants and Austenite

2.4.4. Applications of Shape Memory Alloys

Since the discovery of SMA (Nitinol) in 1963 the development of SMA based applications has been strongly pursued and still increases today given the ever increasing creation of application specific alloys. The versatility of shape memory alloys gives greater potential for practical applications within a multitude of industries.

Shape memory alloys have their employ with in the medical field, being used anywhere from orthodontic (dental) applications to cardiovascular stents. Once again the versatility of the material, in being able to be made from almost an endless array of alloy variations, helps to maintain the shape memory mechanism while providing the appropriate material type for the given use. For example, shape memory alloys are used for cardiovascular stents where the expanding characteristic of the material is used to support major blood vessels in the body.

Materials that are placed within the body must be carefully selected because the biocompatibility of foreign materials within the body is very important. Shape memory alloys (specifically NiTi) combined with special titanium nickel surface coatings produce highly biocompatible stents. Also, along with the biocompatibility, the self-expanding ability of the material is especially suited for this particular application.

Another area of application is the aerospace industry. A typical application of shape memory alloys is the variable geometry chevron used in plane jet turbine engines. These SMA comprised chevrons, which are located on the exterior of the engine, are used to decrease the noise output of the engine. At low elevations the chevron contracts inward. The propulsion of the air though the turbine creates extremely load noise for which the chevrons, when contracting inward, help to mix the air flow and decrease the noise output. At higher elevations, where noise is not required to be lessened, the colder air allows the chevrons to relax which also helps engine performance.

Shape memory alloys already have their use in many kinds of industries including electronics, automotive, mechanical, examples mentioned above and many others. Within the realm of structural engineering there are limited applications for which shape memory alloys are employed, most of them being experimental. The majority of shape memory alloy applications in the area of structural engineering have to do with and concentrate on damping of structures. For the damping of structures shape memory alloys are applied to key structural elements of the structural system of a building. Some of these key locations are: connection points, where vibration forces concentrate whole they travel through the building, building bracing elements and framing/foundation anchorage locations. Some specific references showing these particular applications are summarized next.

DesRoches and Delemont (Year 2002) described a rather practical application for reducing the seismic vulnerability of bridges using shape memory alloy restraining bars. In their research, simply supported bridges subjected to seismic loading are retrofitted with shape memory alloy restraining bars for the purpose of decreasing the translation at roller supports of simply supported bridge bearing locations. Here, the shape memory alloys restraining bars replace traditional steel rod restraining measures. The results of the paper find that the shape memory alloy restraining bars are more effective in preventing large translations in the bridge. The shape memory alloys are deemed more effective because of its ability to remain elastic while undergoing large deformations and help to dissipate energy at the bridge roller supports because of its superelastic properties.

Ocel, et al. (2004) studied steel beam column connections using Shape Memory Alloys; while El-Tawil and Ortega-Rosales (2004) researched Prestressing Concrete Using Shape Memory Alloy Tendons. Both of them discussed structural member retrofitted with or reinforced with shape memory alloys. The steel beam-column application involves the attachment of 4 large diameter shape memory alloy bars that are used as a primary moment transfer mechanism (through actuation) when subjected to elevated temperatures. The concrete application involves the casting in of shape memories alloy tendons of which are pre-strained and after the concrete is fully cured the tendons are heated to induce the shape memory effect which results in an internal pre-stressing of the concrete. Both these applications have significant results showing that there is beneficial pre-stressing applied to the structural members.

In Chapter 3 and in Chapter 5 of this thesis, there can be seen some applications similar to these applications referenced and research here. The applications especially in Chapter 5 show structural beams and columns retrofitted with shape memory alloy for the purpose of increasing structural bending and compression capacity of the members.

General knowledge and understanding of shape memory alloys is taken from the following referenced materials: Lagoudas, et al. (2008), Li (2011), Cai, et al. (2003), Maji and Negret (1998), Song, Ma and Li (2006), Song, Kelly and Agrawal (2006) and Terriault, Viens and Brailovski (2006).

2.5. Stress Mitigation

All structural design and analysis is dependent on the understanding and care taking of stress with-in any given structural system. Whether it is bending stress, axial stress, torsional stress or combined stress, the formation of mechanical stress controls all structural designs.

Stress with-in a structural system can be compared to the flow of water. For example, when considering gravity loads on a structure, the load path is typically the fastest route from the point of application to the nearest point of bearing. The bearing point typically being the nearest foundation element of the structure must be able to withstand and transfer the collected loads to the earth. As this is true, it is also true that along the load path all structural elements, be it main framing members or structural components, must be able to withstand the load being transferred through the system. With this consideration in mind, typical critical stress locations in a structural system can be pin pointed.

2.5.1. Critical Stress Locations in Structures

2.5.1.1. Main Framing Members

The design of main framing members such as joists, beams and girders, is typically controlled by bending stress. Bending stress in these conditions, are concentrated at the outer extents of the given section, be it compression or tension stress. Extreme bending stress will either cause yielding or buckling of the section. AISC design of flexural members takes into account the effect that the unbraced length of a section has on flexural capacity. Typically the longer the unbraced length of a section the less amount of potential yield strength is used. On the other hand the shorter the unbraced length the greater the amount of potential yield strength can be utilized. Either way the bending stress in the section must be understood and controlled in order that the load can be transferred successfully through the member to adjacent structural elements.

2.5.1.2. Structural Components

Structural components, comprising of connections and load transfer members, such as braces and struts, have their own unique considerations when it comes to stress. The structural connection element's main purpose is to successfully transfer the load from upstream members to downstream members. This is typically seen through the beam-to-column connection scenario. Usually this transfer is simple shear transfer, for which the shear at the end of the beam is transferred to the column and continues down the column as axial load. Typically connections are designed in such a way that there is no bending on the connection interface. The pinned-pinned beam scenario that this promotes causes the critical bending to occur at the mid-span of the beam rather than at the connection.

For lateral design however, sometimes the structural design incorporates resolving the lateral loads at the connection point. This brings about the application of the moment connection. A moment connection is designed to resolve the bending stress of the framing members at the connection point. This helps to stiffen the local framing of the structure in that area to support lateral support. This, in some cases, creates large connections for which large amounts of stress must be resolved. In order to resolve stress within the connection and not transfer bending to the downstream member, steel stiffeners and large plates are designed to take these stresses. These elements of the moment connection are subjected to large amounts of stress and can be considered a critical stress location of a structural system.

Similarly, load transferring elements such as braces and struts, must be able to transfer, at times, large loads from member to member. These load transferring elements are subjected to both axial and bending stress at times.

2.5.1.3. Columns (Axial Members)

Columns can be considered the major collecting element in a structural system. A column collects loads from the entire structure above and transfers it down to the foundation. It can be safely assumed that columns are heavily loaded structural elements. The ASIC design for compression members such as columns, considers the potential of the column to buckle under axial load. This is called the critical buckling stress of the column. Column buckling can be caused by many things, such as initial residual stress within the column due to the manufacturing process, degradation of the column or external forces brought about by structural components such as bracing or connections.

2.5.2. Methods of Mechanical Stress Mitigation

2.5.2.1. Structural Reinforcement (Retrofitting)

A simple way to relieve stress at a location of critical stress is simply to add material. Stress is basically a force distributed over an area, so by adding more material or more area stress can be relieved. A typical way to do this is to add a structural retrofit. An example of this would be increasing the capacity of a steel beam by welding an additional steel plate to the bottom flange of the beam. The amount of bending stress that the bottom flange can take increases because of the additional cross sectional area. This retrofitting or reinforcing technique is typically conducted on existing structures for which additional loading is required.

2.5.2.2. Load Path Redirection

Another way to relieve stress is by redirecting the load path. This can be done in various ways, but a good example would be a perpendicular gusset plate. Figure 2.9 below shows two built up plates, one with a gusset plate and one without. Load is applied to the back face of the vertical plate and the bending stress results at the base of the vertical plate where it connects to the base plate. This is basic result of a bending moment on a cantilevered member. By adding the perpendicular gusset plate the load path now has a different path to travel to the base plate. The load now gets distributed down the gusset and mostly becomes normal stress on the base plate. By redirecting the load path the stress intensity and type of stress is changed and the component gains a greater structural capacity.

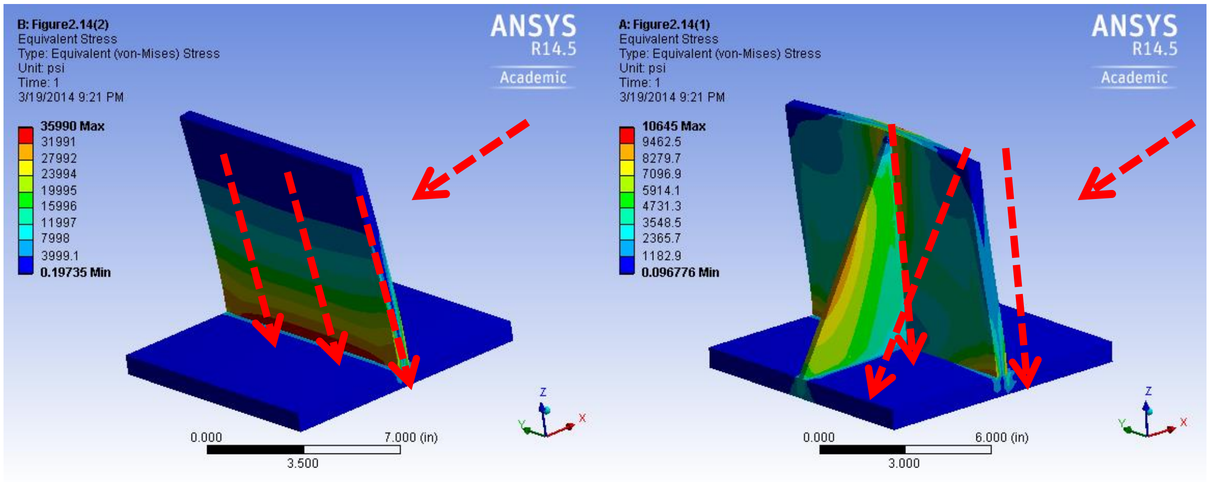

Figure 2.9: Load Path Redirection

Another good example of this is an x-brace or cross bracing member. These structural elements provide lateral support for large framed structures. Instead of resolving loads at connection points via moment connections, an x-brace provides a redirection of the load path for which the load creates axial stress along the bracing member.

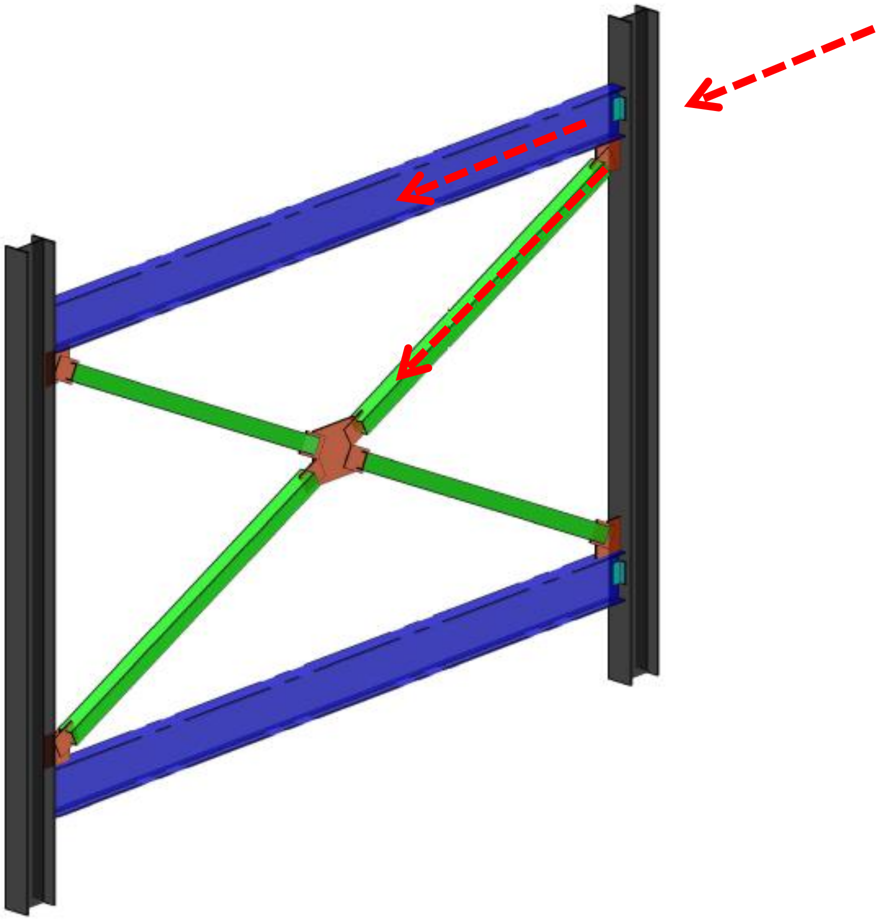

Figure 2.10: X-Brace Load Path Redirection

2.5.2.3. Counter Stress (Actuation)

Another way to relieve stress is to apply a counter stress. This is traditionally done by pre-stressing a structural component in the opposite way that an assume stress will be applied. For example, a simple beam design takes into account the critical bending stress at the midspan. By pre-stressing the beam during the manufacturing stage a positive deflection or camber can be created in the beam. When the beam is loaded the load has to overcome the initial camber before negative deflection of the beam can happen. This allows for more load to be applied before a critical bending stress is reached.

In the case of piezoelectric actuators and shape memory alloys, a surface actuator can also serve as a counter stress mechanism. The actuating material creates negative surface stress which acts as a pre-stress. When load is applied the pre-stress has to be overcome before positive stress is achieved. This grants the base material a greater capacity.

2.5.3. Stress Distribution in Composite Materials

The concept of composite modulus describes the combined material properties of the two different materials with significantly different elastic moduli. The contribution that each material has to the combined composite modulus is described in the concept of the “rule of mixtures”. The “rule of mixtures” which in the case for elastic modulus can be stated as: the contribution of each material’s elastic modulus is proportional to each material’s area fraction. The area fraction is simply the percentage of the total cross sectional area of the composite that each individual material makes up. The concept of “rule of mixtures” is traditionally utilized for fiber composites, where the contribution of fiber elastic modulus and matrix elastic modulus is found. Although this is true the concept can still be used for the mechanical relationship between the composite model presented in chapter 3, where two actuators are applied to a substrate. See figure 2.11 for the calculation of the composite modulus.

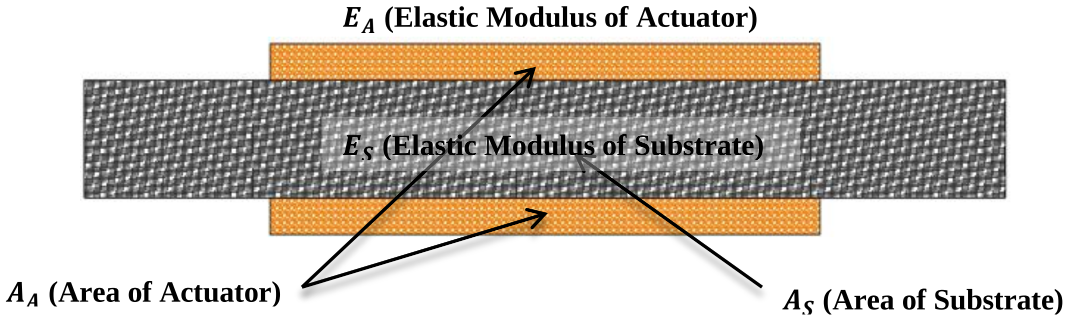

$$\bar{A}_A(area\ fraction\ of\ actuator) = \frac{A_A}{A_{Total}} \qquad \bar{A}_S(area\ fraction\ of\ substrate) = \frac{A_S}{A_{Total}}$$

$$E_C\ (Composite\ Modulus) = E_S\bar{A}_S + E_A\bar{A}_A$$

Figure 2.11: Calculation of Composite Modulus through the “Rule of Mixtures”

The purpose of understanding the methods of calculating the composite modulus of the substrate and actuator, used in chapter 3, is to develop a better understanding of the stress distribution to the substrate and actuators in respect to the stiffness of each material. For example, in chapter 3 the parametric study looks at the elastic modulus of the substrate. If the elastic modulus of the substrate is increased (becomes more stiff) and the elastic modulus of the actuator remains constant than the substrate will encounter more stress since its stiffness increased resulting in more stress being distributed to the substrate. This general concept is crucial to understanding the stress distribution with in composite materials.

CHAPTER 3. OPTIMIZATION OF PZT PATCH/SMA STRESS MITIGATION THROUGH FINITE ELEMENT MODELING

3.1. Introduction

This chapter examines the theoretical understanding of how the actuation abilities of piezoelectric actuators and shape memory alloys can aid in the stress mitigation of structural components. Through finite element modeling a parametric study is conducted. This parametric study includes many parameters including material properties, geometric consideration, and stress induction. The finite element simulations are conducted with ANSYS Mechanical.

The first two sections of this chapter demonstrate and verify the models used for the actuation simulation of piezoelectric actuators and shape memory alloys. The material properties used for the piezoelectric material models are determined through the product specifications and literatures. The material properties used for the shape memory alloy material models are determined through product specifications and experimental data. The third section discusses the parametric study and the individual parameters that are studied.

The goal of this chapter is to gain an understanding of how surface actuators interact with the substrate and what mechanisms and factors promote stress reduction. Each parameter is examined to determine the extent of its individual contribution to the stress reduction of the substrate. In order to determine a particular parameter’s effectiveness a concept of stress reduction is developed. This concept is referred to as the stress reduction percentage ($\bar{\sigma}_R$).

The substrate used in these simulations is representative of a GFRP (glass fiber reinforced polymer) board developed by SpaceAge Synthetics. The GFRP board is made up of randomly placed glass fibers suspended in polymer foam. The mechanical properties of this board are considered isotropic for the finite element model, since the random placement of fibers is impossible to model exactly. An isotropic approximation is sufficient for these simulations.

The technical guide for this product describes a modulus of elasticity range of 587.43 MPa (85.2 ksi) to 779.12 MPa (113 ksi) given for a range of densities provide for the particular product. The particular product referenced is the Versatile Thermal-Lite Board Series. This range of elastic modulus is divided into four particular values that are used for the elastic modulus parameter in the parametric study. See Table 3.1 for all the parametric values used in the study.

3.1.1. Stress Reduction Percentage

The stress reduction percentage ($\bar{\sigma}_R$) is used to express the performance of the actuator in reducing stress. The $\bar{\sigma}_R$ is simply the percentage of stress reduced by the actuator in relation to the amount of stress present in the substrate with no actuators attached. The $\sigma_{induced}$ is the amount if stress applied to the substrate through external loading without the actuator and the $\sigma_{found}$is the amount of stress recorded for the same substrate with the actuator attached. This simple comparison helps to determine the effectiveness of individual parameter variances and maintains that the level of stress induced on the substrate affects how well the actuator performs. The basic understanding of stress reduction percentage is that it is simply a comparison between the specimen without an actuator and the specimen with an actuator. The contributions to stress reduction are from many factors whether it is geometric or mechanical, but the stress reduction percentage presents the total stress reduction. The overall consideration of the stress reduction percentage ($\bar{\sigma}_R$) is that the higher the stress reduction percentage ($\bar{\sigma}_R$) the better. Later, in post study 1(section 3.4.4.), the components of stress reduction are separated and discussed.

A special consideration for a multi-parameter study of the stress induction parameter and the substrate modulus parameter is taken. Examining both the amount of stress induced on the substrate as well as the mechanical properties of the substrate itself, can present insight into how the actuator preforms and what the limits of performance are. The stress reduction percentage can be defined by the equations seen below.

$$\boldsymbol{Stress\ Reduction}\ \%\ (\bar{\boldsymbol{\sigma}}_{\boldsymbol{R}}) = \left(\frac{\boldsymbol{\sigma}_{\boldsymbol{induced}} - \boldsymbol{\sigma}_{\boldsymbol{found}}}{\boldsymbol{\sigma}_{\boldsymbol{induced}}}\right) \times \mathbf{100}$$

$$(\bar{\boldsymbol{\sigma}}_{\boldsymbol{R}}) = \left(\frac{\mathbf{8}\ \boldsymbol{MPa} - \mathbf{4}\ \boldsymbol{MPa}}{\mathbf{8}\ \boldsymbol{MPa}}\right) \times \mathbf{100} = \mathbf{50}\%$$

3.1.2. Variable Parameters and Basic Model

The parameters that are examined in the parametric study are the modulus of the substrate (E_S), modulus of the actuator (E_A), width ratio of the actuator in respect to the substrate width (r_b), length ratio of the actuator in respect to the substrate length (r_L), thickness of the substrate (t_S), actuation strain (ε_A), and stress induction (σ_i). These seven parameters are studied through using a PZT actuator and the results from these seven parameters support the multi-parameter studies discussed in Post Study 1 section 3.4.4 and Post Study 2 section 3.4.5. The implementation of a SMA actuator is included in the multi-parameter study to compare the two materials' ability as actuators. The main difference between the two actuator materials is their actuation strain. Although the actuation strain is activated by different stimuli the ending result is still a mechanical strain. The PZT actuator is driven by its strain coefficient d_{31} and the SMA actuator is driven by its thermal strain component (ε_T). For definition purposes these components are referred to as actuation drivers since they are the main components that affect the actuation abilities of the two materials. These actuation drivers make up the actuation strain parameter (ε_A). Table 3.1 shows these parameters and their variations.

Table 3.1: Parameter Values and Notation

Parameter		**Variations**	**Values**	
Substrate Modulus	$\mathbf{E_S}$	E_{S-1}	587.43 MPa	**Group 1**
		E_{S-2}	651.33 MPa	
		E_{S-3}	715.21 MPa	
		E_{S-4}	779.12 MPa	
Actuator Modulus	$\mathbf{E_A}$	E_{A-1}	52.11 GPa	
		E_{A-2}	62.11 GPa	
		E_{A-3}	72.11 GPa	
Width Ratio	$\mathbf{r_b}$	r_{b-1}	0.3	**Group 2**
		r_{b-2}	0.6	
		r_{b-3}	0.9	
Length Ratio	$\mathbf{r_L}$	r_{L-1}	0.2	
		r_{L-2}	0.4	
		r_{L-3}	0.6	
		r_{L-4}	0.8	
Substrate Thickness	$\mathbf{t_S}$	t_{S-1}	6.35mm	
		t_{S-2}	12.7mm	
		t_{S-3}	25.4mm	
		t_{S-4}	50.8mm	
Actuation Strain	$\boldsymbol{\varepsilon_A}$	$\varepsilon_{A\text{-Soft PZT}}$	0.0700%→0.1225%	**Group 3**
		$\varepsilon_{A\text{-Hard PZT}}$	0.0225%→0.0424%	
		$\varepsilon_{A\text{-SMA}}$	4%	
Induced Stress	$\boldsymbol{\sigma_i}$	σ_{i-1}	3.1496 MPa	
		σ_{i-2}	6.2992 MPa	
		σ_{i-3}	9.4488 MPa	
		σ_{i-4}	12.5984 MPa	
		σ_{i-5}	15.748 MPa	

The main purpose of the finite element simulations in this chapter is to examine the effect of actuation on the substrate. The actuation strain is the main driver of actuation and must be first clarified. The actuation strain calculated for the PZT actuator is developed through the piezoelectric strain coefficient and is a function of charge density (ρ) and electrical permittivity (ε_{11}). The actuation strain for the SMA actuator is considered based upon the thermal strain that is witnessed during experimental testing (see Chapter 4 conclusions of this thesis) and the typical range of SMA actuation strain. PZT actuators can be divided into two categories: soft PZT and hard PZT. Soft PZT has a lower elastic modulus than hard PZT but has a higher strain coefficient. This allows for longer actuation strains but with lower stress. Hard PZT, having a higher elastic modulus and lower strain coefficient, has shorter actuation strains but has higher actuation stresses supported by a stiffer material property.

The basic model is comprised of a 300mm (11.81 in) long x 50mm (1.97 in) wide x 6.35mm (0.25in) thick GFRP substrate provided by Space Age Synthetics. Upon this substrate are attached two actuators, one upon each face. The actuator has dimensions of 60mm (2.36 in) long x 30mm (1.18 in) wide x 0.5mm (0.02 in) thick. The actuator's dimensions mimic those of the DuraAct P-876 Transducer developed by Physik Instrumente. This DuraAct P-876 piezoelectric patch is discussed in more detail in the section 3.2. In order to induce stress with in the substrate one end of the substrate is subjected to a tension load. These tension loads range from 5,000 Ns to 1,000 N. With a cross sectional area of 0.0003175 m^2 (0.00635m x 0.05m) the substrate is subjected to a range of stress from 15.748 MPa to 3.1496 MPa, as indicated in table 3.1 above. This tension load is different for the substrate thickness parameter where the thickness of the substrate will require more load to achieve the same stress. By using stress as the parameter is simplifies the loading application of the basic model. See figure 3.1 for the basic presentation of the model for the parametric study in this chapter.

3.2. Piezoelectric Finite Element Model

The piezoelectric model developed for the parametric study uses the ANSYS material models for piezoelectric and piezoresistive modeling. Both these material models, as well as many others, utilize coupling elements that support the coupling effect which is characteristic of smart materials. This section discusses the general model that is used to simulate the piezoelectric actuator. There are two parts in this section: material properties and input, and model verification. The material properties found in Table 3.2 used for modeling the actuator are taken from PI (Physik Instrumente) and is based upon an actual PZT actuator that is produced by the company. The material properties that are presented by PI help to formulate the final input values for the piezoelectric model. The verification of the piezoelectric model takes into account the normal mechanical range of piezoelectric ceramics discussed in section 2. The modeling of an actuation strain with in this normal mechanical range along with the direct input of the manufacturer’s material properties is used to verify the model.

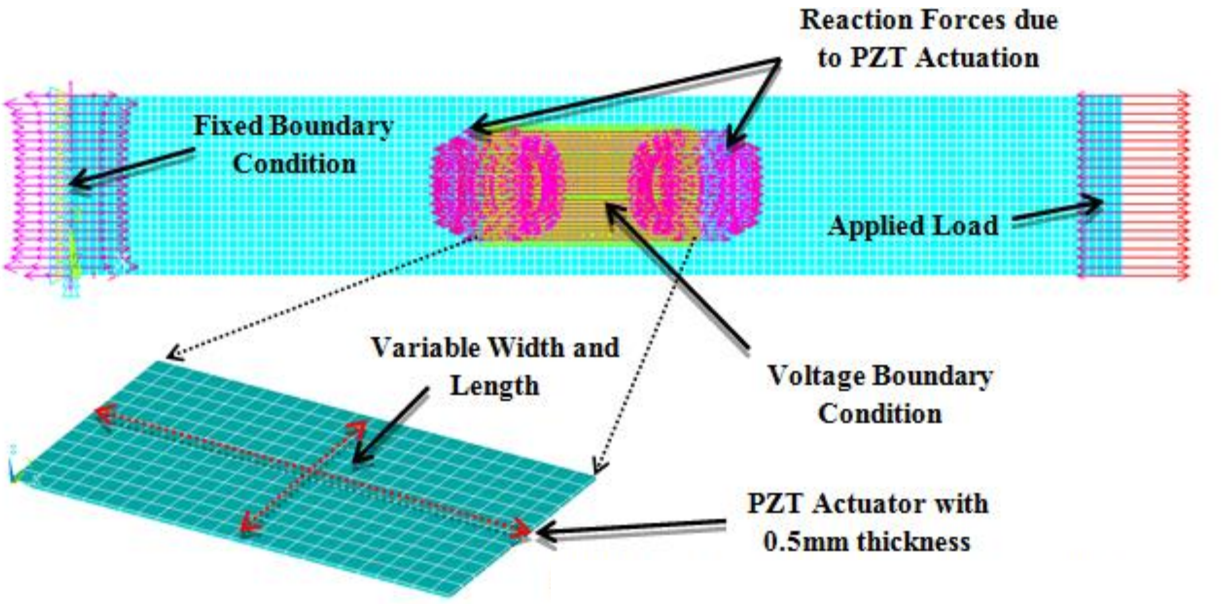

Figure 3.1: Basic Finite Element Model for Parametric Study

3.2.1. Material Properties and Input

The piezoelectric actuator model mimics an actual actuator. The actuator provided by PI (Physik Instrumente) is a DuraAct P-876 Transducer. The material properties for this actuator are provided in some detail by the manufacturer, but need to be reorganized into material properties that are directly corresponding to the ANSYS material model parameters.

Table 3.2: Material Properties based upon DuraAct P-876 Transducer

Given Material Properties	Relationship and Equations	Calculated Material Properties
Relative Permittivity $\frac{\varepsilon_{33}}{\varepsilon_o} = 1750$ $\frac{\varepsilon_{11}}{\varepsilon_o} = 1650$	$\varepsilon_o = 8.9 \times 10^{-12}\ {}^{F}/_{m}$	**Permittivity** $\varepsilon_{33} = 1.5575 \times 10^{-8}\ {}^{F}/_{m}$ $\varepsilon_{11} = 1.4685 \times 10^{-8}\ {}^{F}/_{m}$
Piezoelectric Strain Coefficient $d_{31} = -180 \times 10^{-12}\, {}^{C}/_{N}$ $d_{33} = 400 \times 10^{-12}\, {}^{C}/_{N}$ $d_{15} = 550 \times 10^{-12}\, {}^{C}/_{N}$	$C = \begin{bmatrix} C_{11} & C_{12} & C_{13} & 0 & 0 & 0 \\ C_{21} & C_{22} & C_{23} & 0 & 0 & 0 \\ C_{31} & C_{32} & C_{33} & 0 & 0 & 0 \\ 0 & 0 & 0 & C_{44} & 0 & 0 \\ 0 & 0 & 0 & 0 & C_{55} & 0 \\ 0 & 0 & 0 & 0 & 0 & C_{66} \end{bmatrix} \Rightarrow C^{-1} = S = \begin{bmatrix} \frac{1}{E_1} & \frac{-v_{21}}{E_2} & \frac{-v_{31}}{E_3} & 0 & 0 & 0 \\ \frac{-v_{12}}{E_1} & \frac{1}{E_2} & \frac{-v_{32}}{E_3} & 0 & 0 & 0 \\ \frac{-v_{13}}{E_1} & \frac{-v_{23}}{E_2} & \frac{1}{E_3} & 0 & 0 & 0 \\ 0 & 0 & 0 & \frac{1}{G_{23}} & 0 & 0 \\ 0 & 0 & 0 & 0 & \frac{1}{G_{31}} & 0 \\ 0 & 0 & 0 & 0 & 0 & \frac{1}{G_{12}} \end{bmatrix}$	**Piezoelectric Stress Coefficient** $e_{13} = -6.6816\ {}^{C}/_{m^2}$ $e_{33} = 14.4565\, {}^{C}/_{m^2}$ $e_{42} = 11.6327\, {}^{C}/_{m^2}$
Elastic Compliance Coefficient $S_{11} = 16.1 \times 10^{-12}\ {}^{m^2}/_{N}$ $S_{33} = 20.7 \times 10^{-12}\ {}^{m^2}/_{N}$	$C_{33} = 100$ GPa is criteria for the final stiffness matrix; Iteration is used to determine a final Poisson's ratio ($v_{31,32}$ and $v_{13,23}$)	**Elastic Stiffness Coefficient** $C_{11} = 120.6 \times 10^9\ {}^{N}/_{m^2}$ $C_{12} = 74.22 \times 10^9\ {}^{N}/_{m^2}$ $C_{13} = 70.95 \times 10^9\ {}^{N}/_{m^2}$ $C_{44} = 21.15 \times 10^9\ {}^{N}/_{m^2}$ $C_{66} = 23.18 \times 10^9\ {}^{N}/_{m^2}$
Elastic Stiffness Coefficient $C_{33} = 100 \times 10^9\ {}^{N}/_{m^2}$	$e = cd^T = \begin{bmatrix} 0 & 0 & e_{13} \\ 0 & 0 & e_{13} \\ 0 & 0 & e_{33} \\ 0 & e_{42} & 0 \\ e_{42} & 0 & 0 \\ 0 & 0 & 0 \end{bmatrix} \qquad d^T = ec^{-1} = \begin{bmatrix} 0 & 0 & d_{31} \\ 0 & 0 & d_{31} \\ 0 & 0 & d_{33} \\ 0 & d_{15} & 0 \\ d_{15} & 0 & 0 \\ 0 & 0 & 0 \end{bmatrix}$	
Poisson's Ratio $v_{12,21} = 0.34$		**Poisson's Ratio** $v_{31,32} = 0.3642$ $v_{13,23} = 0.4683$
Elastic Modulus $E_1 = \frac{1}{S_{11}} = 62.11 \times 10^9\, {}^{N}/_{m^2}$ $E_2 = \frac{1}{S_{11}} = 62.11 \times 10^9\, {}^{N}/_{m^2}$ $E_3 = \frac{1}{S_{33}} = 48.31 \times 10^9\, {}^{N}/_{m^2}$	$G_{23} = \frac{E_2}{2(1 + v_{23})}$ $G_{13} = \frac{E_3}{2(1 + v_{31})}$ $G_{12} = \frac{E_1}{2(1 + v_{12})}$	**Shear Modulus** $G_{23} = C_{44} = 21.15 \times 10^9\ {}^{N}/_{m^2}$ $G_{13} = C_{44} = 21.15 \times 10^9\ {}^{N}/_{m^2}$ $G_{12} = C_{66} = 23.18 \times 10^9\ {}^{N}/_{m^2}$

Table 3.2 shows the material properties supplied by the manufacturer and the general relationships of material mechanics and piezoelectric formulation that help to transform them into material properties that are used as the direct input values for the ANSYS model. There are three main input matrices for the piezoelectric material model. These are the permittivity matrix, the piezoelectric matrix, and the stiffness matrix. The stiffness matrix is selected as a linear elastic and anisotropic material. The piezoelectric matrix can be inputted in two ways. The piezoelectric stress coefficients (e) can be inputted when stress is declared as the analysis method. The alternative is inputting the strain coefficients (d) when the user declares the analysis method as a strain analysis. This distinction between input methods signifies that both methods produce the same results but are formulated from the coupling characteristic of piezoelectric material. The input values used for the piezoelectric model for the DuraAct P-876 are seen in Table 3.3.

Table 3.3: Input Values for ANSYS Piezoelectric Modeling of DuraAct P-876

Material Properties	ANSYS Input Variables	Final Input Matrices
$\varepsilon_{11} = 1.4685 \times 10^{-8}\ F/m$ $\varepsilon_{33} = 1.5575 \times 10^{-8}\ F/m$	$EP = \begin{bmatrix} EP_{11} & EP_{12} & EP_{13} \\ EP_{21} & EP_{22} & EP_{23} \\ EP_{31} & EP_{32} & EP_{33} \end{bmatrix}$	$EP = \begin{bmatrix} 1.4685 & 0 & 0 \\ 0 & 1.4685 & 0 \\ 0 & 0 & 1.5575 \end{bmatrix}$
$d_{31} = -180 \times 10^{-12}\ C/N$ $d_{33} = 400 \times 10^{-12}\ C/N$ $d_{15} = 550 \times 10^{-12}\ C/N$	$d_{ij} = \begin{bmatrix} d_{xx} & d_{xy} & d_{xz} \\ d_{yx} & d_{yy} & d_{yz} \\ d_{zx} & d_{zy} & d_{zz} \\ d_{xy-x} & d_{xy-y} & d_{xy-z} \\ d_{yz-x} & d_{yz-y} & d_{yz-z} \\ d_{xz-x} & d_{xz-y} & d_{xz-z} \end{bmatrix}$	$d_{ij} = \begin{bmatrix} 0 & 0 & -180 \\ 0 & 0 & -180 \\ 0 & 0 & 400 \\ 0 & 550 & 0 \\ 550 & 0 & 0 \\ 0 & 0 & 0 \end{bmatrix}$
$C_{11} = 120.6 \times 10^{9}\ N/m^2$ $C_{12} = 74.22 \times 10^{9}\ N/m^2$ $C_{13} = 70.95 \times 10^{9}\ N/m^2$ $C_{33} = 100 \times 10^{9}\ N/m^2$ $C_{44} = 21.15 \times 10^{9}\ N/m^2$ $C_{66} = 23.18 \times 10^{9}\ N/m^2$	$D = \begin{bmatrix} D_{11} & D_{12} & D_{13} & D_{14} & D_{15} & D_{16} \\ & D_{22} & D_{23} & D_{24} & D_{25} & D_{26} \\ & & D_{33} & D_{34} & D_{35} & D_{36} \\ & sym & & D_{44} & D_{45} & D_{46} \\ & & & & D_{55} & D_{56} \\ & & & & & D_{66} \end{bmatrix}$	$D = \begin{bmatrix} 120.6 & 74.22 & 70.95 & 0 & 0 & 0 \\ & 120.6 & 70.95 & 0 & 0 & 0 \\ & & 100 & 0 & 0 & 0 \\ & & & 21.15 & 0 & 0 \\ & sym & & & 21.15 & 0 \\ & & & & & 23.18 \end{bmatrix}$

The ANSYS matrix EP represents the electrical permittivity of the material. In the case of PZT, the permittivity is described as orthotropic. The permittivity along the number 1 and number 2 axes are the same and the permittivity along the number 3 axis is different. The ANSYS matrix D represents the anisotropic input for the mechanical material properties of the PZT actuator. The matrix is inputted as a symmetric matrix and supports any anisotropic material input. PZT, being orthotropic, follows the same symmetry between axis number 1 and 2. The ANSYS matrix d represents the piezoelectric effect, either being supported by piezoelectric strain coefficients or piezoelectric stress coefficients.

With the input values for the piezoelectric material model declared, they are ready to support the inverse piezoelectric effect. The introduction of a voltage potential on the actuator is applied as two boundary surfaces which are equal and opposite. The two boundaries are applied on the surfaces of the actuator that are perpendicular to the axis of polarization. In this case these surfaces are the top and bottom surfaces of the actuator. The piezoelectric strain matrix's components are not all affected by voltage potential along the polarized axis. With this in mind, the only components affected are the $d_{31}$and d_{33}components. The d_{15} component is only affected by a voltage potential applied on the number 1 and number 2 surfaces which promotes shearing of the PZT actuator. Since the applied voltage is only in respect to the polarized axis the only mechanical occurrences are displacements along the normal faces of the shape model.

Along with the orientation of the polarized axis, the positive and negative directions of the polarized axis must be considered. The application of alternate voltage potentials on opposite faces of the material either supports a contraction or expansion of the actuator. This is controlled by applying the right positive and negative potentials on the right surfaces. For this model, to induce a contraction of the PZT, the negative voltage potential is applied on the top surface respectively and the positive voltage potential is applied on the bottom surface respectively. To insure that the right surfaces of the actuator are supplied with the right voltage the direct piezoelectric effect can be used as a reference. The direct piezoelectric effect can show upon the application of a mechanical influence which surfaces produce negative or positive voltage potentials.

A simple simulation applying both piezoelectric effects was done to insure that the direct effect and inverse effect are proportional to each other. A tension force is applied to the PZT actuator and the surface charge created on the top surface is recorded. This surface charge is gathered at every node that makes up the top surface of the modeled actuator. These nodes represent the surface charge across the area of the top surface. This surface charge has a unit of coulomb (C) which is Faraday (F) multiplied by voltage (V). The farad unit is the capacitance unit which describes the capacitance of a material. The electrical characteristics of PZT make it a capacitor which can store electric charge as voltage potential. This relationship can be used to calculate the amount of voltage on the top surface of the actuator considering the amount of surface charge recorded [$voltage\ (V) = surface\ charge(C) \div farad\ (F)$].

Figure 3.2 shows the voltage gain for a certain amount of stress induced upon the actuator. The voltage that is generated on the surface has a positive charge and is due to stress caused by tension. In order to counter this, the inverse piezoelectric effect can be used by applying opposite voltage to that surface. The results show that the direct and inverse effects are proportional to each other. The influence of one is canceled out by the influence of the other. The direct effect produces a voltage gain on the top surface of +765 volts. Applying -1000 volts to the same surface cancels out this positive voltage and actually is enough to produce a contraction of the actuator with a final voltage of -235 volts. This verifies that the direct and inverse piezoelectric effects show coupling characteristics within the finite element model.

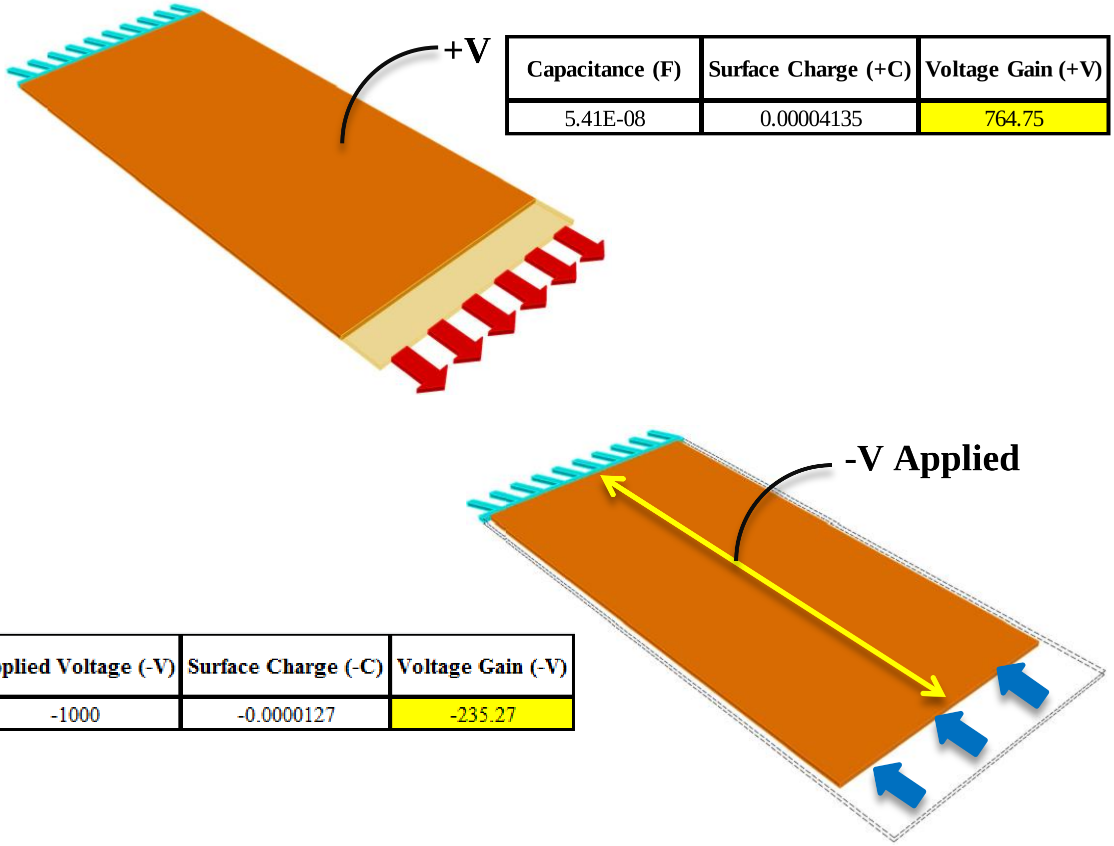

Capacitance (F)	Surface Charge (+C)	Voltage Gain (+V)
5.41E-08	0.00004135	764.75

Applied Voltage (-V)	Surface Charge (-C)	Voltage Gain (-V)
-1000	-0.0000127	-235.27

Figure 3.2: Schematic of Direct and Inverse Piezoelectric Effect

3.2.2. Model Verification

The verification of the finite element model can be accomplished in two ways. The first way is to verify that the input method and values are in accordance with general piezoelectric formulation. The second way is to verify that the results of the simulated piezoelectric effect are within the normal mechanical range (actuation strain) that is typical for piezoelectric ceramics.

Verifying the model in accordance with general piezoelectric formulation, is done by assuring that the input is complete and that the three matrices needed are indeed permittivity (ε), piezoelectric coefficients (d), and stiffness (c). Figure 3.3 presents the entire finite element formulation for piezoelectric simulation. Research of piezoelectric finite element formulation was conducted and the below formulation is mainly reference from “A Smooth Four-Node Piezoeletric Element for Analysis of Two-Dimensional Smart Structures” by Nguyen, Mai-Duy and Tran-Cong.

$K_{uu} = Mechanical\ Stiffness$

$K_{u\phi}, K_{\phi u} = Piezoelectric\ Coupling$

$K_{\phi\phi} = Capacitance$

Mechanical and Electrical Loads

$$\underbrace{\begin{bmatrix} K_{uu} = \int_V [B_u]^T \underline{[c]} [B_u] dV & K_{u\phi} = \int_V [B_u]^T \underline{[e]} [B_\phi] dV \\ K_{\phi u} = \int_V [B_\phi]^T \underline{[e]}^T [B_u] dV & K_{\phi\phi} = \int_V [B_\phi]^T \underline{[\epsilon]} [B_\phi] dV \end{bmatrix}}_{\textbf{Stiffness Matrix}} \begin{Bmatrix} u_i \\ v_i \\ w_i \\ \phi_i \end{Bmatrix} = \begin{Bmatrix} F \\ Q \end{Bmatrix}$$

Degrees of Freedom
(3 dimensional translation and voltage)

Figure 3.3: Basic Piezoelectric Formulation

Typical actuation strain range for piezoelectric ceramics is 0.07 % to 0.15%. In this chapter several piezoelectric ceramic actuators are simulated through finite element analysis and the actuation strains recorded are within this range. See figure 3.7 for the various PZT products tested through finite element analysis and the corresponding recorded actuation strain.

3.3. Shape Memory Alloy Finite Element Model

The finite element models used for simulating shape memory alloy as a structural retrofit can be separated into three models. The first model simulates the pseudoelastic (superelastic) characteristics of the material at temperatures above austenite finish temperature (A_f), which were discussed in Chapter 2. The second model simulates the shape memory effect of the material. The third model simulates the detwinning of shape memory alloy from twinned martensite to detwinned martensite at temperatures below the austenite start temperature (A_s), for which is typically around room temperature. The shape memory effect simulation is what is used in the actuation simulations for the single actuation strain parameter in this chapter and the beam retrofit models discussed in Chapter 5 sections 5.1 and 5.2. The pseudoelastic model simulation is used in chapter 5 for a column retrofit model. The detwinning model was used for general formulation of models and for column buckling simulations found in Chapter 5. This section is simply a brief explanation of the finite element models used for all the shape memory alloy models in this thesis. All models and results refer to this section for clarity of development and model setup.

3.3.1. Pseudoelastic (Superelastic) Model

The pseudoelastic finite element model follows a direct stress-strain relationship input. Six input values are needed for the SMA finite element model used by ANSYS. The first is the elastic modulus ($E_{Aust.}$) value of austenitic nitinol since the pseudoelastic characteristic of shape memory alloys occurs at temperatures above the austenite finish temperature. The next four input values are stress/strain values ($\sigma_{Ms}, \sigma_{Mf}, \sigma_{As}, \sigma_{Af}$) which distinguishes the particular detwinning start and detwinning finish stresses for both the forward and backward portions of the hysteresis curve. As discussed in Chapter 2 the pseudoelastic characteristic follows a hysteresis curve which has different forward and backward curves but has the same start and ending value. Also, remember that the detwinning discussed here is the direct detwinning of austenite to detwinned martensite, which can occur at high stress levels. The sixth value is the strain length (ε_L) which is the amount of total plastic strain that occurs along the detwinning path of the curve. This value distinguishes the amount of strain that occurs during both the forward detwinning and the backwards strain recovery of the pseudoelastic effect of shape memory alloy.

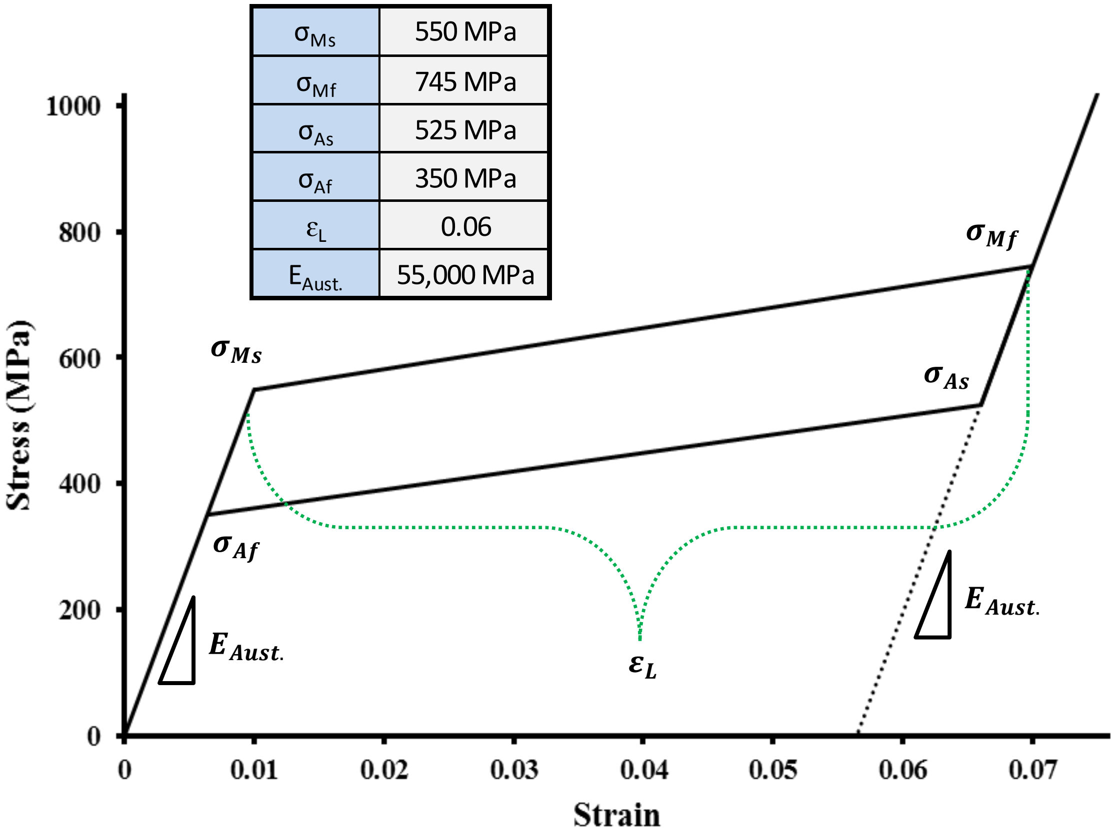

σ_{Ms}	550 MPa
σ_{Mf}	745 MPa
σ_{As}	525 MPa
σ_{Af}	350 MPa
ε_L	0.06
$E_{Aust.}$	55,000 MPa

Figure 3.4: Pseudoelastic Finite Element Input Values

3.3.2. Shape Memory Effect Model

The simulation of the shape memory effect can be approximated by the implementation of a finite element thermal strain model. The total strain that is desired is accomplished by implementing a thermal expansion coefficient of $\varepsilon_{Thermal} = -0.0011111/$°F. The model then is subjected to a temperature increase from room temperature to a temperature value that gives the desired thermal strain. For example, a strain of 0.04 requires a temperature change of 36 °F to simulate the actuation strain of 0.04 through the thermal strain model. See chapter 4 conclusions for considerations for the use of 4% actuation strain in SMA actuation simulations.

The elastic modulus for the shape memory alloy used for this model is that of completely detwinned martensite. As discussed in Chapter 2, in order to get the maximum strain out of the SMA, the material must be in the detwinned martensite state. This makes sense since the strains that are accrued during detwinning are the strains that, through recovery, make up the concept of the shape memory effect. The elastic modulus of detwinned martensite, acquired through physical testing presented in chapter 4, is $E_{Detw.Mart.} = 2{,}030{,}500\ psi$. The elastic modulus is generated from the results shown in figure 4.6, which shows the slope of the strain-stress curve of the material after detwinning is accomplished.

It can be assumed that as the shape memory effect occurs through forward transformation that an increase in elastic modulus occurs when the material changes from martensite to austenite. This occurrence can be difficult to simulate so a conservative approach is taken where the elastic modulus is assumed to be that of detwinned martensite for the entire actuation simulation. Another important assumption is that the simulated actuation strain of the shape memory alloy is a linear strain, which is not completely representative of the SMA strain during the shape memory effect. The shape memory effect (shown in Figure 2.3) during the forward and backward transformation shows a rather non-linear strain. For the simplicity of the model the finite element simulations are conducted assuming the SMA strain is linear.

3.3.3. Detwinning Model

The detwinning model simulates the deformation of twinned martensite to detwinned martensite. This characteristic can be simulated though a multi-linear finite element material model, for which a stress/strain relationship curve is declared for an apparently plastic and therefore non-linear material curve. The multi-linear approach declares several linear lines that make up an approximation of a non-linear material. This type of material model is perfect for simulating the non-linear behavior of shape memory alloys during the detwinning phase. The values that are needed for this multi-linear model are directly attained through physical testing, which is presented in chapter 4, of the material. This multi-liner curve is shown in Figure 3.5.

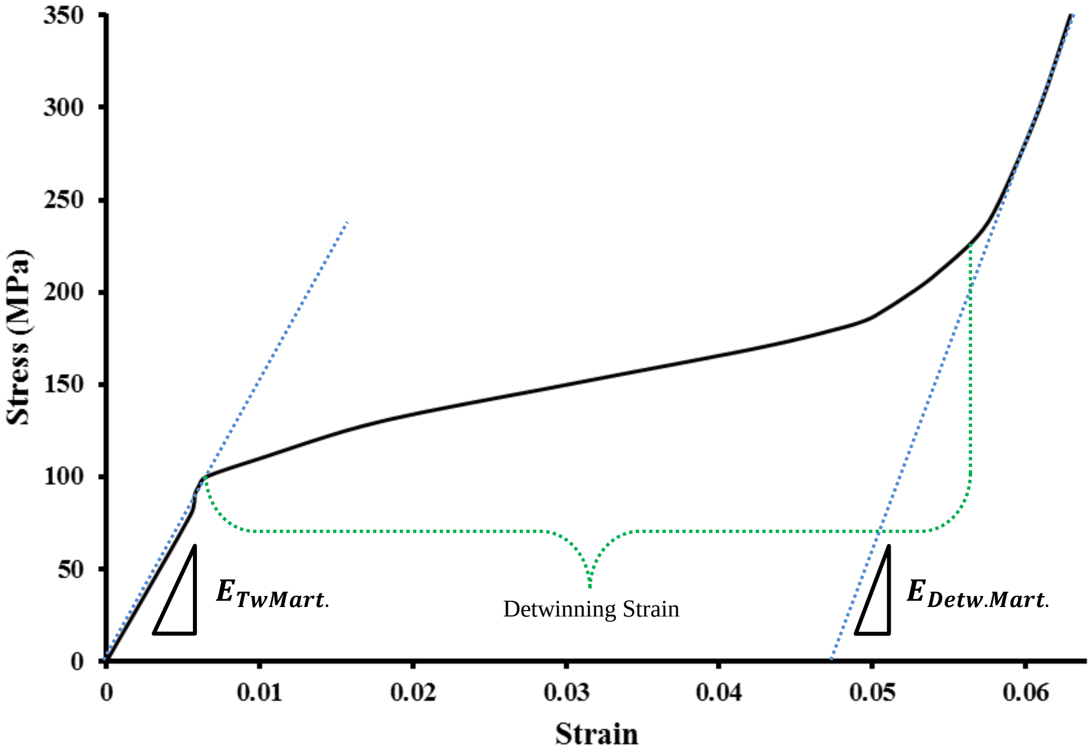

Figure 3.5: Multi-linear Curve of Martensitic SMA

3.4. Parametric Study

This study examines the effect of several parametric changes made in the general actuation model. These parameters, which are discussed in the chapter introduction, are comprised of several geometric and material based characteristics. Each parameter is explored and discussed. Table 3.1 is divided into three parameter groups and these groups are analyzed together. The first group is comprised of the elastic modulus of the substrate and the actuator (E_S & E_A). This groups looks at the effect of the stiffness of the actuator on its stress reduction capabilities. The range of substrate modulus is selected from typical material property values declared by the manufacturer discussed at the beginning of this chapter. The range of elastic modulus for the actuator is selected from typical material properties similar to the DuraAct P-876 Transducer Patch discussed earlier (see section 3.2.1).

The second group is comprised of three geometric variances in the model. These variances consist of the width of the actuator compared to the width of the substrate (r_b), the length of the actuator compared to the length of the substrate (r_L), and the thickness of the substrate (t_S). The ranges for these three geometric parameters are selected through the reasoning that the change in actuator size could have a great effect on the actuation stress distributed to the substrate. Also the thickness of the substrate was chosen as a parameter because the length and width of the substrate would have to be maintained since the parameters involving the actuator size were based upon the ratio resulting from the comparison with the substrate dimensions.

The third group is comprised of actuation strain of the actuator (ε_A) and the stress induced (σ_i) at the location of the actuator. These two parameters have a reciprocal relationship for which they are contrasted. The ability of the actuation strain to reduce stress in the substrate is directly affected by the amount of stress induced on the substrate. The ranges for these two parameters are selected from typical strains indicated for PZT and SMA material per either manufacturer documentation and/or experiment results. SMA actuation strains are referenced from material testings conducted which are discussed in the conclusions of chapter 4. PZT actuation strains are referenced from Physik Instrumentes DuraAct P-876 Transducer (see section 3.2.1.).

Group 1 and 2 are consistent between the two materials (SMA and PZT) used for the actuators. One material (PZT) is used to simulate these first two groups since the impact that these parameters have on stress reduction are independent of the type of material being used for the actuator. This conclusion is supported by the fact that the actuation of SMA and PZT are similar in the sense that they both produce actuation strain. The difference between the two is the way in which this actuation strain is achieved. The third group is examined by utilizing both SMA and PZT models. By looking at both SMA and PZT actuation strains the difference between the two materials can be considered when compared to the amount of stress induced on the substrate.

After these three groups are explored a post study is done. The first post study considers an equivalent patch upon which the amount of stress reduction caused by the actuator is separated from the amount of stress reduction caused by the composite modulus of the substrate and actuator. The second post study looks closer at the interaction between induced stress and actuation strain and how they interact with the addition of a third parameter, substrate modulus.

The average stress is recorded by summing the total elemental stress at the mid-point of the actuator and dividing by the number of elements. The substrate elements at this location represent the elements that are experiencing the most stress reduction. All parameters are analyzed by this recording method so that consistency of data collection is achieved. Figure 3.6 shows this process of recording data. The right-hand picture in figure 3.6 shows the typical distribution that is found when the elements at this location are extracted. The distribution of stress or strain or whatever is recorded, is not distributed evenly. In order to gain consistency in the recording process and maintain simplicity in the study, the average stress is taken instead of the distribution.

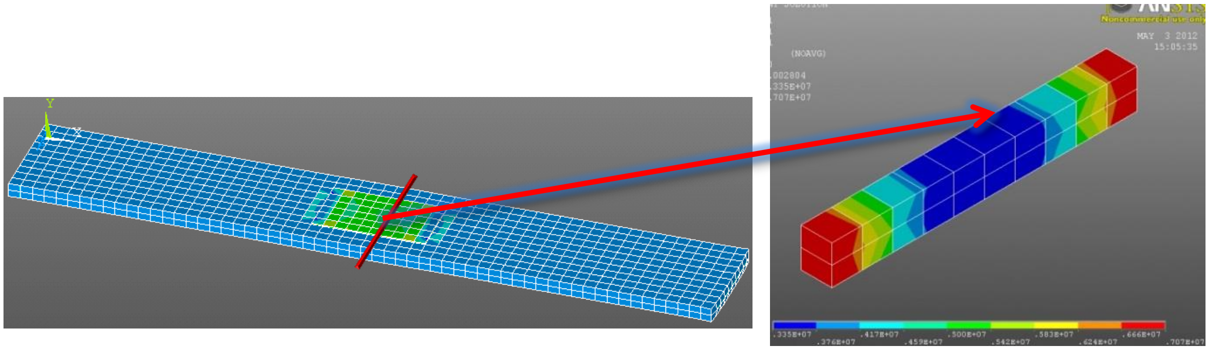

Figure 3.6: Recording Process

The results for each group of parameters are presented by two simulations. The first simulation involves a non-stressed substrate. This simulation maintains that the substrate is experiencing no stress during the actuation of the actuator. The results for this simulation are comprised solely of the stresses and strains that are induced on the substrate solely by the actuator. The second simulation involves a stressed substrate. This simulation maintains that the substrate is experiencing axial stress during the actuation of the actuator. The results for this simulation are comprised of the resulting stresses and strains that are found in the substrate. The non-stressed state values are negative values associated with compression of the actuator and the stressed state values are positive values associated with tension of the substrate.

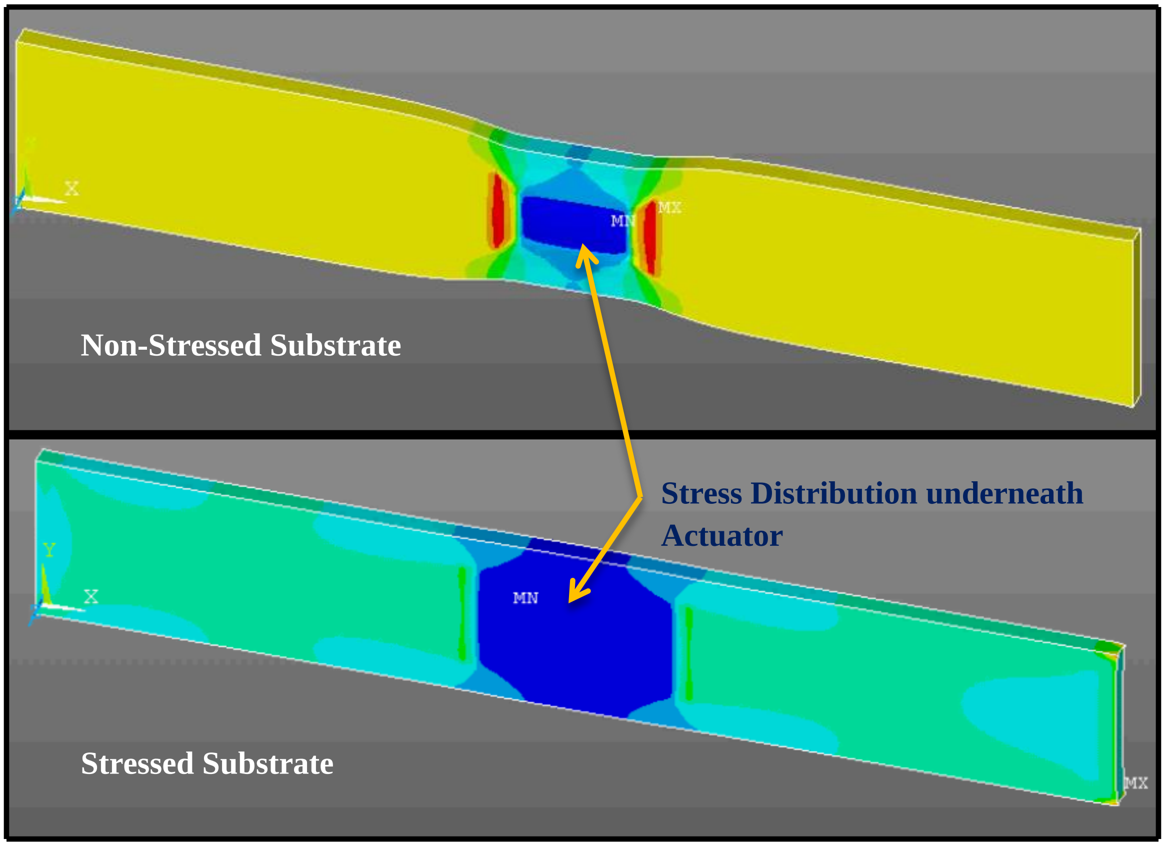

Figure 3.7: Non-Stressed and Stressed Substrate States

3.4.1. Group 1 – Material Stiffness

The stiffness of either the substrate or the actuator can affect the ability of the actuator to reduce stress. A stiffer substrate is more resistant to external forces just as a stiffer actuator is able to affect the substrate more than a softer or less stiff actuator. The study of group 1 examines the significance of the elastic modulus parameter in being a component of stress reduction.

The elastic modulus of either the substrate or the actuator is an important component that can be used to understand the interaction between the actuator and the substrate. Increasing the stiffness of one or the other influences the other directly and influences the amount of stress reduction. In the study of group 1, all other parameters are kept constant so this influence of material stiffness can be witnessed. Table 3.4 shows the results of this study presented in average strains and average stresses. Also presented in Table 3.4 is the stress reduction percentage according to a 15.748 MPa stress induced in the substrate (for stressed substrate only), which is parameter (σ_i) (see chapter 3 introduction section 3.1). The orange highlighted value indicates the parameter value which is kept constant as the other parameters are changed (i.e. all results presented for E_A are associated with E_S equal to 587.43 MPa).

Table 3.4: Group 1 – Material Stiffness Parameters

GROUP 1		**Non-Stressed Substrate**		**Stressed Substrate**		
		ε_{avg}	σ_{avg} **(MPa)**	ε_{avg}	σ_{avg} **(MPa)**	$\overline{\sigma}_R$ **(%)**
E_S	**587.43 MPa**	-0.0614	-0.43	0.273	1.568	90.01
	651.33 MPa	-0.0607	-0.472	0.2604	1.656	89.45
	715.21 MPa	-0.06	-0.514	0.25	1.741	88.91
	779.12 MPa	-0.0595	-0.554	0.241	1.825	88.38
E_A	**52.11 GPa**	-0.0602	-0.423	0.313	1.806	88.5
	62.11 Gpa	-0.0614	-0.43	0.273	1.568	90.01
	72.11 GPa	-0.0622	-0.435	0.243	1.392	91.13
Constant Parameters		r_b	r_L	t_S	ε_A	σ_i
		0.6	0.2	6.35mm	700με	15.748 MPa

3.4.1.1. Commentary – Elastic Modulus of Substrate (E_S)

As the stiffness of the substrate increases the stress found in the substrate during the non-stressed state increases. Since the actuation strain of the actuator remains constant the amount of stress that the actuator can put on the substrate is dependent on the stiffness of the substrate. Even though the substrate is increasing in stiffness, the strain found in the substrate does not change much. This, close to constant strain, is transformed into increasing stress per the increasing elastic modulus of the substrate. The simple consideration is that the stiffer the material becomes the more it is resistant to the actuation force from the actuator. When the substrate becomes stressed through external axial forces the same stiffness consideration can be witnessed. As the stiffness of the substrate increases the actuator becomes less able to reduce stress in the substrate. This is also due to the change in the composite modulus of the substrate/actuator composite. The increasing stiffness of the substrate distributes more stress to the substrate. Although the actuator is greater in stiffness than the substrate the increase in substrate stiffness allows for more stress to be distributed to it.

3.4.1.2. Commentary – Elastic Modulus of Actuator (E_A)

The increasing stiffness of the actuator allows for stronger actuation forces. The actuation strain along with a stiffer actuator material can better apply force on the substrate as well as resist external forces as in the stress state of the substrate. This is seen as an increase in stress reduction. The non-stressed state results show that the stress induced on the substrate does not increase much with the increasing stiffness of the actuator. The stressed state results show a large increase in stress reduction and overall effect on the substrate. This is mainly due to the composite modulus of the substrate/actuator composite. There is a close relationship that piezoelectric actuators have between the actuation strain of the material and the overall stiffness of the material. This relationship is the reason for such small change in stress induced on the substrate through actuation. This relationship is explored more through the study of parameter group 3.

3.4.2. Group 2 – Geometric Consideration

The geometry of the actuator patch attached to a substrate is a basic model. There are a few geometric considerations that can be looked at that effect the potential for the actuator to reduce stress with in the substrate that it is attached to. There are three geometric variances examined in this parameter group. The first is the width of the actuator compared to the width of the substrate (r_b). This parameter is represented by a ratio between the two. The second is the length of the actuator compared to the length of the substrate (r_L). This parameter is also represented by a ratio between the two. The third examines the effect of the thickness (t_s) of the substrate and the ability of the actuator to reduce stress through its thickness.

Table 3.5: Group 2 – Geometric Consideration Parameters

GROUP 2		**Non-Stressed Substrate**		**Stressed Substrate**		
		ε_{avg} (%)	**σ_{avg} (MPa)**	**ε_{avg} (%)**	**σ_{avg} (MPa)**	**$\overline{\sigma}_R$ (%)**
r_b	**0.3**	-0.0467	-0.3010	0.7450	4.5000	71.338
	0.6	-0.0614	-0.4300	0.2730	1.5680	90.013
	0.9	-0.0659	-0.4980	0.1004	0.4720	96.994
r_L	**0.2**	-0.0614	-0.4300	0.2730	1.5680	90.013
	0.4	-0.0606	-0.4270	0.1846	0.9990	93.637
	0.6	-0.0571	-0.4060	0.1799	0.9690	93.828
	0.8	-0.0488	-0.3580	0.1797	0.9670	93.841
t_S	**6.35mm**	-0.0614	-0.4300	0.2730	1.5680	90.127
	12.7mm	-0.0543	-0.3750	0.5265	3.0857	80.346
	25.4mm	-0.0398	-0.2720	1.0298	5.9429	62.147
	50.8mm	-0.0210	-0.1500	1.7400	9.8506	37.257
Constant Parameters			**E_S**	**E_A**	**ε_A**	**σ_i**
			587.43 MPa	62.11 GPa	700με	15.748 MPa

3.4.2.1. Commentary – Width Ratio (r_b)

The width ratio of the actuator to the substrate can be used to understand the effectiveness of the actuator to reduce stress when it is placed and positioned wisely along the target area. The results show that as the width ratio increases the stress reduction increases. Please note that stress is recorded along the whole width of the substrate. It makes sense then that the largest width ratio is able to reduce more stress. It not only covers more surface area of the substrate, but also increases the composite modulus of the actuator/substrate composite which directs more of the induced stress upon itself (actuator) and away from the substrate, since it is a stiffer material.

3.4.2.2. Commentary – Length Ratio (r_L)

The length ratio of the actuator compared to the length of the substrate can be used to help understand the effectiveness of the length of the actuator in reducing stress with in the substrate. The results show that as the length of the actuator increase so does the stress reduction. The initial increase in stress reduction is considerable but after 0.4 the stress reduction begins to plateau. Please note that the stress is recorded at the mid cross section of the substrate. With this in consideration it makes sense that the initial increase from 0.2 to 0.4 length ratio supports an increase in stress reduction because it is still close to the target area of the record stress. As the length further increases the actuators influence on the target area decreases and the increasing stress reduction seen here begins to diminish.

3.4.2.3. Commentary – Substrate Thickness (t_S)

The thickness of the substrate is an important factor in understanding the limits and applicability of the actuator. The effectiveness of the actuator in reducing stress in the substrate is greatly affected by the thickness of the substrate. The results show that the stress reduction decreases dramatically as the substrate becomes thicker. This makes sense since the effect of surface actuation is overcome by the general increase in substrate material or mass. Also the induced stress parameter is maintained at 15.748 MPa which as the substrate thickness increases so the does the tension load required to achieve the same stress over more area.

3.4.3. Group 3 – Stress Interaction

The main component that influences stress reduction is stress itself. Stress both acting on the substrate externally and stress acting on the substrate by the influence of actuation stress. It would make sense to assume that the level of stress reduction is very much dependent on the amount of stress introduced into the system and the amount of countering stress produced within the system by the actuator. This parameter group examines the effect that the amount of induced stress has on the level of stress reduction as well as the effect of the amount of stress produced by the actuator. Separated into the two parameters, actuation strain (ε_A) and induced stress (σ_i), this group gives the most important insight into understanding the effectiveness of the actuation simulations.

This study looks at both actuation strain (ε_A) and induced stress (σ_i) in a multi parameter study since these two components are dependent on each other in respect to the level of stress reduction. First this multi parameter study examines the actuator as PZT material and secondly the multi parameter study examines the actuator as a SMA material. This separation shows the difference between the two materials.

3.4.3.1. Commentary – Induced Stress

The values for induced stress (σ_i) are calculated from an external tensile load applied to the end of the substrate which is distributed over the substrate's cross-sectional area (see chapter 3 introduction section 3.1). The results in Table 3.6 show that as the amount of stress induced in the system increases the amount of stress reduction decreases. These results follow the reasoning that at some point of increasing stress there will be negligible levels of stress reduction caused by the actuator. This is simply due to the fact that there will a point where very large stresses cannot be effectively countered by the actuator material (PZT) and it’s actuation ability. Basically there is a limit to the stress reduction capabilities of the actuator. PZT and SMA both produce different levels of actuation strain while for the most part having common mechanical material properties. The SMA actuator can produce larger actuation strains than the PZT actuator; hence it can overcome larger stresses making it effective at higher stresses. The results shown for the SMA actuator are from simulations at higher stress levels making it more suitable for applications involving higher stresses. This is consistent with the common characteristic of shape memory materials, which is they can support large mechanical strain while under large amounts of stress. This characteristic is very beneficial for this actuation application.

Table 3.6: Group 3 – Stress Interaction

GROUP 3 - PZT $(\bar{\sigma}_R)$ (%)		**Induced Stress (MPa)**				
		3.15	**6.30**	**9.45**	**12.60**	**15.75**
Pz 24	$\varepsilon_A=225\mu\varepsilon$	94.57	92.27	91.51	91.13	90.90
Vibrit 202	$\varepsilon_A=350\mu\varepsilon$	96.60	93.02	91.83	91.24	90.88
DuraAct P-876	$\varepsilon_A=700\mu\varepsilon$	101.21	94.23	91.90	90.74	90.04
Pz 29	$\varepsilon_A=945\mu\varepsilon$	105.57	96.19	93.06	91.50	90.56
Vibrit 1100	$\varepsilon_A=1225\mu\varepsilon$	112.53	100.27	96.19	94.14	92.92

SMA $(\bar{\sigma}_R)$ (%)	**Induced Stress (MPa)**					
	37.80	**50.39**	**62.99**	**75.59**	**88.19**	**125.98**
$\varepsilon_A=40{,}000\mu\varepsilon$	101.24	98.12	96.25	95.01	94.12	92.51

3.4.3.2. Commentary – Actuation Strain

The actuation strains of PZT and SMA material are very different. As discussed in Chapter 2 the typical actuation strain of PZT ranges from 0.07% to 0.15%, while the typical actuation strain of SMA ranges from 1% to 7%, which is significantly larger.

These materials represent the typical actuation range of PZT material and can be divided into two groups. These two groups are hard PZT and soft PZT. Hard PZT represents the group of PZT material that has stiffer material properties. Soft PZT represents the group of PZT that has less stiff material properties. The level of actuation strain is dependent on the elastic modulus of the PZT and the piezoelectric strain coefficient. The piezoelectric strain coefficient describes the extent of electrical potential that supports actuation strain. This potential for actuation strain is dependent on the stiffness of the material. Two PZT materials with the same piezoelectric strain coefficients but different elastic moduli will produce different actuation strains. In Table 3.7 materials Pz 24 and Vibrit 202 are considered hard PZT and materials DuraAct P-876, Pz 29, and Vibrit 1100 are considered soft PZT. The actuation strains that these materials produce follow that the hard PZT support lower strains than the soft PZT, but their stiffer material properties help to distribute more of the induced stress to the substrate.

Figure 3.8 shows the stress reduction trend for the various PZT materials. The figure shows that as the induced stress increases the amount of stress reduction decreases as expected. The difference between the hard PZT and soft PZT materials is that the hard PZT trend plateaus more quickly than the soft PZT. This is due to the fact that the stiffer materials support a higher reinforcement, as one could say, that improves the composite action of the PZT and the substrate. The soft PZT begins to plateau at lower levels of stress reduction since it stiffness is lower. The plateau that is seen in figure 3.8 along the direction of increasing stress is discussed more in the next section which explores the separation of contributions between actuation of the actuator and the stiffness (reinforcement action) of the actuator.

Table 3.7 shows various piezoelectric materials and their piezoelectric and mechanical properties. The table is separated into soft and hard piezoelectric material. The DuraAct Patch, which is the main piezoelectric material used in this study, and two soft and two hard piezoelectric materials are selected from this table for the actuation strain parameter. All values shown in Table 3.7 are either taken directly from or derived from table 7.14 of Fundamentals of Piezoelectric Sensorics. This table is comprised of various commercially available PZT ceramic materials. These materials are similar to the DuraAct Patch but have varying actuation strains and mechanical properties.

As discussed before the various properties of these ceramics materials make them either soft or hard PZT. A soft PZT material supports a lower modulus of elasticity and higher actuation strains, while a hard PZT material supports a higher modulus of elasticity and lower actuation strains. The actuation strains at the bottom of Table 3.7 indicate the actuation strains recorded through ANSYS simulation of the actuation in free space. The actuator is modeled by itself in free space where it is subjected to a voltage potential and the actuation strain is recorded. These values are used for the actuation strain parameters in this study.

Table 3.7: Properties of Piezoelectric Materials

Property	Unit	Soft PZT						Hard PZT				
		DuraAct P-876	**Pz 29**	**N-10**	**Vibrit 1100**	**PZT 5H**	**APC 856**	**Pz 24**	**N-8**	**Vibrit 202**	**PZT 8**	**APC 841**
s_{11}	$e^{-12}\ \frac{1}{Pa}$	16.10	17.00	14.80	14.20	16.40	15.00	10.40	11.20	11.80	11.50	11.70
s_{33}		20.70	22.90	18.10	20.60	20.80	17.00	23.40	15.20	13.80	13.50	17.30
E_1	$e^9\ Pa$	62.11	58.82	67.57	70.42	60.98	66.67	96.15	89.29	84.75	86.96	85.47
E_3		48.31	43.67	55.25	48.54	48.08	58.82	42.74	65.79	72.46	74.07	57.80
ε_{11}	$e^{-8}\ \frac{F}{m}$	1.4685	2.1716	4.4500	4.2275	3.0260	3.6490	0.7209	1.2905	0.8900	1.1481	1.2015
ε_{33}		1.5575	2.5543	4.8416	4.0050	3.0260	3.6490	0.3622	0.8010	0.8900	0.9790	1.2015
d_{31}	$e^{-12}\ \frac{C}{N}$	-180	-243	-287	-315	-274	-260	-57.8	-99	-90	-97	-109
d_{33}		400	574	635	640	593	620	194	226	205	225	275
d_{15}		550	724	930	895	741	710	151	652	295	300	450
$\nu_{12,21}$	%	0.340	0.340	0.340	0.261	0.310	0.390	0.290	0.240	0.381	0.310	0.400
$\nu_{31,32}$		0.364	0.384	0.360	0.316	0.340	0.320	0.324	0.390	0.326	0.380	0.320
$\nu_{13,23}$		0.468	0.517	0.440	0.458	0.431	0.327	0.729	0.529	0.381	0.446	0.473
c_{11}	$e^9\ Pa$	120.60	133.87	123.71	106.29	100.12	112.20	239.53	164.61	145.09	157.09	174.34
c_{12}		74.22	89.97	73.29	50.45	53.57	64.24	165.00	92.60	83.72	90.70	113.29
c_{13}		70.95	85.95	70.92	49.53	52.26	56.46	131.07	100.31	74.59	94.16	92.04
c_{33}		100.00	109.68	106.31	79.84	83.61	94.95	127.67	144.03	121.09	145.63	116.71
c_{44}		21.15	19.38	23.46	24.14	21.30	24.46	27.81	29.19	30.68	30.07	29.01
c_{66}		23.18	21.95	25.21	27.92	23.27	23.98	37.27	36.00	30.68	33.19	30.53
$\varepsilon_{A\text{-}ANSYS}$	%	0.07	0.0945	0.1116	0.1225	0.1066	0.1011	0.0225	0.0385	0.035	0.0377	0.0424

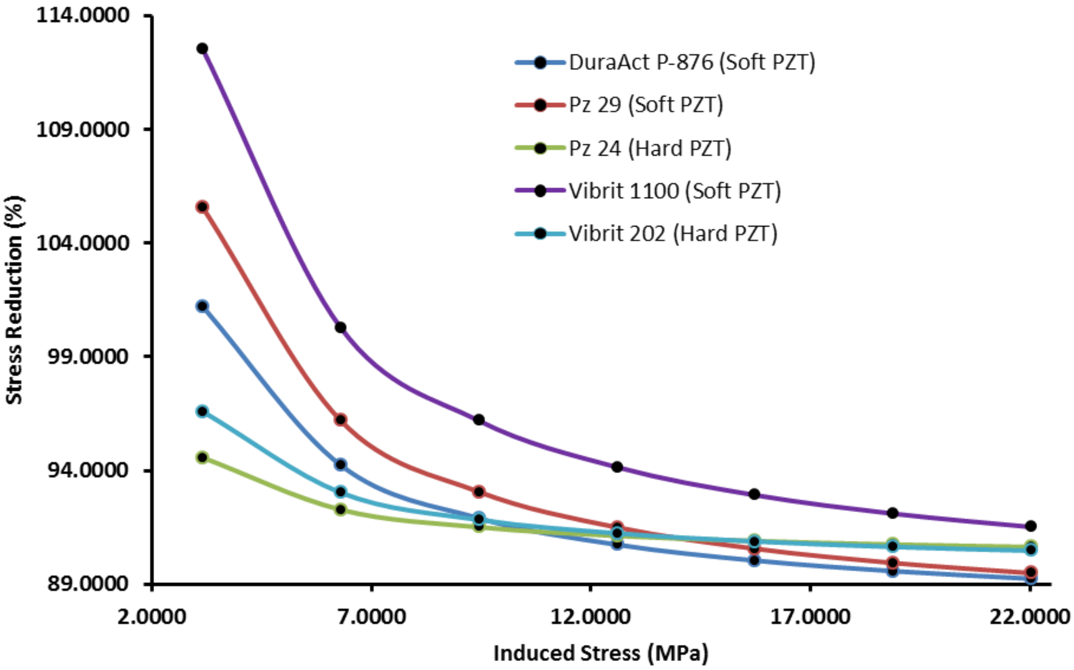

Figure 3.8: Stress Reduction for Various PZT Materials

3.4.4. Equivalent Patch – Post Study 1

In order to distinguish between the contribution to stress reduction of the actuator and its material stiffness these components must be separated. To do this a control simulation is done involving an equivalent patch. This simulation takes into account the mechanical material properties of the actuator without the contribution of the actuation capability based upon the DuraAct P-876 Transducer Patch. This is simply done by replacing the piezoelectric material model (ANSYS) with a general anisotropic material model (equivalent patch). The same equation for stress reduction is used and compared to the stress reduction recorded from the actuation simulations.

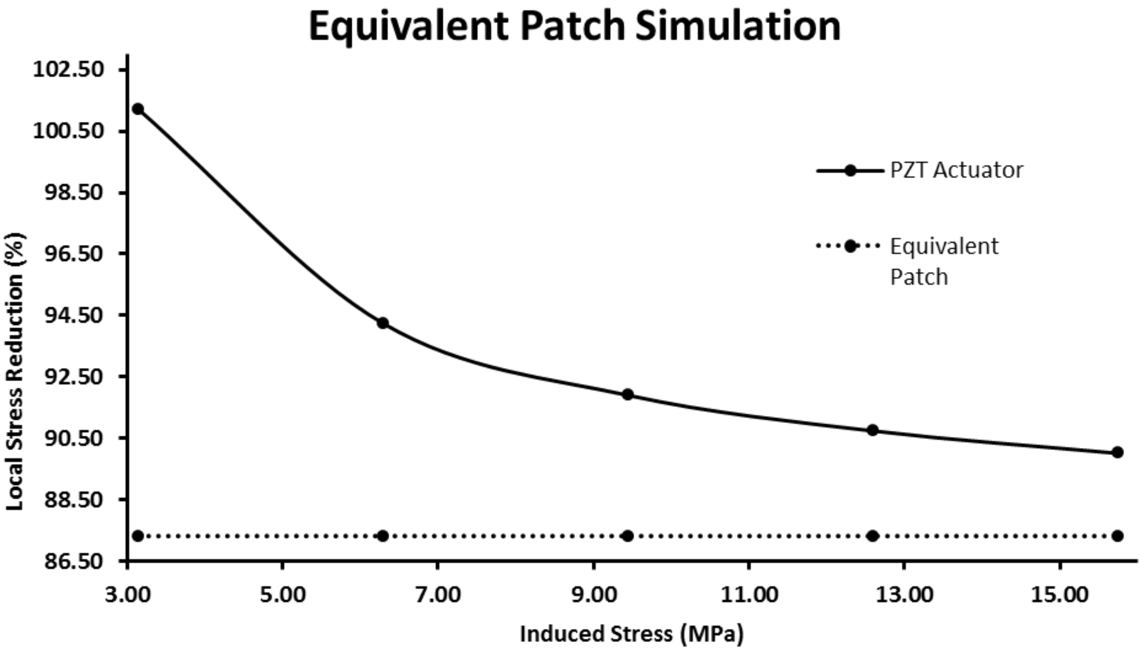

Figure 3.9: Equivalent Patch Simulation

Figure 3.9 compares a typical actuation simulation with its control equivalent patch simulation. The equivalent patch simulation shows that the stress found in the substrate remains proportional to the stress induced on the substrate, producing a constant stress reduction regardless of the amount of induced stress. Note that the stress reduction is determined by comparing the stress found in the substrate to the stress induced in the substrate. In the case of the equivalent patch simulation the only stress reduction component is the reinforcement action of the actuator acting as a composite system with the substrate. It then makes sense that the stress reduction remains constant as the stress increases. The composite action of the actuator/substrate composite directs stress to the individual material according to ratio (or difference) between their individual elastic moduli. Therefore no matter how much stress is induced on the substrate the same percentage of that stress is reduced by the reinforcement action or stiffness increase that the actuator offers to the substrate.

By separating out the contribution of the material stiffness, the contribution of the actuation ability to stress reduction can be more clearly seen. This contribution decreases as the induced stress increases and as seen in section 3.4.3. of this chapter where the the stress reduction begins to plateau at higher stresses. This plateau corresponds to the reinforcement action of the material for which at some point of increasing stress there will be no visible stress reduction remaining due to actuation. The only stress reduction component remaining will be the material stiffness unless at some point either material yields for which this study does not take into account.

3.4.5. Common Stress Point – Post Study 2

The induced stress parameter discussed in section 3.4.3 describes the behavior and potential for stress reduction by the actuator when the stress induced upon the system is varied. This induced stress analysis can be further explored by varying the stiffness of the system in respect to the substrate. The common stress point is obtained by the addition of this parameter. Figure 3.10 shows the common stress point produced by varying the elastic modulus (stiffness) of the substrate.

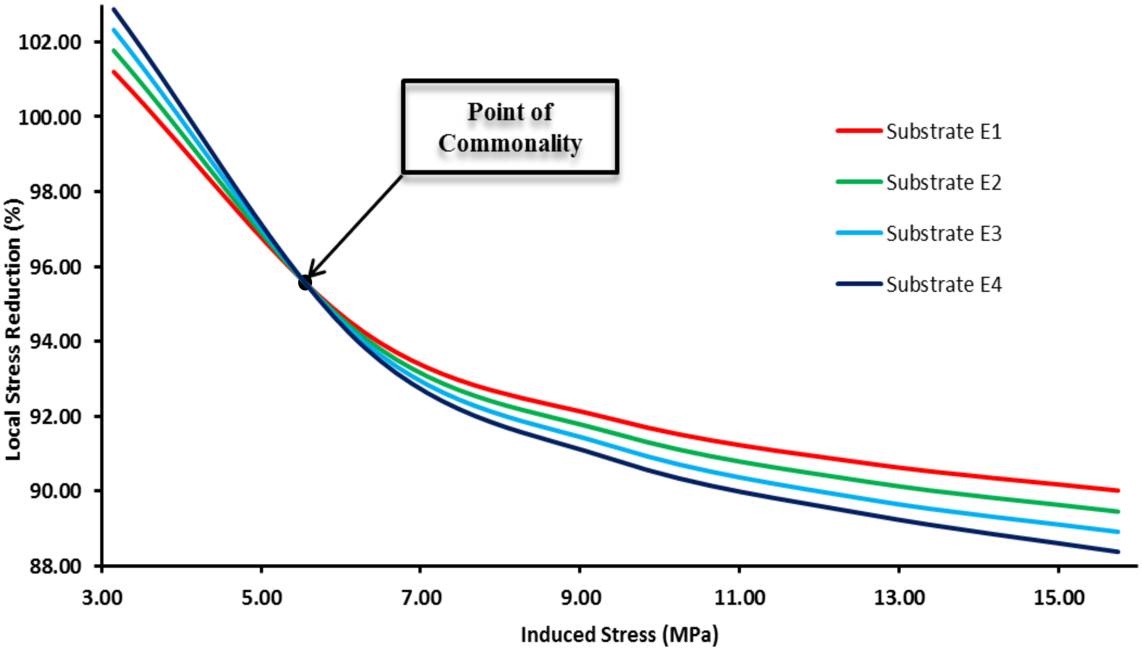

Figure 3.10: Point of Common Stress

The typical trend for stress reduction versus induced stress can be seen in Figure 3.10. By varying the substrate modulus the trend becomes different for each substrate modulus. As declared in Table 3.1 substrate E1 ($E_{S\text{-}1}$) through substrate E4 ($E_{S\text{-}4}$) are increasing in stiffness, E1 representing the substrate with the lowest stiffness and E4 representing the substrate with the highest stiffness. The four curves show that at some common point of induced stress the stress reduction is the same for all substrate parameters. At stress levels higher than this common stress point the substrate E1 shows greater stress reduction and at the stress levels lower than the common stress point E4 shows greater stress reduction.

By increasing the stiffness of the substrate, the composite action relationship between the substrate and the actuator is altered. As the stiffness of the substrate increases the percentage of stress distributed to the substrate also increases, resulting in a lower stress reduction. Figure 3.11 shows the trends of the equivalent patch analysis for each substrate parameter. The substrate with the highest stiffness shows the lowest stress reduction as is expected. This holds true for stress levels higher than the common stress point, but at stress levels lower than the common stress point the substrate with the highest stiffness shows reversely the highest stress reduction.

This is caused by the fact that the actuator has a constant actuation strain, but each substrate, having a different, elastic modulus, is stressed differently because of varying differences in stiffness. The stiffer the substrate the less strain is required to induce the same amount of stress. Table 3.4 shows that this is evident with the non-stresses state simulation where no external stress is present. The equation for young's modulus ($\sigma = E \times \varepsilon$) also is evidence of this, where stress is a function of both elastic modulus and strain. The results show that the substrate with a higher stiffness (elastic modulus) accrues more stress, with the same actuation strain acting upon it, than the less stiff substrate.

For a simulation with external stress involved, this becomes apparent as the induced stress decreases to a level at which the internal stress from the actuator is strong enough to start to show effects on the substrate as would be seen during the non-stress state simulation done in section 3.4.1. This middle ground between external stress (induced stress) and the countering internal stress (actuation stress) is this common stress point. The relationship between external stress (induced stress) and internal stress (actuation strain) determines where this common stress point occurs. A more powerful actuator generating higher actuation strain will produce a common stress point at higher stress levels.

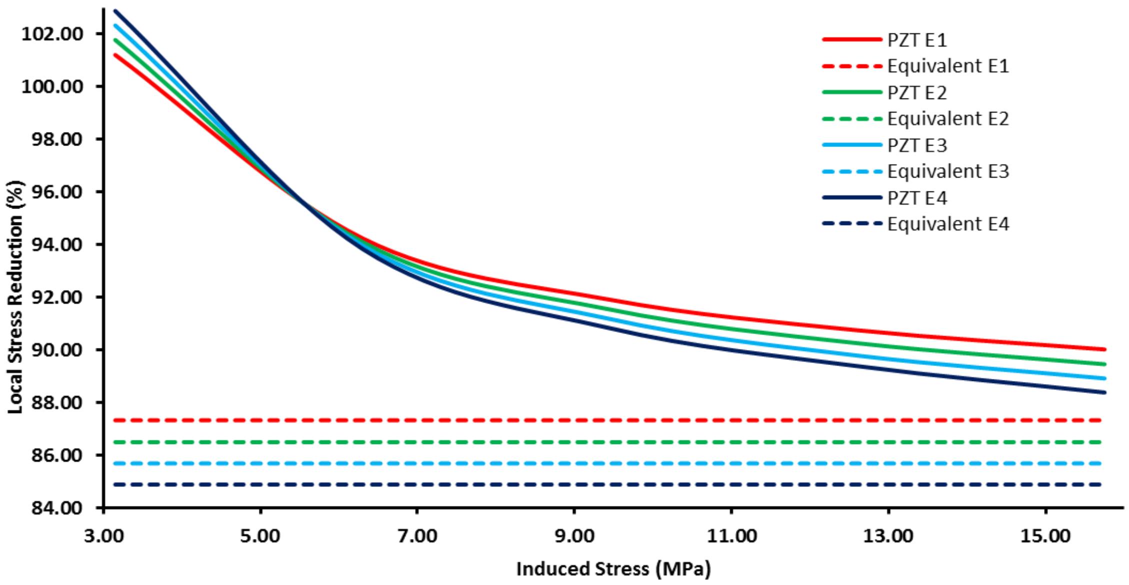

Figure 3.11: Point of Common Stress & Equivalent Patch

3.5. Conclusions

The results of this parametric study show the various components that can make up and affect the ability of an actuator, be it PZT, SMA or any other mechanical actuator, in reducing stress within a given material. This study is to serve a glimpse into the most important components of stress reduction for actuators applied to a substrate surface. Some of these most important components are geometric conditions of the substrate and actuator, mechanical properties of the substrate and actuator comparatively and the amount external stress applied to the substrate versus the amount of stress applied internally from the actuator (actuation strain).

It can be seen that the actuation strains of PZT are generally too low to be effective with high stress level applications. The highest stress levels used in the PZT simulations are around 15.75 MPa which distributed over the cross sectional area of the substrate is around 5,000 N or

1,124 lbs. The highest stress levels used in the SMA simulations (during the induced stress parameter study) are around 125.98 MPa which distributed over the cross sectional area of the substrate is around 40,000N or 8,992 lbs. The induced stress parameter showed that the ability of the actuator to reduce stress solely by means of actuation diminishes greatly when the induced stress levels reach that 15.75 MPa point. The actuation strains of SMA show greater potential for being used for higher stress level applications. With an average actuation strain of around 4% and the ability to be able to counter stress levels resulting from almost 9 kips of load, the potential for stress reduction solely by means of actuation can be applied at higher more practical stress levels which can benefit a wider range of applications.

CHAPTER 4. SMA MATERIAL TESTING

4.1. Introduction

This chapter discusses lab testing that was conducted on shape memory alloy wires in an attempt to simulate typical shape memory behavior. The tests conducted in this chapter are based upon results found in “Shape Memory Alloys: Modeling and Engineering Applications” by Dimitris C. Lagoudas. The three shape memory behaviors that are tested for are shape memory detwinning, pseudoelastic behavior and isobaric response of shape memory alloy. The goal of these tests are to successfully achieve similar and typical testing results for these particular behaviors in accord with results found through research of relevant literature like literature referenced above.

4.2. Material Characteristics and Testing Procedures

4.2.1. Material & Specimen Preparation

The material used for the shape memory alloy tests described in this chapter is a nitinol (SMA) wire called Flexinol ®, supplied by Dynalloy Inc. These wires are electrically driven and are a good basic shape memory material to explore and test. The wire is supplied in a spool of wire and is cut into lengths appropriate for small tension testing about 381mm to 406mm (15” to16”). The wires are wrapped around and clamped between two steel coupons, which are then clamped by the loading frame clamps.

The steel coupons are cut in 2 inch long strips and the cut edges are grinded down to prevent the sharp edges from damaging the wire during clamping. Two holes are drilled in one of the coupons for which the SMA wire specimen is wrapped around. The wire is than clamped by the other coupon. The steel coupons are taped together around the SMA wire and the excess wire is allowed to extend out from the coupons on each end. This allows for the crimp connectors to be attached for the electrical powering of the SMA wire.

The electrical powering of the SMA wire is done through a 10 amp 30 volt power supply. The excess wire left out of the coupons is attached to a wire that is connected to the power supply. By attaching the positive wire from the power supply to one wire end of the specimen and the negative wire from the power supply to the other wire end of the specimen a circuit is created for which electrical current can flow through the wire. By allowing current to flow through the wire internal resistance is created which generates heat within the wire which promotes transformation of the SMA. In fact at higher current levels (about 4 to 5 amps) the SMA wire heats up rapidly which creates a faster actuation of the wire. The specific SMA wire used in these tests has an austenite transformation start temperature of around 90°C and an austenite finish temperature of around 110°C. The applications that typically use this type of SMA are applications such as small electrical switches, tensioning (pulling devices) and other things that need fast actuation. The current supplied must be carefully regulated so that the temperature of the SMA wire is maintained within this temperature range. The manufacturer’s electrical powering guidelines dictate a 4 amp current supply to initiate a one second contraction, therefore a 1 second temperature change from room temperature to austenite finish temperature (110°C). Preferably the temperature should be at or above the austenite finish temperature to ensure total transformation or actuation of the wire. The temperature of the wire was measured through the use of a thermo couple attached to the SMA wire. Repeated exercises were conducted using the thermal couple to measure temperature of the SMA wire and to ensure the successful attachment of the thermal couple. Through these repeated exercises and after a consistent temperature recording was achieved, the required current supply needed to achieve and maintain a temperature of 110°C (Austenite finish temperature (A_f)) was around 2.1 to 2.2 amps. This is the current that gradually brings the SMA to the final transformation temperature (A_f) and maintains the temperature. This is different than the manufacturer's recommendation of 4 amps for one second transformation for which would continue to increase after one second to extreme temperatures, which would burn up the SMA. An extreme temperature experiment was done applying tension on the wire while to high current (about 5 amps) and the SMA became so hot that it became like a filament which burned and melted away. See the end of this chapter for powering considerations for the SMA wires.

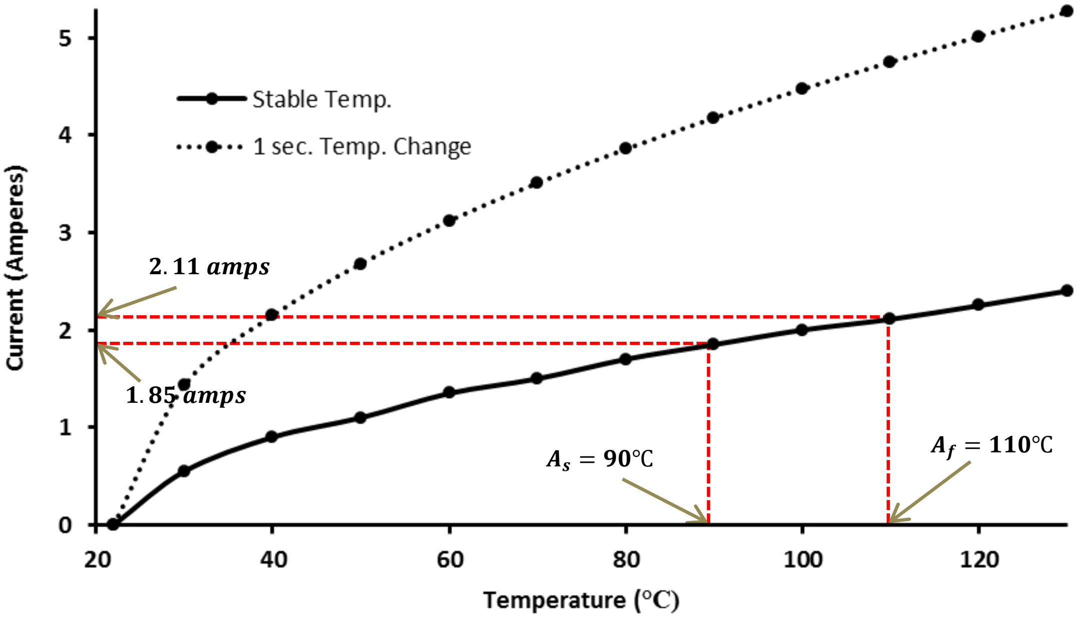

Figure 4.1: Powering Requirements for Nitinol SMA Wires

Table 4.1: Calculated Electrical Powering of SMA Wire

<table>
<tr><th colspan="10">ELECTRICAL POWER OF SMA WIRES</th></tr>
<tr><th colspan="5">Governing Equations</th><th colspan="5">Material Properties</th></tr>
<tr><td colspan="5">$I\ (Current) = \frac{V\ (Voltage)}{R\ (Resistance)}$
$P\ (\mathrm{Power}) = I^2 \times R$
$\Delta E = mC\Delta T \Rightarrow P = mC\frac{dT}{dt}$</td><td colspan="5">$Density: 0.00645 g/mm^3$
$Resistance: 0.0043\ \Omega/mm$
$Specific\ Heat\ (C): 0.8368 J/g \cdot ℃$
$Wire\ Mass (m): 0.3953\ g$
$Wire\ Length: 300 mm$</td></tr>
<tr><th>Temperature (°C)</th><td>40</td><td>50</td><td>60</td><td>70</td><td>80</td><td>90</td><td>100</td><td>110</td><td>120</td></tr>
<tr><th>Power (Watts)</th><td>5.62338</td><td>8.93125</td><td>12.2391</td><td>15.547</td><td>18.8549</td><td>22.1627</td><td>25.4706</td><td>28.7785</td><td>32.0863</td></tr>
<tr><th>Current (Amps)</th><td>2.087872</td><td>2.63124</td><td>3.08021</td><td>3.47159</td><td>3.82311</td><td>4.14493</td><td>4.4435</td><td>4.72323</td><td>4.9873</td></tr>
</table>

The current needed to induce the desired temperature in the interval of 1 second is shown in Table 4.1. Supplying this constant current longer than 1 second will continue to heat the wire and produce a higher internal temperature. This is undesirable when a constant temperature is needed. Since at some point the temperature will become constant, the theoretical current needed to achieve a constant temperature can be calculated. This current being a lower current, for which builds up to the constant desired temperature, does not produce rapid actuation like the higher current levels. In this case the shape memory alloy transformation will occur over some longer time period. Current needed for maintaining constant temperatures witnessed through experiments are shown in figure 4.1.

Figure 4.2: Test Set-up of SMA Wire Specimen

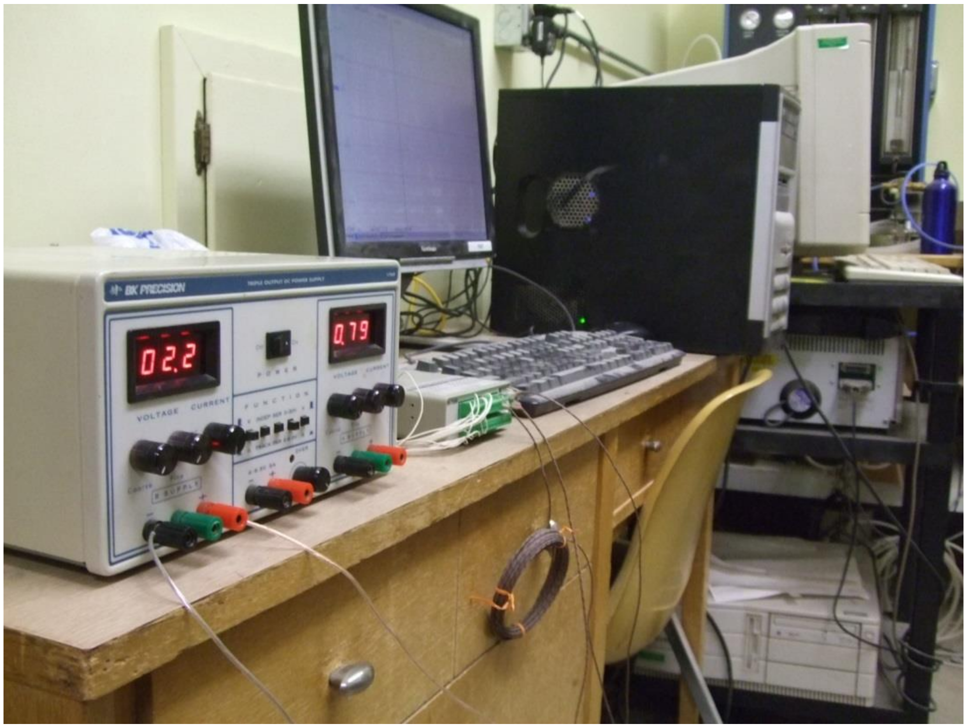

Figure 4.3: Equipment Set-up for SMA Wire Test

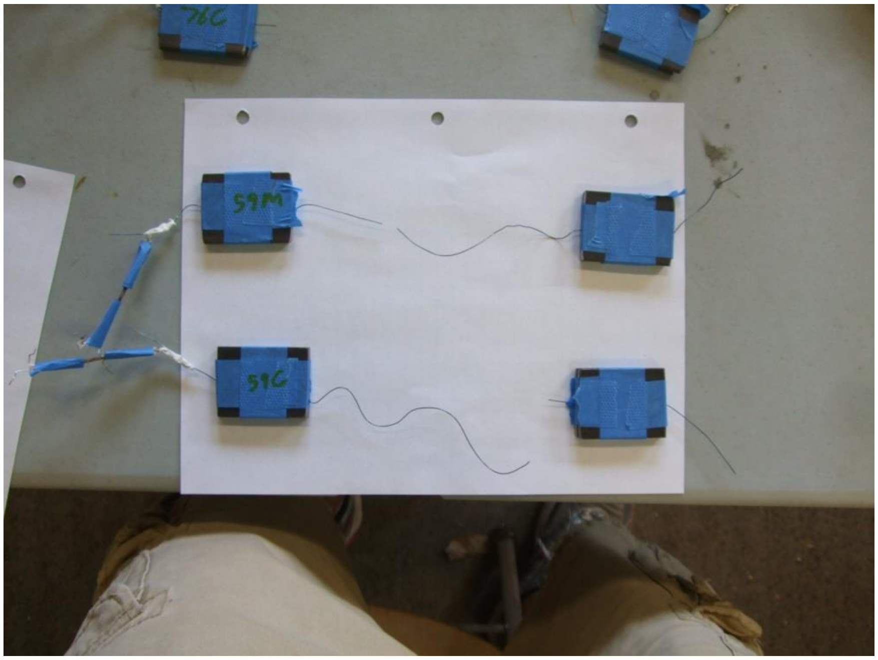

Figure 4.4: SMA Wire Test Failed Specimens

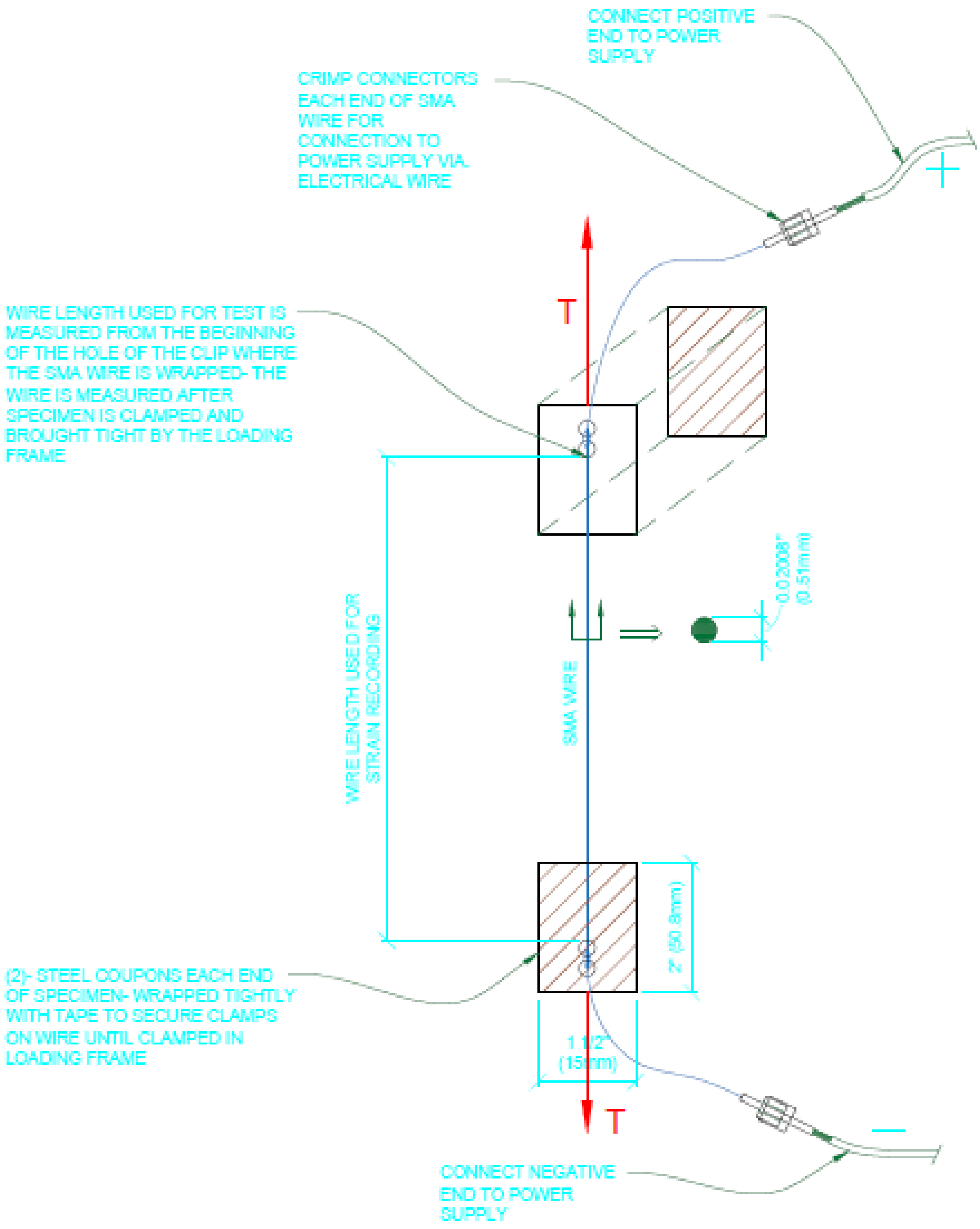

Figure 4.5: SMA Wire Test Schematic

4.2.2. Testing Schemes

There are three different testing schemes performed during the testing of the SMA wires. The first is a simple monotonic loading of the specimen to failure without any electrical powering of the wire. The purpose of this test is to explore the failure characteristics of the material as well as the detwinning characteristics of the material, which is the detwinning of twinned martensite to detwinned martensite.

The second test is a pseudoelastic test which showcases the superelastic characteristics of the SMA. This test involves the electrical powering of the SMA wire (2.1 amps) so that the austenite finish temperature is reached and maintained during the tensioning of the wire. The pseudoelastic or super-elastic ability of the material is of interest in this test. At temperatures beyond the austenite finish temperature (A_f=100°C) the material should be able to be detwinned completely and then during the slow release of the load should be able to regain almost all of the plastic deformation witness during the detwinning. This characteristic is the epitome of the shape memory effect.

The third test is what is called an isobaric test. This test involves the loading of the SMA wire, which is already detwinned, at room temperature (or below non-transformative temperatures) to a desired load and holding that load. While the load remains constant the temperature of the wire is raised gradually from room temperature to beyond the austenite finish temperature (A_f=100°C) and the strain is recorded. The loading frame used for these tests takes a little time each time the temperature is raised to bring the load back to the constant load, so temperatures increments are used for which the strain is recorded at each increment.

4.3. Testing Results

4.3.1. Shape Memory Alloy Detwinning

The process of detwinning the SMA wire was accomplished through many trial tests. One difficult task was to maintain the clamping of the wire. During the first trial tests the wire was only clamped between the steel clips and was not wound, like detailed in Figure 4.5. Without winding the wire, the wire would slip within the clamp and unwarranted strain was recorded. After introducing the two holes in the steel clips, and winding the SMA through them, the detwinning of the wire was accomplished rather quickly. The results are shown in Figure 4.6.

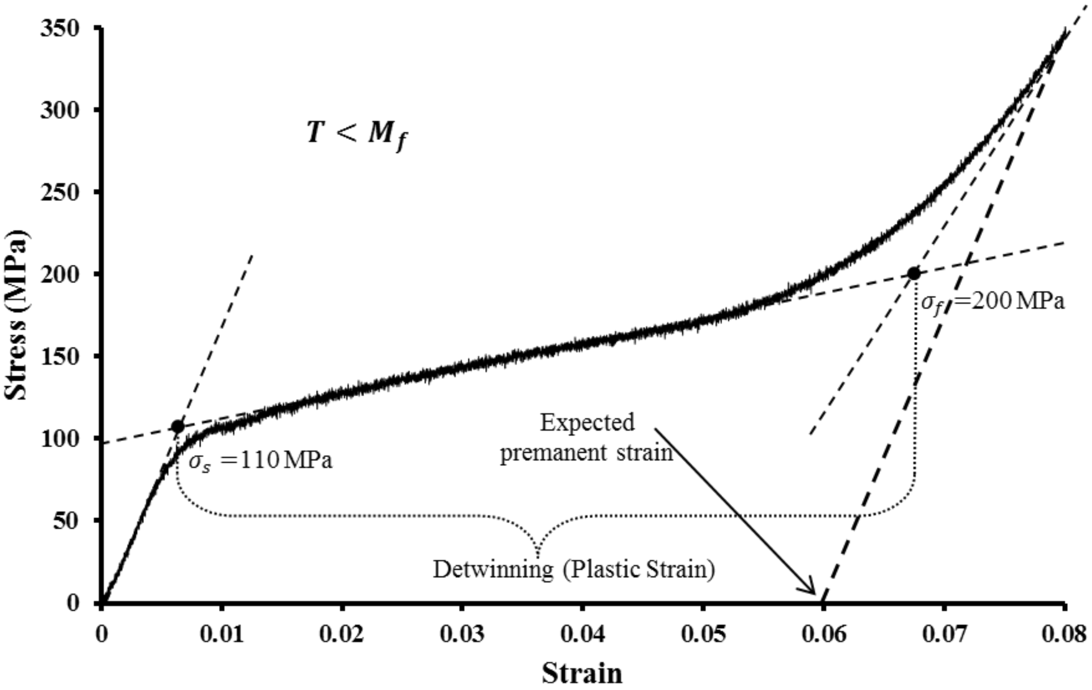

Figure 4.6: SMA Detwinning (Monotonic Loading)

The results obtained show that the detwinning start stress (σ_s), resulting from the intersecting tangents of the elastic to plastic curve, is around 110 MPa. This stress level results from a tension load of 22.5 N, induced on the wire. The detwinning finish stress (σ_f), resulting from the intersection tangents of the plastic to hardening curve, is around 200 MPa. This stress level results from a tension load of 40.9 N, induced on the wire. Typical detwinning stresses for nitinol shape memory alloy material are between 100 MPa and 200 MPa. This shows that the test was successful in achieving the detwinning curve of the material. Typical detwinning stresses were found in “Shape Memory Alloys: Modeling and Engineering Applications” by Dimitris C. Lagoudas. The detwinning figure 4.6 declares that the temperature during this test was below the Martensite finish temperature (M_f). This signifies that the shape memory alloy is at a completely martensite phase. See figure 2.3 in chapter 2 for more details on the four temperature phases.

4.3.2. Pseudoelastic Test

To create the pseudoelastic curve for the material, the SMA wire is tensioned to a level that shows that significant detwinning has occurred and then is unloaded slowly. If the SMA wire is kept at the austenite finish temperature hysteresis should be witnessed and the recovery of the plastic deformation should happen.

Figure 4.7a shows the recorded results for the pseudoelastic tests performed on the SMA wire. Through many trials a desirable pseudoelastic curve was able to be replicated based on research and results found in “Shape Memory Alloys: Modeling and Engineering Applications” by Dimitris C. Lagoudas. Figure 4.7b show figure 2.30b from this reference which gives an example of a pseudoelastic curve of an untrained specimen. The results show detwinning of the specimen during the forward loading phase. During the unloading phase, the deformation due to detwinning is somewhat recovered, which is visual evidence of the shape memory effect. As can be seen in Figure 4.7a there is incomplete recovery of the plastic deformation. This is due to the fact that the specimen is an untrained specimen. This particular SMA wire would have to be trained through mechanical or thermal cyclic loading in order to get full recovery or full hysteresis while utilizing its pseudoelastic abilities.

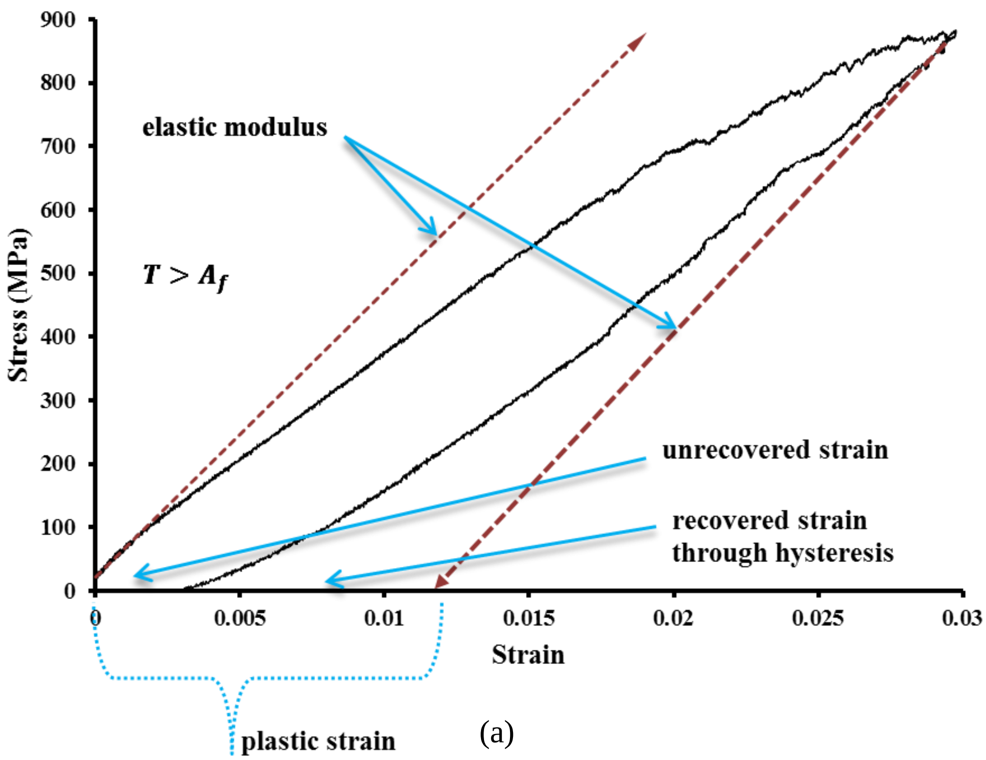

(a)

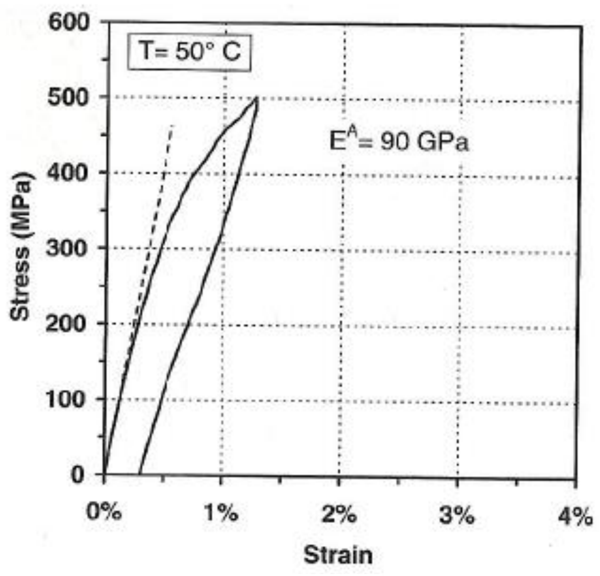

(b)

Figure 4.7: (a) Pseudoelastic Testing (Austenite); (b) Fig. b “Shape Memory Alloys: Modeling and Engineering Applications

Another thing to note pertaining to Figure 4.7 is the typical loading curve of austenitic SMA (Figure 4.7) compared to the loading curve of martensitic SMA (Figure 4.6). The detwinning is very much apparent in the martensitic SMA loading curve than in the austenitic SMA curve. It is important to note that both the martensitic and austenitic specimens were untrained. This factor affects the austenitic SMA specimen rather more significantly than the martensitic SMA specimen. The austenitic SMA being in a sense the higher level phase (having more mechanical stiffness) requires higher levels of stress to be detwinned. Also during the loading phase of the austenitic SMA there are microstructure impurities that are reordered and initially act as stiffness enhancers, but after the training of the material these impurities are removed and the austenitic material becomes more easily detwinned. And also becomes better at achieving full recovery during the shape memory effect. Training and microstructure impurity considerations are taken from “Shape Memory Alloys: Modeling and Engineering Applications”.

4.3.3. Isobaric Testing

The isobaric test involves maintaining a constant load on a detwinned SMA wire while the wire is subjected to increasing temperature. The loading instrument is programmed to modify the extension of the loading frame when external load is detected. As the SMA wire begins to contract because of the shape memory effect, the loading frame shortens the extensions in order to maintain the constant load.

The detwinned SMA wire, which is about 1500mm in length, is loaded to the constant load of 50 N. The temperature is than increased, in 10°C increments using the current required for stable temperature increase shown in figure 4.1, from room temperature (23°C) to 130°C which is above the austenite finish temperature. The constant load of 50 N, which corresponds to about 245 MPa in stress, was chosen because the wire was previously detwinned using the same load. This is apparent since the loading curve for the initial startup of the isobaric test, shown in Figure 4.8, is linear.

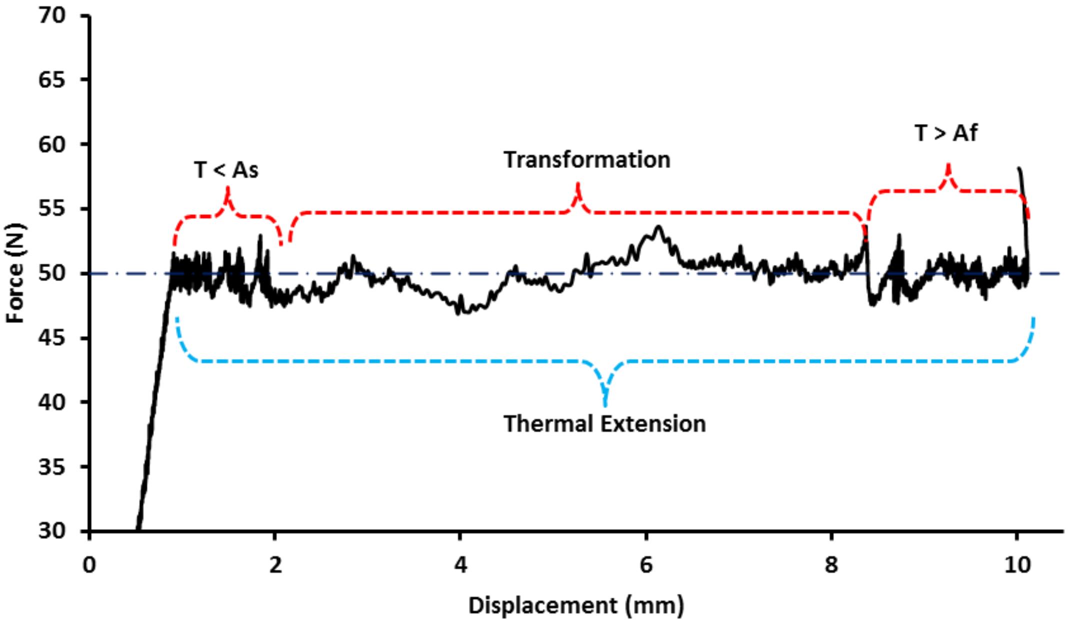

Figure 4.8: Isobaric Testing Results

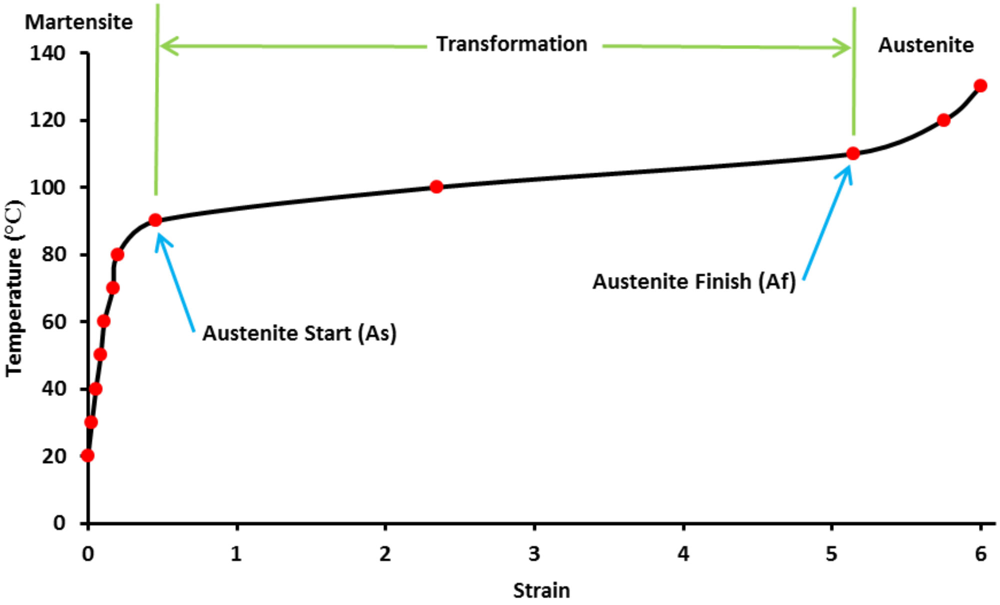

Figure 4.9: Shape Memory Alloy Isobaric Curve

Figure 4.8 shows the recorded data from the isobaric test. After every temperature increase the load cell shows load spikes where external load from the SMA contraction is detected. Upon detecting these changes in load the load frame modifies the extension of the frame to accommodate these loads in order to maintain the constant loading of the wire. This is how the strain of the wire is recorded. When the loading frame stops adjusting, the strain (calculated from displacement) is recorded by hand for that particular temperature. In Figure 4.8 the transformation of the SMA from martensite to austenite can be easily seen graphically. These results, in terms of temperature and strain, can be seen in Figure 4.9, which shows the isobaric curve of the material. A typical isobaric curve also includes the back transformation of the material, which involves a hysteresis curve, such like the hysteresis curve in the pseudoelastic test. The back transformation was not induced because it was not possible to achieve with the equipment available to this research. The SMA wires, through electrical current, generate rapid internal heat which causes forward transformation of the material. In order to cause backward transform the temperature is decreased. For electrical powered SMA applications this cooling is hard to control and usually results in these types of applications, these experiments included, being designed around the forward transformation and not the backward transformation. Other applications which utilize both the forward and backward transformation of SMA employ a controlled environment where external temperature change can be controlled more accurately using forced heating and cooling utilizing an enclosed environment around the specimen.

4.4. Testing Conclusions

The purpose of these tests were to gain a working knowledge of the material by mimicking typical tests witnessed through the general research of the material. These main tests help to gain practical knowledge of the limitations that the shape memory alloy has. These limitations can be seen through the weaknesses of the testing procedure that has been presented below.

First, the wrapping and clamping of the wire between the two steel clips presented some difficulties in securing the wire sufficiently. Many tests were down in vain, where there was additional unwanted strain recorded because of wire slipping between the clamps. Being aware that there are techniques, not utilized here, that can securely clamp the material; this can be deemed as one of the major weaknesses of the SMA wire testing procedure presented in this chapter. One thing to take from this though, would be the understanding that the SMA wire can be difficult to connect or adhere to substrates. Welding of the shape memory alloy is difficult to accomplish even between the material itself, let alone a steel substrate for example. One possible way of through adhesion by epoxy retrofits, which presents its own challenges. The large strains of the SMA, degrades the epoxy bond between the materials through mechanical means as well as thermo means. If a typical SMA is used for application, such as the type used for these tests, the SMA must be heated to engage the transformation. This also degrades the epoxy for which high temperature epoxies must be used.

Secondly, the method for heating the SMA wire is done through electrical means. This means of shape memory alloy actuation is well suited for fast actuation of the material as used for applications involving switches and fast mechanical movements, but for applications involving sustained actuation of the shape memory a way of inducing temperature change through ambient methods would be more suited. The main downfall of electrical powering is the fact that the current supplied to the wire not only achieves the desired temperature change, but continues to increase in temperature. The electrical power, being joules per second, maintains that the wire will receive a constant energy increase. Flexinol (Nitinol) manufacturer recommendation for a 1 second transformation of the wire is 4 amps. Although after 1 second the temperature will begin to increase dramatically. It can be determined that the same transformation can be achieve through a lower amperage over a longer time interval. As discussed earlier in this chapter this has been achieved for this thesis work through experimental work with thermal couples (see Figure 4.1).

Through these lab tests, three SMA material characteristics were calculated. The elastic modulus of Austenite ($\boldsymbol{E_{Aust.}}$) was calculated around 6,078,500 psi, the elastic modulus of Twinned Martensite was calculated around 1,337,900 psi and the elastic modulus of Detwinned Martensite was calculated around 2,030,500 psi. The only value used for design purposes in this thesis is the elastic modulus of detwinned martensite, which is used as the SMA elastic modulus for the beam retrofit simulations in section 5.1 and 5.2 of chapter 5. The elastic modulus of Austenitic SMA for simulations in chapter 5 pertaining to the column buckling simulations is referenced from a different shape memory alloy material, which is different from what was tested in this chapter.

The actuation strain found in the isobaric material testing is recorded around 6% total strain resulting from detwinned martensite SMA. A typical SMA actuation strain ranges from 1% to 7%. For the parametric study in chapter 3, and the beam retrofit models in chapter 5 (5.1 & 5.2), the actuation strain was conservatively chosen to be 4% strain. Although the 6% strain was recorded for the SMA wires that were tested, the parametric actuator and beam retrofit simulations in chapter 3 and 5 implement plate type actuators which may not necessarily produce the same actuation strain. With this consideration in mind a conservative mid-range typical actuation strain was chosen for simulations involving SMA actuation.

CHAPTER 5. STRUCTURAL APPLICATIONS USING FINITE ELEMENT SIMULATIONS

5.1. Introduction

Two l applications involving shape memory alloys have been explored and theoretically analyzed using the finite element method. The first application involves the actuation mechanism (shape memory effect) of shape memory alloys and the second examines the benefit of the pseudoelastic (superelastic) properties in providing structural stability in the context of high temperature buckling scenarios.

Both these applications involve the attachment of shape memory alloys to structural steel members. The connection between the SMA and the steel component is crucial in understanding the effect that the retrofit may have on the steel. Complete and pure attachment between the SMA and the steel components is rather hard to achieve and a realistic method must be established and explored. There are several practical ways that SMA may be attached as a retrofit, but the two most applicable and feasible ways are presented in Section 5.2. The effects that the attachment method has on these applications are included in this chapter.

In section 5.3.1 the shape memory effect or actuation of the shape memory alloy is explored by simulated a beam retrofitted with a SMA plate and subjected to actuation strain from the SMA. In section 5.3.2 the pseudoelastic effect of the shape memory alloy is explore through the retrofitting of a wide flange column for the purpose of strengthening the column during building fire conditions.

5.2. Shape Memory Retrofit Attachment Method

There are two plausible methods for connecting shape memory alloy to structural steel members. The first is a rather common method involving epoxy adhesive. This method is traditionally used in fiber composite retrofitting. This method is very applicable to fiber composites since the fiber material is already supported by an epoxy matrix. The retrofit is made directly on the structural member by applying plies of fiber composites and applying the epoxy with each layer. This method is possible when considering shape memory alloys as the retrofit, but there are some problems when considering its mechanical abilities. First, the shape memory effect supports very large mechanical strains which in turn create large surface stresses along the epoxy/steel interface. In most cases the failure of the epoxy bond to the substrate will control most failure modes. Another problem is that some shape memory alloys must be heated to rather high temperatures which would degrade the epoxy adhesive and hinder its ability to maintain surface adhesion as well as degrade the stiffness of the epoxy allowing the interface between the steel and SMA to elongate. High temperature epoxy adhesives could also be used, but still pose the problem of large actuation strains created by the SMA retrofit. With these concerns in mind, an alternative retrofit method for shape memory alloys is explored.

A second alternative method involves mechanical bolt fastening of the SMA retrofit to the structural member. Utilizing pretensioning of bolt fasteners to produce frictional anchorage, the retrofit can be attached to the structural members while not being susceptible to the above described mechanical concerns associated with epoxy adhered retrofits.

Bolt pretensioning attachment of the retrofit can create a complex analysis for the applications in this chapter. The models used in this chapter, simplify the retrofit attachment by using a pure and complete attachment, or bonding, of the contact surfaces between the SMA retrofit and the structural member. Understanding that this is ideal but unrealistic, a comparison between a bolted retrofit scenario and a purely bonded retrofit scenario must be considered. This chapter entertains this comparison and concludes with some general considerations for realistic attachment of SMA to steel.

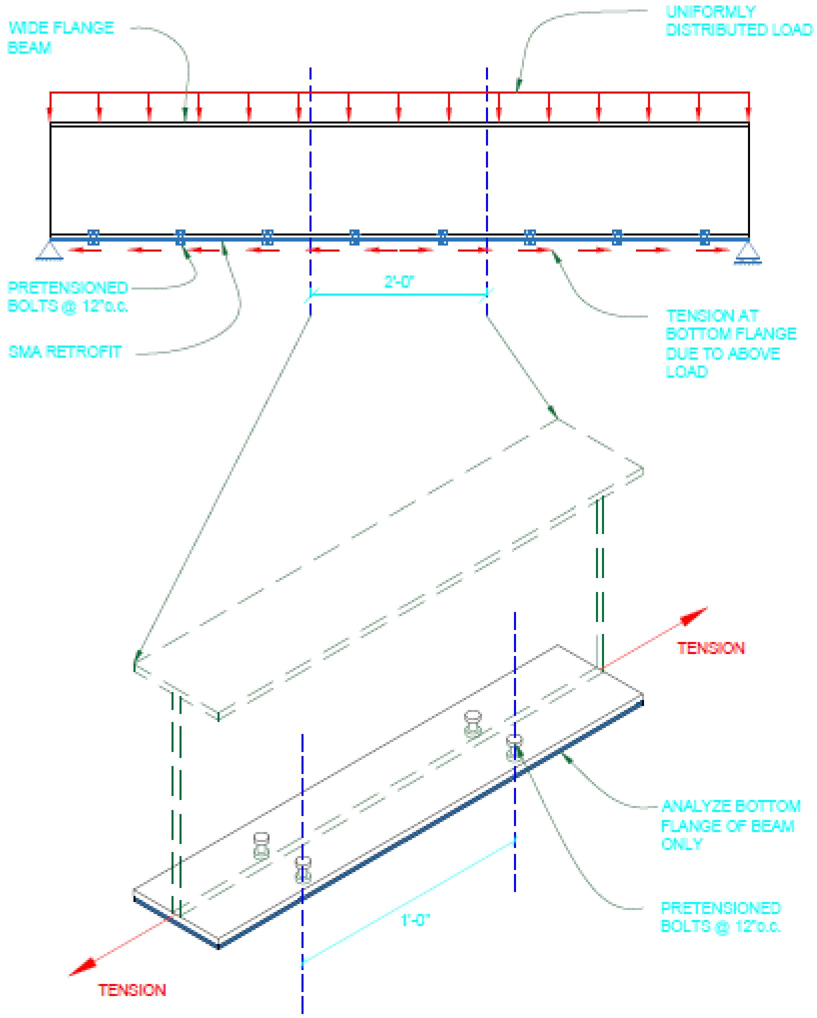

Figure 5.1: Pretensioned Bolted SMA Retrofit Anchorage Detail

5.2.1. Exploratory Model

In order to explore the differences between the completely bonded attachment of the SMA retrofit to the more realistic bolted attachment, a finite element model & analysis, utilizing bolt pretensioning methods, is developed. This model simplifies the retrofitted beam geometry and looks entirely at the bottom flange of the beam where the retrofit is attached. At this location, during positive bending of the beam, the bottom flange encounters mostly normal tension stress, which the bonding elements must resist in the form of shear stress. To simplify this, just the bottom flange, of a W16x26 wide flange beam, is modeled and the beam flange portion of the model is subjected to a tension load. Two loading conditions of the model are explored. The first tests the anchorage abilities of the bolted assembly while subjected to an external tension and the second tests the anchorage abilities of the bolted assembly while subjected to an internal actuation force by the SMA retrofit while the beam flange is fixed both ends.

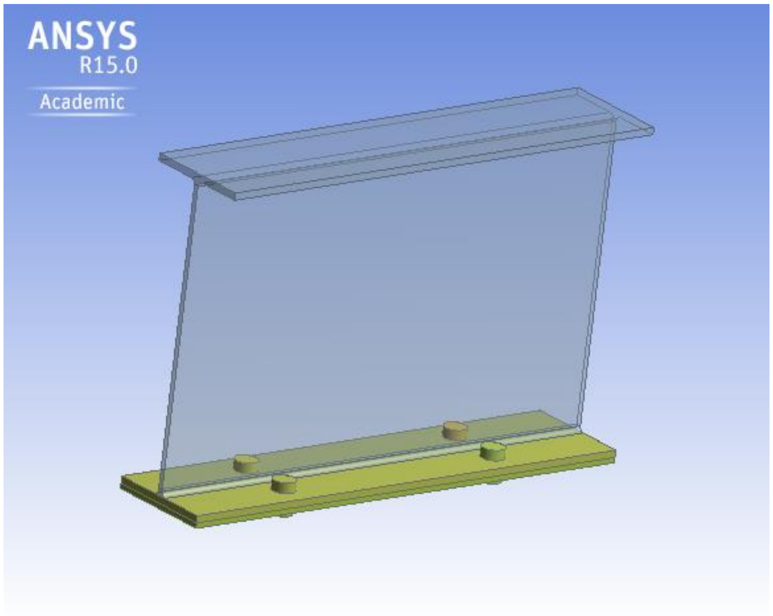

Figure 5.2: Bolted Attachment FEA Model Geometry

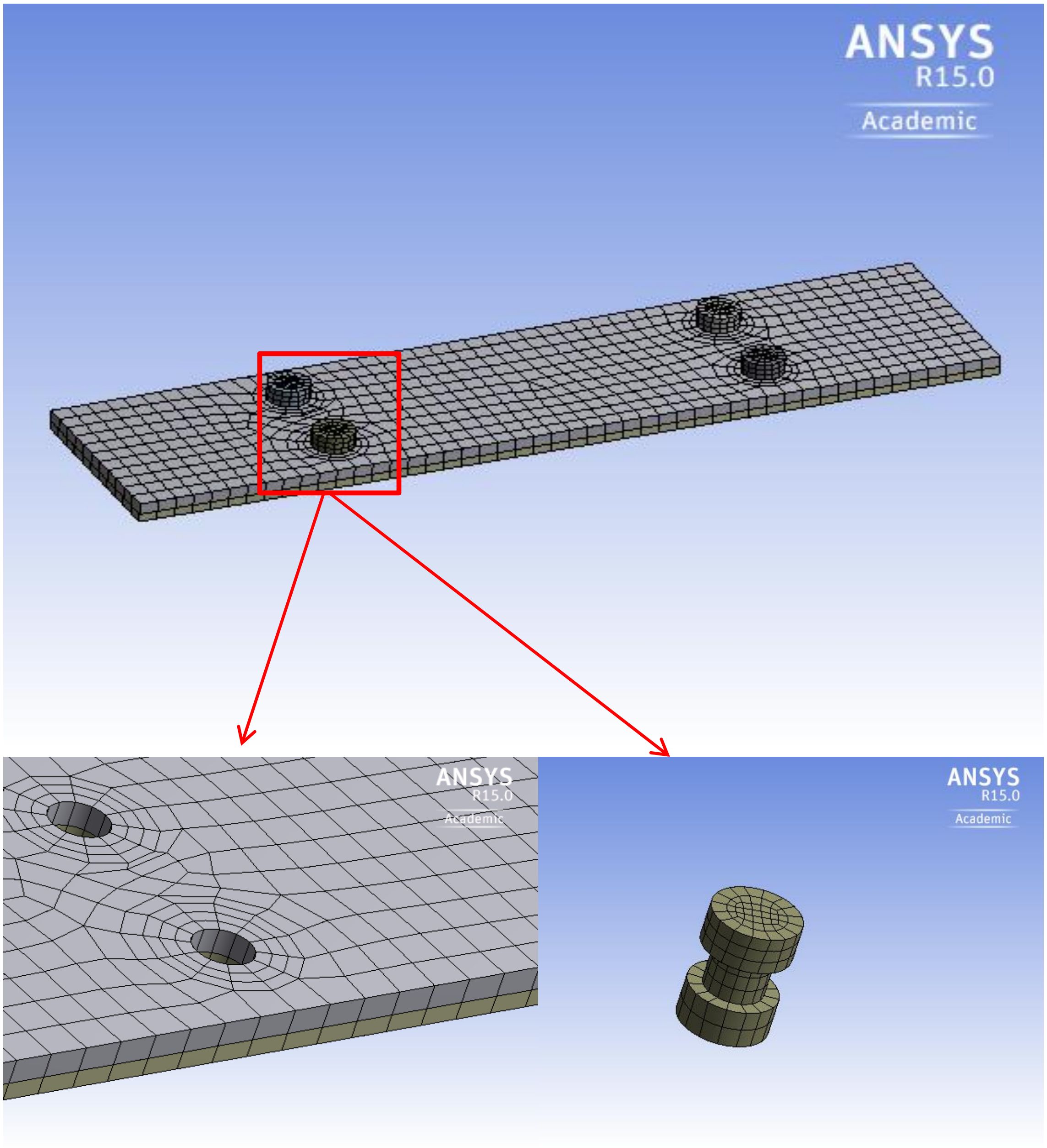

Figure 5.3: Bolted Attachment FEA Model Mesh

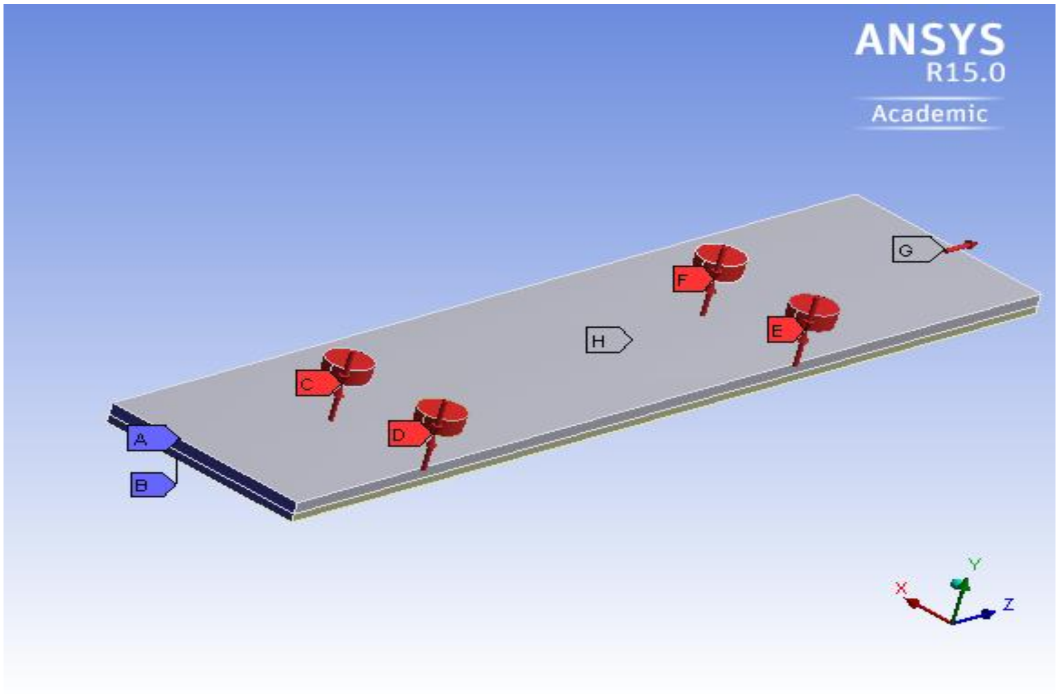

Figure 5.4: Pretensioned Bolted SMA Retrofit (External Loading) FEA Model

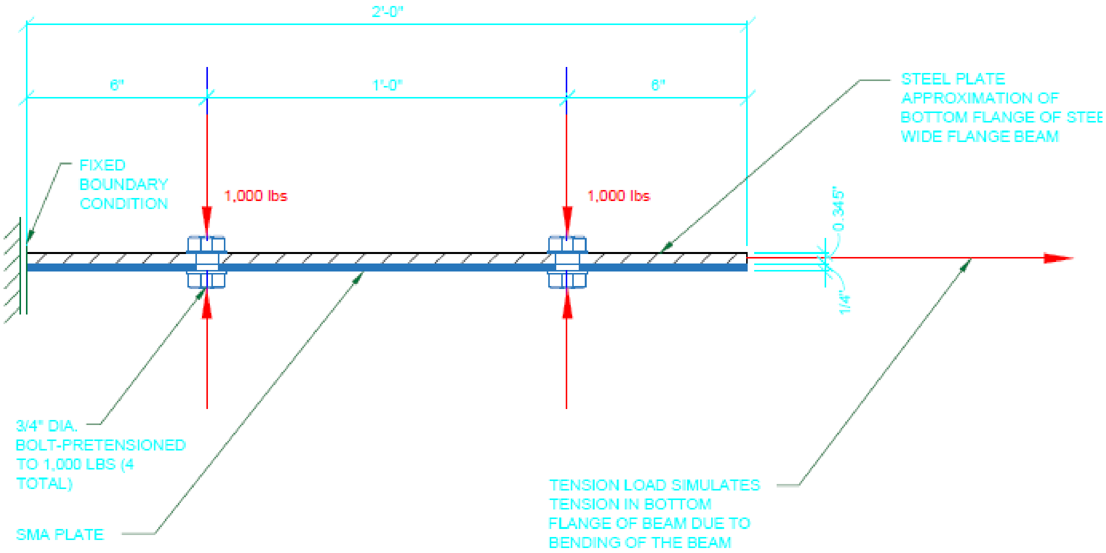

Figure 5.5: Pretensioned Bolted SMA Retrofit Model (External Load)

Table 5.1: External Loading Model Boundary Conditions

Boundary Conditions							
Boundary Condition	**Geometry Application**	**Displacement**			**Loading (lbs)**		
		x-axis	**y-axis**	**z-axis**	**x-axis**	**y-axis**	**z-axis**
A	Face	Fixed	Fixed	Fixed	---	---	---
B	Face	Fixed	Fixed	Fixed	---	---	---
C	Bolt Assembly	Free	Free	Free	---	1,000	---
D	Bolt Assembly	Free	Free	Free	---	1,000	---
E	Bolt Assembly	Free	Free	Free	---	1,000	---
F	Bolt Assembly	Free	Free	Free	---	1,000	---
G	Face	Free	Free	Free	---	---	10,000
H	Face	Free	Fixed	Free	---	---	---

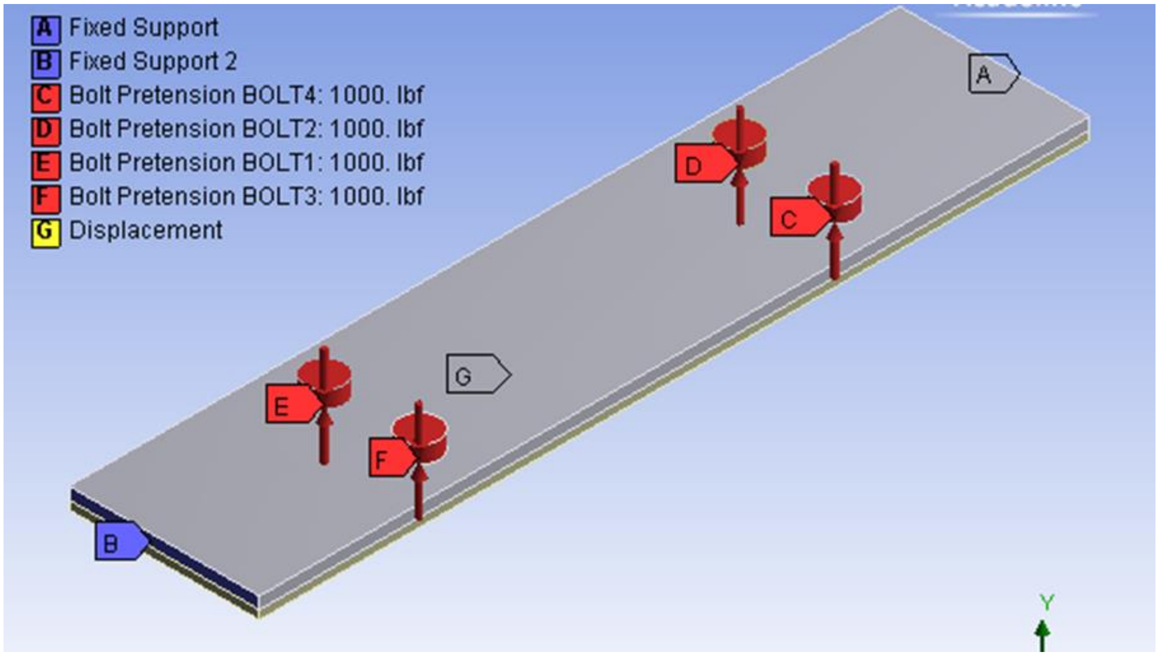

Figure 5.6: Pretensioned Bolted SMA Retrofit FEA Model (SMA Actuation) FEA Model

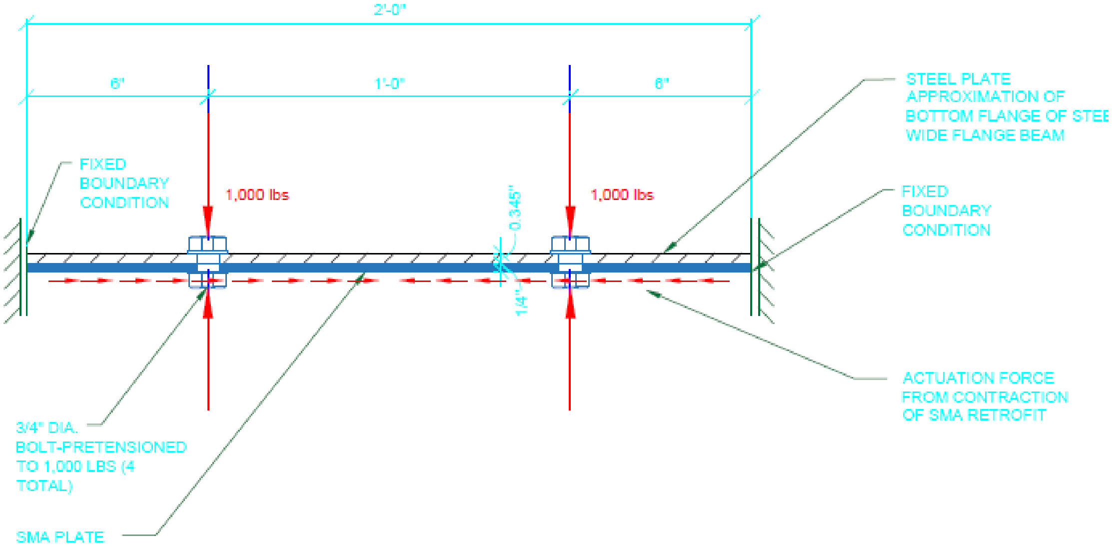

Figure 5.7: Pretensioned Bolted SMA Retrofit Model (SMA Actuation)

Table 5.2: SMA Actuation Model Boundary Conditions

Boundary Conditions							
Boundary Condition	**Geometry Application**	**Displacement**			**Loading (lbs)**		
		x-axis	**y-axis**	**z-axis**	**x-axis**	**y-axis**	**z-axis**
A	Face	Fixed	Fixed	Fixed	---	---	---
B	Face	Fixed	Fixed	Fixed	---	---	---
C	Bolt Assembly	Free	Free	Free	---	1,000	---
D	Bolt Assembly	Free	Free	Free	---	1,000	---
E	Bolt Assembly	Free	Free	Free	---	1,000	---
F	Bolt Assembly	Free	Free	Free	---	1,000	---
G	Face	Free	Fixed	Free	---	---	---

The boundary conditions for the externally loaded model are shown in Figure 5.4 and described in table 5.1. Boundary condition A and B provides a fixed condition at the end of the model where both the beam bottom flange and the SMA retrofit are not allowed to translate. Boundary conditions C, D, E and F provide bolt pretensioning load to each bolt assembly. Boundary condition G provides a pulling force at the opposite end of the beam flange. This creates normal tension stress along the beams bottom flanges z-axis which is indicative of the tension stress created in the bottom flange during beam bending. Since the pulling force is applied to only the beam bottom flange and not the SMA retrofit, an eccentric loading is created causing the model to displace (y-axis direction) away from the normal (z-axis) direction. Boundary condition H provides a zero displacement (y-axis) condition along the bottom face of the model. This allows the model to displace only along the normal (z-axis) direction. The model parameters are shown below in Table 5.1.

The boundary conditions for the actuation model are similar, but have both ends of the beam flange fixed while the SMA retrofit is left free to translate. The boundary conditions A and B are applied to each end face of the steel plate. The SMA plate is not fixed as in the externally loaded model since the SMA is needed to translate when caused to actuate. This actuation is simulated through simulated thermal strain which has been discussed in chapter 3 section 3.3.2 of this thesis for the general finite element model that simulated the actuation of shape memory alloy. The elastic modulus of detwinned martensite, indicated in the conclusions of chapter 4, is used as well as a 4% actuation strain for the general material properties of the SMA used in these simulations.

The pretension load of 1,000 lbs was arbitrarily selected to a level for which a sufficient clamping force would be expected to produce friction bonding between the two surfaces. When this pretension is compared to actual structural connected pretensioned applications the bolt pretension loads range from 18 kips to 28 kips for 5/8” bolts and 3/4” bolts. For this application a low value was chosen as a simple benchmark from which to compare to the non-pretensioned model used as a control.

The tension load of 10,000 lbs, applied to the steel plate, was selected with considerations for being a large enough value to be practical & appropriate for a typical tension load induced at the bottom flange of a steel wide flange beam subjected to uniform bending while being low enough to not induce yielding of the steel. The 10,000 lbs tension load at the bottom flange for the 8’-0” long W16x26 wide flange beam is can be back calculated to a uniformly distributed load of 1,667 lbs per foot.

5.2.2. Model Results

The initial thought for the effectiveness of the retrofit attachment was that the pretensioned bolted assembly would be a less effective attachment method compared to the unrealistic pure bonded attachment. The results shown in Table 5.3 show that the initial prediction is true in regards to the attachment effectiveness. The displacement (External Loaded Model only) of the bonded model versus the bolted model is significantly less, which can be expected. However, the prediction is inaccurate in respect to the effective stress applied to the beam flange (SMA Actuation Model only).

Table 5.3: Bolt Pretension Model Results

Bolt Pretension Model Results			
	Displacement (inch) (External Loaded Model)	**Tension Stress (psi) (External Loaded Model**	**Compression Stress (psi) (SMA Actuation Model)**
Control (bonded)	0.0025682	3,056	-20,341
Bolted (pretension)	0.0032978	3,466.20	-25,370
Bolted Control (no pretension)	0.0033642	3,503.30	-25,353

The results presented above show three models involved in the simulations. The first model is the control which models the purely bonded condition. The second is the bolted assembly with pretensioned bolts, which promotes a friction element to the connection through a clamping force. The third is the bolted assembly control which has bolts with no pretension.

The displacement results indicate the displacement at the tensioned end of the steel plate for the externally loaded model shown in Figure 5.4 & Figure 5.5. The bonded control model has less displacement since the SMA is totally bonded to the beam flange. The bolted assembly with pretension has more displacement than the bonded model since the SMA is not bonded to the beam flange and some slip between the two surfaces occurs. The bolted assembly, however, has less displacement than the bolted assembly without pretension. This is because the pretensioning of the bolts promotes a frictional bond between the surfaces, while the bolted assembly without pretension relies entirely on the studded action of the bolts.

The tension stress shown in Table 5.3 is the recorded stress, at the cross section shown in Figure 5.10, for the externally loaded model. The compression stress shown in Table 5.3 is the recorded stress, at the cross section shown in Figure 5.10, for the SMA actuation model.

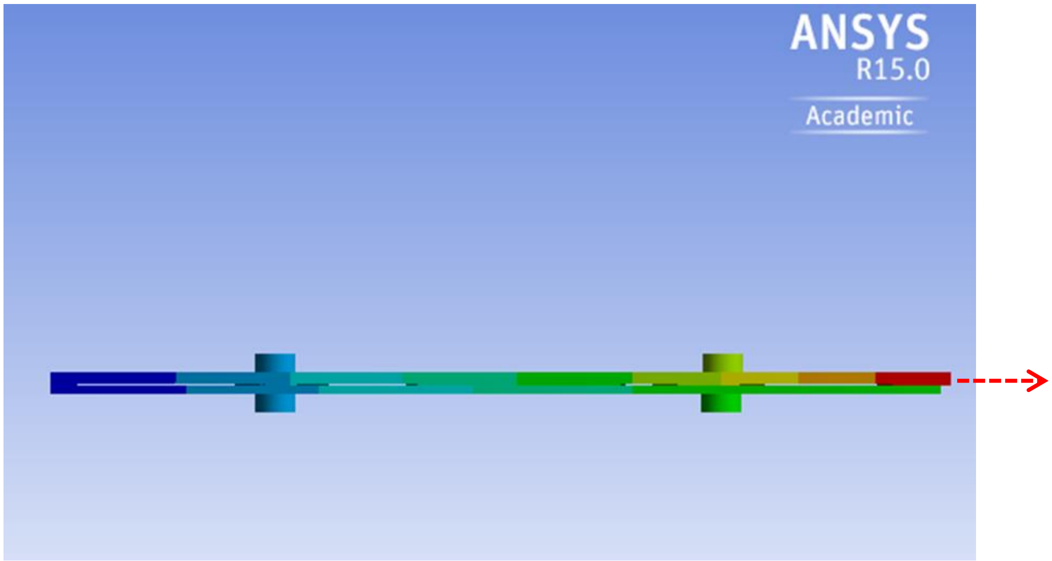

Figure 5.8: Tension (External Load) Model

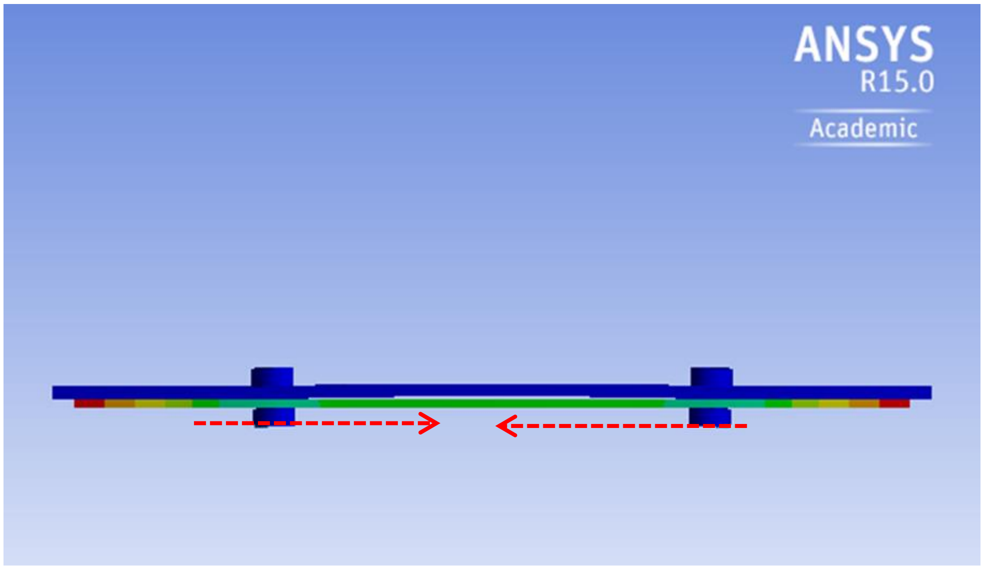

Figure 5.9: Compression (SMA Actuation) Model

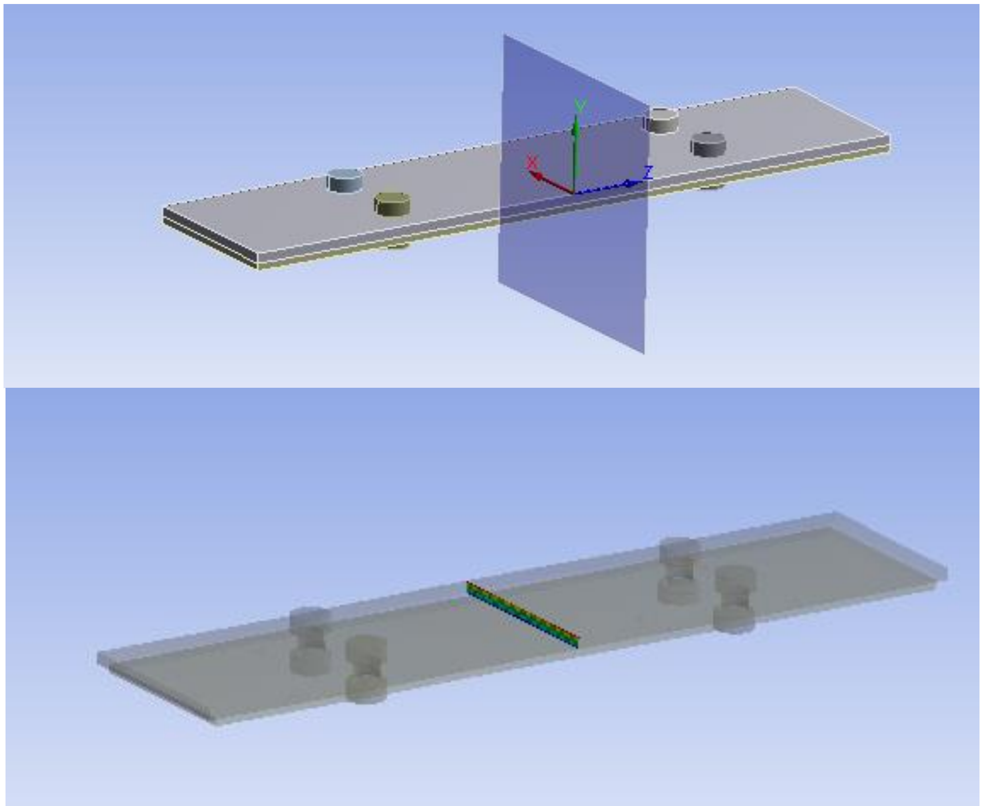

Figure 5.10: Location of Recorded Stress

The tension stress recorded at the cross sectional area shown in Figure 5.10, indicates the average tension stress at that location during external loading of one end of the model. The ideal bonded (control) model has less stress at this location when compared to the bolted assembly models regardless of pretension or no pretensioned bolts. The bolted assemblies have greater displacement since they have to bond the retrofit to the steel through friction force and studded action. It follows than that the bolted assemblies would have greater tension stress in this simulation because less load is transferred to the SMA since it is not as adequately attached as that of the bonded attachment and is susceptible to slip. This simulation also shows an informal verification of the pretension bolt model since the non-pretension model has greater tension stress and displacement than the pretension bolt model which tentatively indicates that the pretension bolt model most likely had been simulated successfully since it looks as if the frictional element of the pretension model allows for less translation of the steel.

The compression stress recorded at the cross section, indicates the average compression stress at that location during the actuation of the SMA retrofit (SMA actuation model). The results show that the compression stress is greater with the bolted assemblies than the ideal bonded (control) model. This is contrary to the initial thought that the bolted assembly with pretension would promote less stress transfer in the beam flange. It can be speculated that the studded action of the bolts during the actuation of the SMA creates a greater force along the beam flange than the continuously bonded surface actuation of the bonded SMA. This result is significant since what was thought to be a less effective way to transfer stress from the SMA retrofit to the steel may be in fact just the opposite.

It can be tentatively concluded that the pretensioned bolted assembly promotes greater stress transfer in regards to the SMA retrofit during actuation. Although this is true, with the results shown in this simulation, the anchorage ability of the pretensioned bolted assembly is still less effective than a purely bonded retrofit when considering the composite action of the two materials when subjected to mechanical loading (bending, tension, compression etc.). With this in mind the bonded models from here on out shall be used for simplicity and shall be considered conservative in regards to stress transfer, but not conservative for the composite action of the steel SMA retrofit

5.3. Shape Memory - Structural Applications

5.3.1. Structural Beam Shape Memory Retrofit

The first application that is explored involves the use of shape memory alloys as an active retrofit for structural steel beams by utilizing its shape memory effect abilities. The effects of the SMA active retrofit on the beam is explored through considering the effects of the retrofit on a static beam, involving pre-stress and pre-camber influences on the beam, and the effects of the retrofit on the overall capacity of the section during a loading scenario. As discussed in Section 5.1 the actuation ability of the SMA is modeled through thermal strain for which the material model having a modulus of elasticity of the detwinned martensite phase. Also as discussed in Section 5.2, the attachment of the retrofit is simplified through a perfectly bonded attachment.

5.3.1.1. FEA Model

The model parameters for the actuating retrofit beam models consist of an 8’-0” beam span with a ¼” x 3 ¾ ” x 7’-0” long shape memory alloy actuating retrofit centered on the beam bottom flange. 8 different structural wide flange beams are analyzed in this application, varying from 4 inches in depth to 21 inches in depth (table 5.4). Each beam is analyzed for pre-stress camber caused by the initial actuation of the SMA retrofit and for final net downward deflection during a two point loading condition. Boundary conditions are representative of a pinned-pinned simple span beam. The model set up is similar to the model shown in Figure 5.1 but without the pretensioned bolted attachment of the retrofit and the uniform load.

The geometry consists of extruded solids models of the particular wide flange beam shape and the retrofitted plate meshed with quadrilateral elements. The material models consist of typical structural steel and shape memory alloy with the shape memory effect approximated by thermal strain of the SMA in the detwinned martensite phase, which was previously discussed in chapter 3 section 3.3.2 for the general SMA finite element model. The detwinned martensite elastic modulus used for these beam retrofit simulations is based upon the elastic modulus found through material testing discussed in the conclusions of chapter 4. The meshing and contact models are meshed at 1” to 1 ½” depending on the beam size and the contact surface are also meshed at 1” to 1 ½” depending on the beam size. The contact type between the steel and the SMA retrofit is modeled as a completely bonded connection. This connection models the beam as a completely composite section for which the contact interface between the steel and the SMA does not open or slide in any direction.

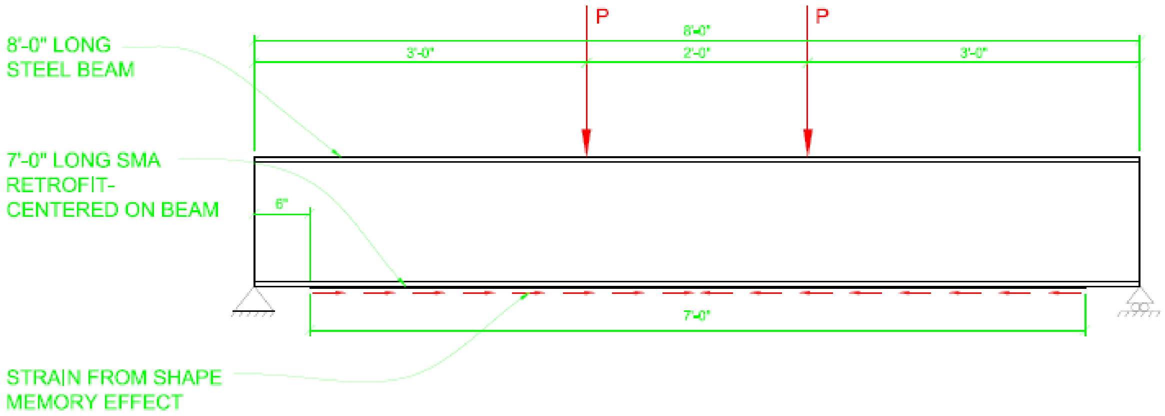

Figure 5.11: Beam/SMA Retrofit Boundary Conditions

The model is analyzed at the mid-span of the beam and the two point load arrangement maintains a sufficient way of applying a moment at the mid-span of the beam while not accruing unwanted stress concentrations, where analysis recording takes place. The model, being modeled as a complete 3-dimensional model, has to have boundary conditions that reflect a 3-D environment. This is done by fixing the axial rotation of the beam, which prevents the beam from having torsional displacement at the supports. The basic boundary conditions and forces are shown in Figure 5.11 & Figure 5.12. The loading scheme follows two load steps. The first load step is the pre-stress caused by the SMA retrofit actuation. The second load step is the external loading of the beam while the actuation strain remains.

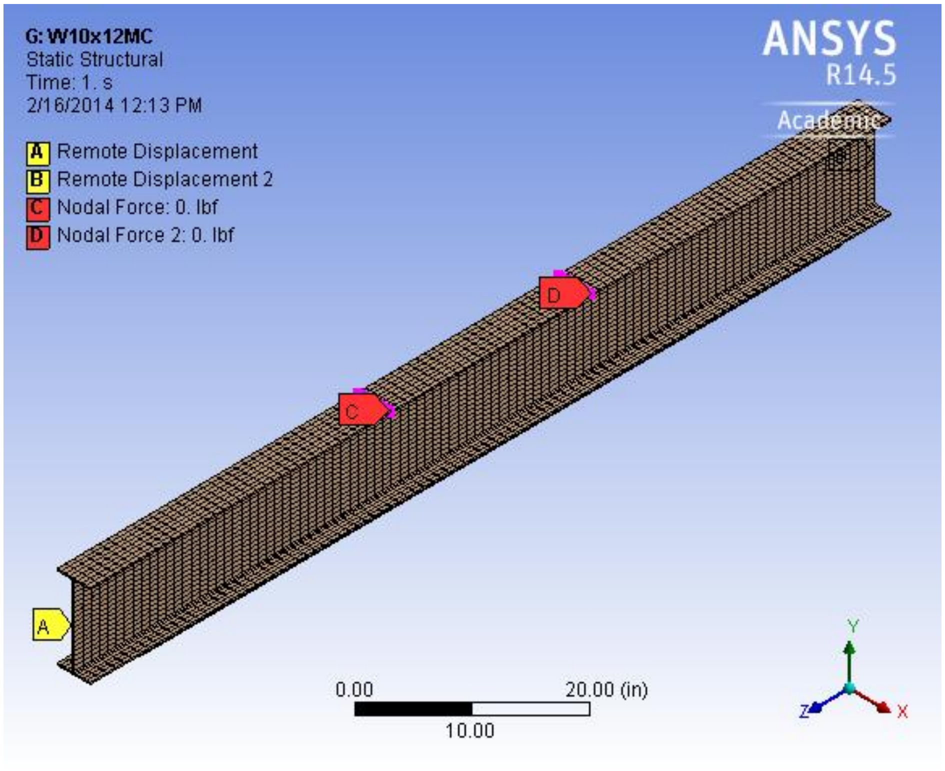

Figure 5.12: 3-D Boundary Conditions of Beam/SMA Retrofit

5.3.1.2. Load Step 1 – SMA Retrofit Actuation

Applying the actuation strain of the SMA retrofit to the bottom of the beam results in a pre-stressing and cambering of the beam. This camber is recorded at the mid-span of the beam. The amount of camber is compared to the moment of inertia of the section. This can give some relationship to the amount of camber expected for a particular section.

This pre-stressing mechanism caused by the SMA retrofit actuation can also be summarized in a general mechanical equation that simplifies the axial actuation into an equivalent distributed load along the bottom of the beam.

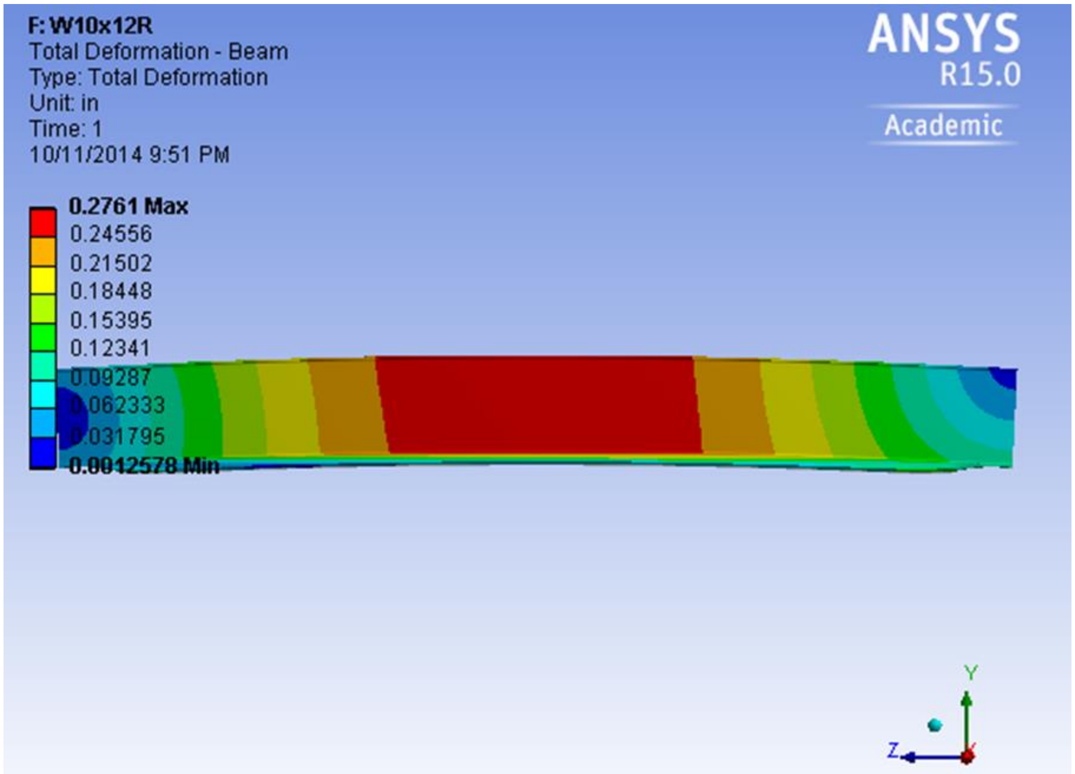

Figure 5.13: Beam Actuating Retrofit Load Step 1

5.3.1.3. Load Step 2 – External Loading

External loading of the steel beam model shows the amount of capacity increase that the SMA actuating retrofit offers to the particular beam size. The capacity is calculated through the elastic section modulus of the beam rather than the plastic section modulus of the beam. AISC Chapter F for the Design of Members for Flexure uses the plastic section modulus for its calculations, but in the case of this finite element analysis the yield moment is used for the beam capacity comparison.

The capacity of the section is measured through the top flange of the beam. As the far very top extents of the beam flange begin to yield the capacity is reached. This is compared to the control beam section for which the capacity is simply the section modulus multiplied by the yield stress. For these models the yield stress of the steel is 50 ksi.

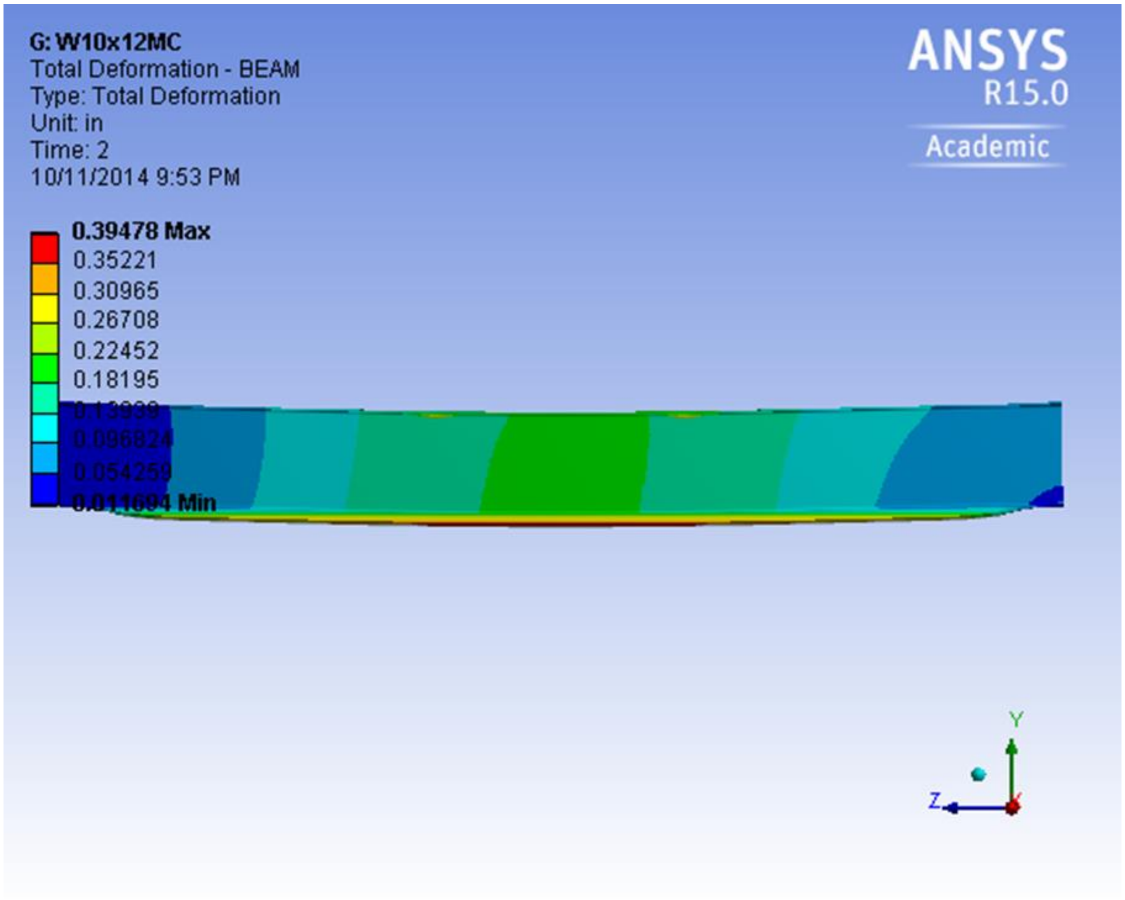

Figure 5.14: Beam Actuating Retrofit Load Step 2

5.3.1.4. FEA Model Results

Table 5.4: Beam Actuating Retrofit Results

Beam Size	**Beam Depth "d" (in)**	**Moment of Inertia I_x (in^4)**	**M_A(k-ft)**	**δ_A(in)**	**δ_P(in)**	**δ_{Total}(in)**	**$\delta_{ANSYS-A}$(in)**	**$\delta_{ANSYS-Total}$(in)**
W4x13	4.16	11.3	13.20	0.55677	-0.8969	-0.3401	0.57318	-0.32528
W8x10	7.89	30.8	25.03	0.38742	-0.3622	0.02521	0.38369	-0.000334
W10x12	9.87	55.8	31.31	0.26751	-0.2644	0.00314	0.27538	-0.021585
W12x14	11.9	88.6	37.75	0.20313	-0.2182	-0.0151	0.20279	-0.040231
W14x22	13.7	199	43.47	0.10412	-0.2409	-0.1368	0.10799	-0.18919
W16x26	15.7	301	49.81	0.07888	-0.2205	-0.1416	0.08138	-0.20264
W18x35	17.7	510	56.16	0.05249	-0.2054	-0.1529	0.05476	-0.22376
W21x44	20.7	843	65.67	0.03714	-0.1812	-0.1441	0.03919	-0.22279

5.3.1.5. Model Verification

In order to test to the validity of the finite element model results shown in table 5.4 an example problem showcasing this simulation with hand calculations is presented. These calculations are compared to the finite element results. The overall testing results for various beam sizes are present above in Table 5.4.

Example calculations for W8x10 wide flange beam:

Load Step 1: SMA Actuation

SMA Actuation Force

$F_{SMA} = \sigma A_{SMA} = E_{SMA}\varepsilon_A A_{SMA} = 2{,}030{,}500 \times 0.04 \times 0.9375 = \mathbf{76,144\ lbs}$

$E_{SMA} = 2{,}030{,}500\ psi$

$\varepsilon_A = 0.04$

$A_{SMA} = 3\ 3/4" \times 1/4" = \ 0.9375"$

Moment at Supports

$M_A = F_{SMA} \times e = 76{,}144 \times 3.945 = 300.4\ kip - in = \mathbf{25.03\ kip - ft}$

$e = d/2$

$d = 7.89"$

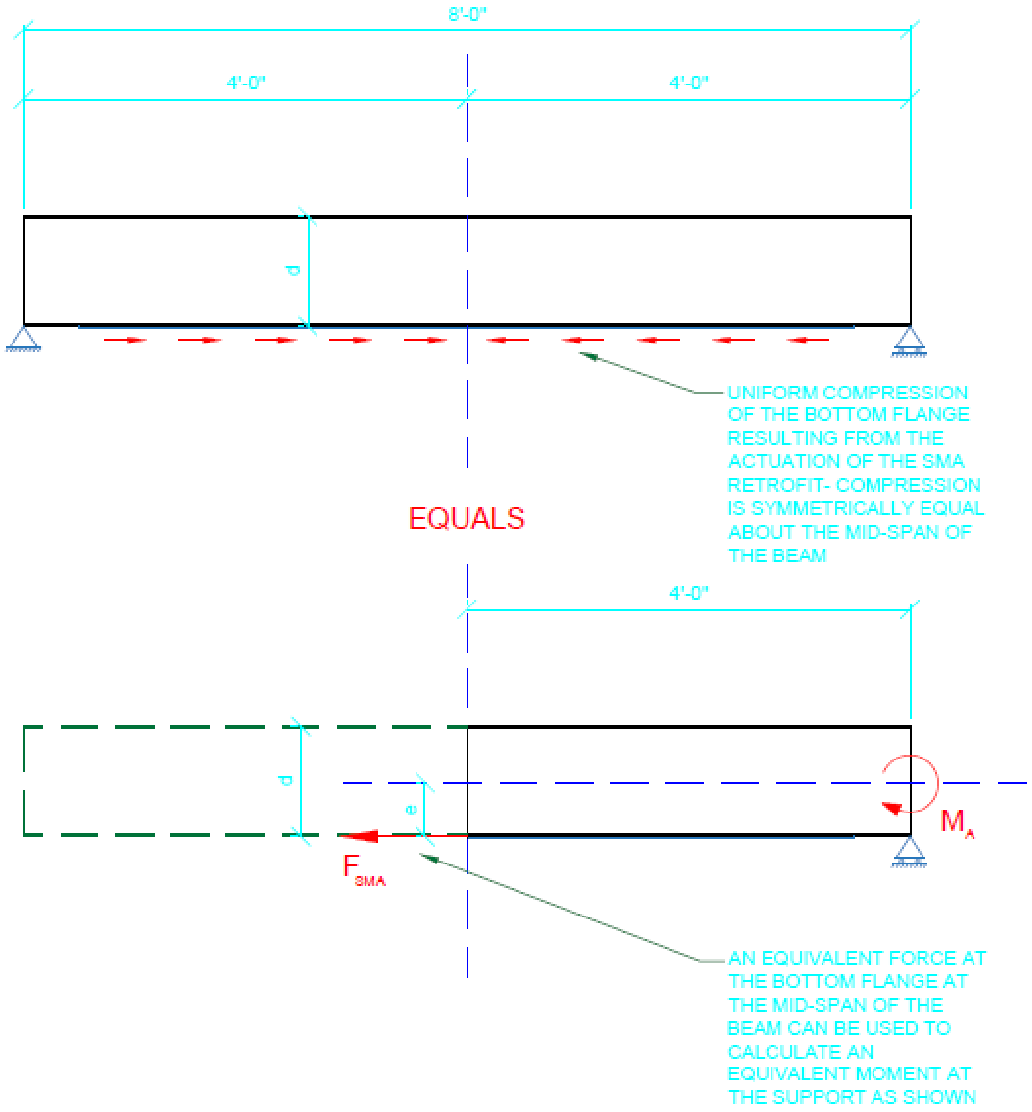

UNIFORM COMPRESSION OF THE BOTTOM FLANGE RESULTING FROM THE ACTUATION OF THE SMA RETROFIT- COMPRESSION IS SYMMETRICALLY EQUAL ABOUT THE MID-SPAN OF THE BEAM

AN EQUIVALENT FORCE AT THE BOTTOM FLANGE AT THE MID-SPAN OF THE BEAM CAN BE USED TO CALCULATE AN EQUIVALENT MOMENT AT THE SUPPORT AS SHOWN

Figure 5.15: Equivalent Loading Considerations for Hand Calculations

Beam Camber through SMA Actuation

$$\delta_A = \frac{MLx}{6EI}\left(1 - \frac{x^2}{L^2}\right), x = \frac{L}{2} \Longrightarrow \frac{M\frac{L^2}{2}}{6EI}\left(1 - \frac{\left(\frac{L}{2}\right)^2}{L^2}\right) = \frac{ML^2}{12EI}\left(\frac{3}{4}\right)$$

$$= \frac{ML^2}{16EI} \times 2\ for\ moments\ at\ each\ end\ of\ beam = \boldsymbol{\frac{ML^2}{8EI}}$$

Derivation:

With equal & opposite moments each support the internal moment at any length x along the beam will be equal to the support moment.

$$M_{int.} = M_{support} \Rightarrow EI\frac{d^2y}{dx^2} = M$$

$$EI\frac{dy}{dx} = Mx + C_1$$

$$@\ support\ A: x = 0, y = 0$$
$$C_2 = 0$$
$$@\ support\ B: x = L, y = 0$$
$$C_1 = -\frac{ML}{2}$$
$$EIy = \frac{Mx^2}{2} + C_1x + C_2 \xrightarrow{becomes} EIy = \frac{Mx^2}{2} - \frac{MLx}{2}$$

$$@\ x = \frac{L}{2}\ slope\ is\ zero \Rightarrow EIy = \frac{ML^2}{8} - \frac{ML^2}{4} = -\frac{ML^2}{8} \Rightarrow \boldsymbol{y = -\frac{ML^2}{8EI}}$$

$$\delta_A = \frac{ML^2}{8EI} = \frac{(25.03 \times 12)(8 \times 12)^2}{8(29{,}000)(30.8)} = \mathbf{0.38739}" \Uparrow$$

$$\delta_{ANSYS-A} = 0.38369" \Uparrow$$

Load Step 2: External Loading of Beam

W8x10 Moment Capacity

$$M_n = M_p = F_yZ_x = 50 \times 8.87 = 443.5k - in \Rightarrow 36.96\ k - ft$$

$$F_y = 50\ ksi$$

$$Z_x = 8.87\ in^3$$

$$L_b = 96"$$

$$L_p = 1.76 r_y \sqrt{\frac{E}{F_y}} = 35.64"$$

$r_y = 0.841"$

$E = 29{,}000\ ksi$

$$L_r = 1.95 r_{ts} \left(\frac{E}{0.7F_y}\right) \sqrt{\frac{Jc}{S_x h_o}} \sqrt{1 + \sqrt{1 + 6.76\left(\frac{0.7F_y}{E}\frac{S_x h_o}{Jc}\right)^2}} = 102.7"$$

$r_{ts} = \sqrt{\frac{\sqrt{I_y C_w}}{S_x}} = 1.0144"$

$I_y = 2.09 in^4$

$C_w = 30.9 in^6$

$S_x = 7.81 in^3$

$J = 0.0426 in^4$

$h_o = 7.69"$

$c = 1.0$

$L_p < L_b < L_r$

$$M_n = C_b \left[M_p - \left(M_p - 0.7F_y S_x\right)\left(\frac{L_b - L_p}{L_p - L_r}\right)\right] \le M_p \Rightarrow \boldsymbol{M_n = 345.65k - in} \Longrightarrow \boldsymbol{28.8\ k - ft}$$

$C_b = 1.190476\ for\ the\ particular\ 4 - point\ bending\ scenario$

Concentrated Load Required to Reach Moment Capacity

$$P = \frac{M}{a} = \frac{345.65}{36} = \boldsymbol{9.601\ kips}$$

Deflection under Load P

$$\delta_P = \frac{Pa}{24EI}(3L^2 - 4a^2) = \frac{9.601(36)}{24(29{,}000)(30.8)}(3(96)^2 - 4(36)^2) = \mathbf{-0.36221}" \Downarrow$$

Total Deflection

$$\delta_{Total} = \delta_A + \delta_P = \mathbf{0.02521}"$$

$$\delta_{ANSYS-Total} = -0.00033401$$

Moment at Calculated Total Deflection

$$M_\delta = P_\delta a = \frac{\delta_{Total}(696{,}000)}{(808{,}704)}(36) = 30.982\delta_{Total}I_x = 30.982(0.02521)(30.8)$$

$$= 24.06k - in = \boldsymbol{2.0047k - ft}$$

$$P_\delta = Equivalent\ force\ at\ total\ deflection\ (\delta_{Total})$$

$$P_\delta = \frac{\delta_{Total}(24EI)}{a(3l^2 - 4a^2)} = \frac{\delta_{Total}I_x(696{,}000)}{(808{,}704)}$$

$a = 36”$

$l = 96”$

Moment Capacity %

$$M_{\%} = \frac{M_\delta}{M_n} = \left[\frac{2.0047}{28.8}\right]100 = \mathbf{6.96\%}\ \boldsymbol{Capacity}$$

Table 5.4 and the hand calculations presented above show that the finite element model mimics the traditional beam analysis results with the SMA actuation approximated by an applied moment at each end of the beam. The camber calculated by hand δ_A=0.38739 in and the camber witnessed through the finite element simulations $\delta_{ANSYS-A}$=0.38369 in are rather close therefore the ANSYS model can be concluded to be a sufficient approximation of the effects of the SMA retrofit actuation on a steel beam. On the other hand the downward deflection caused by the external loading of the beam, while the beam is pre-stressed using the SMA retrofit, is slightly different at large beam sizes.

5.3.2. Structural Column Shape Memory Retrofit

The application of shape memory alloys, in this section, involves utilizing the pseudoelastic or superelastic characteristic of the material. The shape memory alloy is used as a structural reinforcement for structural columns and components subjected to high temperatures. A shape memory alloy retrofit at room temperature does not offer much reinforcement for structural steel since the modulus of elasticity is much lower than that of steel (see figure 5.17). At elevated temperatures however steel begins to degrade rather quickly in terms of yield stress and modulus of elasticity. Shape memory alloys, having a wide range of different alloys, offer high transformation temperatures for some specially made alloys. These high temperature shape memory alloys have transformation temperatures higher than 100°C (212°F). A specific alloy arrangement selected for these experimental applications is Nickel Titanium Palladium alloys (NiTiPd). The metallurgy of shape memory alloys is rather sensitive to the elemental ratios of the alloy so the specific alloy ratio used for the applications is $Ni_{19.5}Ti_{50.5}Pd_{30}$ and has an austenite start temperature of around 500°F and an austenite finish temperature of around 600°F. This specific shape memory alloy arrangement is taken from “Properties of a $Ni_{19.5}Ti_{50.5}Pd_{30}$ High Temerature Shape Memory Alloy in Tension and Compression” by Noebe, Padula II, Bigelow, Rios, Garg and Lerch.

This specific high temperature shape memory alloy is used since the austenite finish temperature is the temperature around which most steels begin to degrade rapidly. The intent of utilizing high temperature SMA is to begin reinforcing the steel as it beings to degrade. It is not the transformation characteristics of the material that is of interest however, but rather the great increase in material properties that the austenite phase offers. These applications ignore the actuation of the material and concentrates on the pseudoelastic capabilities. The models presented for the column retrofit reinforcing take into account a twinned martensite initial material phase. This means that the shape memory alloy is not deformed hence full actuation strains, as in the beam retrofit models, do not occur. Partial deformation does occurs because of the phase change from twinned martensite to austenite but for the simplicity reasons these actuation strains are not considered for these models. High temperature material properties for both steel and shape memory alloy materials used in these applications are presented in Figures 5.16 and 5.17. Properties for shape memory alloy are from reference presented above ("Properties of a $Ni_{19.5}Ti_{50.5}Pd_{30}$ High Temerature Shape Memory Alloy in Tension and Compression" by Noebe, Padula II, Bigelow, Rios, Garg and Lerch.) and properties for steel are referenced from the AISC Steel Construction Manual Table A-4.2.1 for properties of steel at elevated temperatures. The column shape used in all column buckling scenarios is a W8x35 consisting of A36 steel (F_y=36ksi).

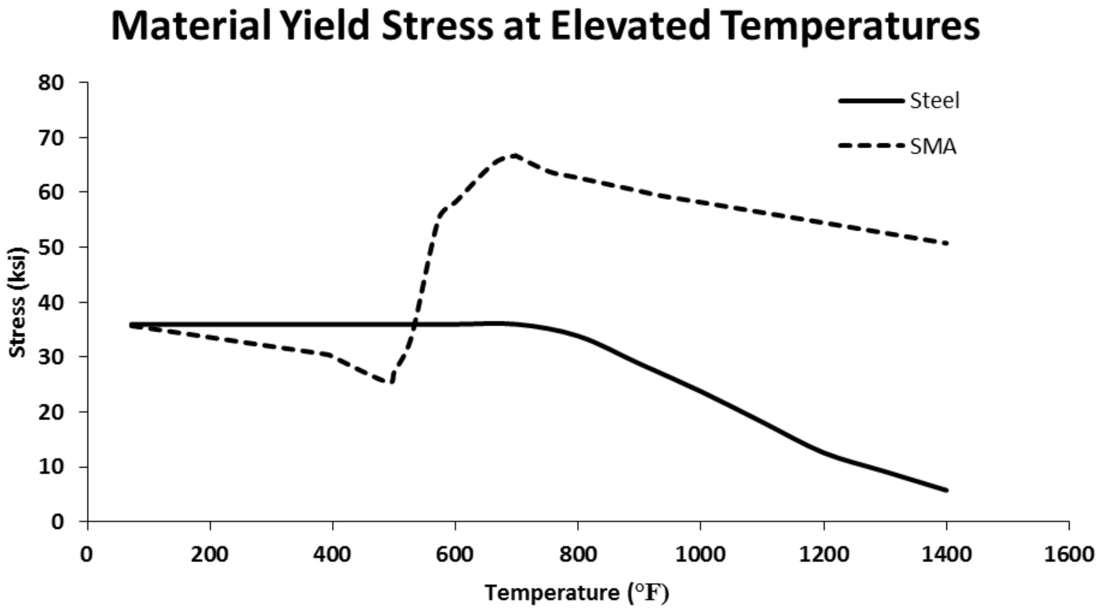

Figure 5.16: Material Yield Stress at Elevated Temperatures

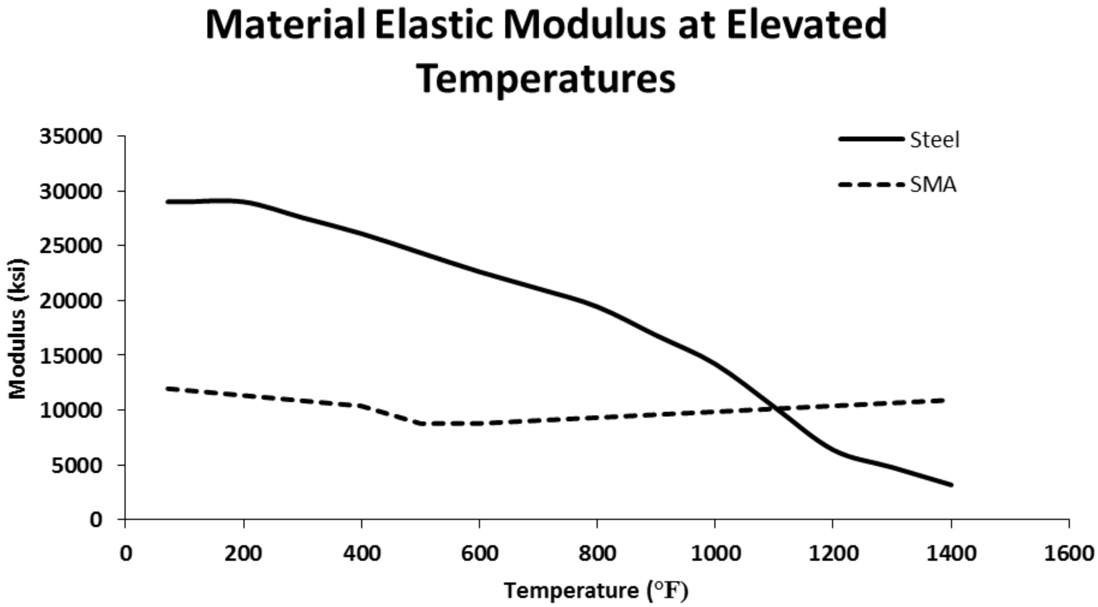

Figure 5.17: Material Elastic Modulus at Elevated Temperatures

The comparison of yield strength of A36 steel and NiTiPd (SMA) is similar at room temperature, but at around 700°F the yield strength of steel begins to degrade rapidly. To counter this, NiTiPd (SMA) is able to achieve complete transformation from martensite to austenite at around 600°F, for which grants the material a large increase in yield strength. The yield strength of NiTiPd is taken as the beginning of the material detwinning. As the steel begins to degrade mechanically the increased material properties of the NiTiPd SMA retrofit at the austenite phase offers a replacement for the loss mechanical abilities of the steel.

The elastic moduli of A36 steel and NiTiPd SMA are rather different at room temperature than at higher temperatures, as shown in Figure 5.17. The elastic modulus of steel decreases rapidly starting around 200°F, but the elastic modulus of NiTiPd SMA remains rather constant with some increase after complete austenite transformation is achieved. The typical range of ambient temperatures for a building fire ranges from 1000°F to around 1800°F. The point at which the elastic modulus of steel and NiTiPd SMA are the same occurs shorting after 1000°F and it is at this point that the NiTiPd SMA can prove to be beneficial in terms of the elasticity of the steel. For structural applications the elastic modulus controls greatly the buckling characteristics of main structural members as well as crucial structural components. This section explores the benefits that NiTiPd SMA may have on buckling capacity and pure yield strength of main structural members and components subjected to elevated temperature scenarios. Steel properties at elevated temperatures are provided through AISC Specifications Appendix 4 Table A-4.2.1 for Properties of Steel at Elevated Temperatures.

5.3.2.1. General Model and Concepts

A W8x35 steel wide flange column with ¼” thick NiTiPd SMA continuous retrofit is analyzed for linear buckling capacity at increasing temperatures. The SMA retrofit is continuously bonded to the outside of both column flanges. Buckling of wide flange columns occurs in the weak axis and the retrofit acts as weak axis reinforcing. The effective column height is 19’-0” for which a pinned-pinned linear buckling analysis is conducted.

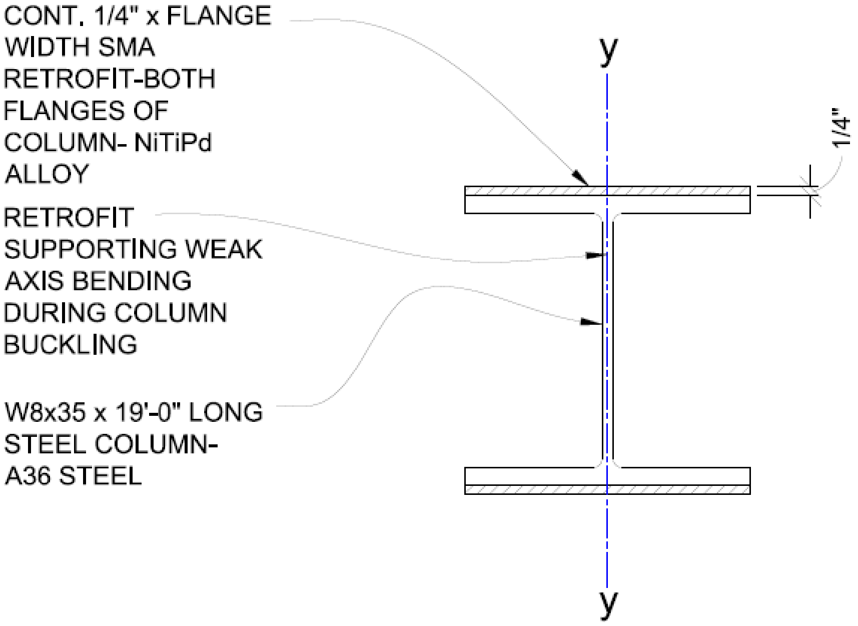

Figure 5.18: Steel Column with SMA Retrofit Detail

The composite retrofitted column can be represented by an equivalent section in respect to the higher elastic modulus between the two materials. In this case the elastic modulus of steel is greater than NiTiPd SMA, so an equivalent section of steel material can be calculated. This is done by determining the ratio between the modulus of steel and the modulus of NiTiPd SMA at various temperatures. The modulus ratio ($\boldsymbol{E_{Ratio}}$), from the transformed section, can be used to reduce the SMA retrofit plate to a smaller equivalent steel plate with the same stiffness in terms of modulus and section properties. This equivalent steel plate represents the overall effect of the SMA retrofit on the steel column by transforming its sectional contributions into a steel representative. This also helps for easier calculations and analysis.

This concept is rather useful for analyzing the steel column for increasing temperature consideration. The rising temperatures change the properties of both materials significantly and this equivalent section can help to determine crucial buckling properties of the column. It also helps to validate the linear elastic buckling finite element model. The equivalent sectional properties of the SMA retrofitted steel column in respect to increasing temperature are shown in Table 5.5.

Table 5.5: Temperature Dependent Equivalent Sectional Properties

W8x35 Retrofit Equivalent Sectional Properties															
Sectional Property	T=room No Retrofit	T=room	T=100	T=200	T=300	T=400	T=500	T=600	T=700	T=800	T=900	T=1000	T=1100	T=1200	T=1300	T=1400
t_f	0.495	0.598	0.597	0.593	0.594	0.594	0.585	0.592	0.603	0.615	0.638	0.669	0.741	0.902	1.052	1.351
b_f	8.02	8.02	8.02	8.02	8.02	8.02	8.02	8.02	8.02	8.02	8.02	8.02	8.02	8.02	8.02	8.02
t_w	0.310	0.310	0.310	0.310	0.310	0.310	0.310	0.310	0.310	0.310	0.310	0.310	0.310	0.310	0.310	0.310
d	8.12	8.33	8.32	8.32	8.32	8.32	8.30	8.31	8.34	8.36	8.41	8.47	8.61	8.93	9.23	9.83
S_y	10.62	12.83	12.80	12.71	12.73	12.75	12.55	12.70	12.92	13.19	13.68	14.34	15.89	19.35	22.56	28.97
Z_y	16.09	19.41	19.37	19.24	19.26	19.29	18.99	19.22	19.55	19.95	20.68	21.67	24.00	29.19	34.00	43.63
I_y	42.58	51.44	51.34	50.98	51.05	51.12	50.33	50.94	51.82	52.90	54.84	57.49	63.72	77.59	90.45	116.19
r_y	2.03	2.09	2.09	2.09	2.09	2.09	2.08	2.09	2.09	2.09	2.10	2.11	2.13	2.16	2.18	2.21
A_g	10.29	11.80	11.79	11.72	11.73	11.74	11.60	11.71	11.87	12.08	12.44	12.93	14.09	16.68	19.08	23.88
E_{STEEL}	29000	29000	29000	29000	27550	26100	24360	22620	21073	19430	16820	14210	10295	6380	4785	3190
E_{SMA}	---	11966	11829	11344	10860	10376	8785	8799	9065	9330	9596	9862	10128	10393	10659	10925
E_{RATIO}	---	0.4126	0.4079	0.3912	0.3942	0.3976	0.3606	0.3890	0.4301	0.4802	0.5705	0.6940	0.9837	1.6290	2.2276	3.4247
t_{SMA}	---	0.25	0.25	0.25	0.25	0.25	0.25	0.25	0.25	0.25	0.25	0.25	0.25	0.25	0.25	0.25
$t_{Equivalent}$	---	0.103	0.102	0.098	0.099	0.099	0.090	0.097	0.108	0.120	0.143	0.174	0.246	0.407	0.557	0.856

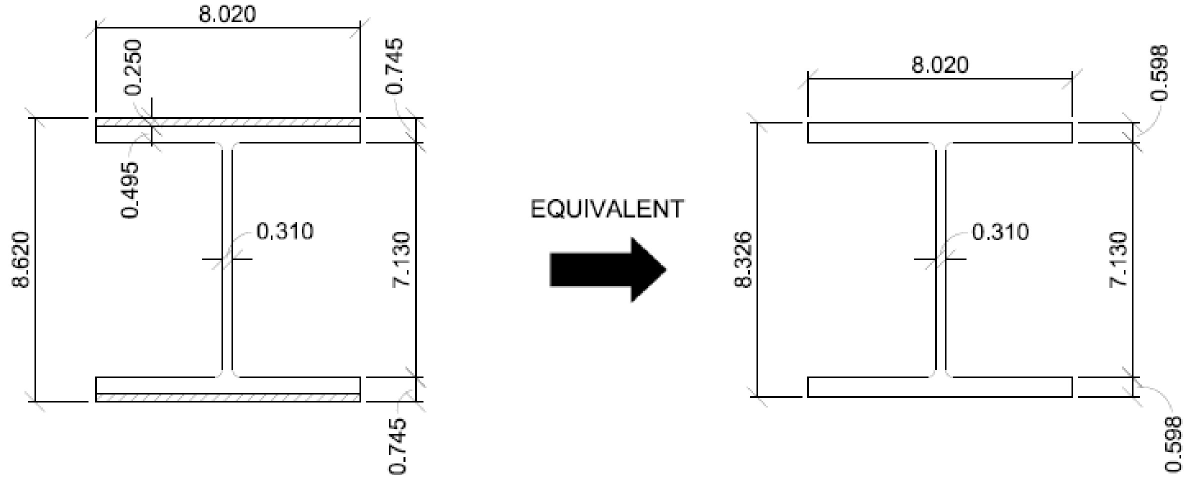

Figure 5.19: Equivalent Section Detail

The equivalent section properties can be utilized in finding the elastic buckling stress of the composite column for each temperature. The two main section properties that govern the equation is the radius of gyration and the elastic modulus.

$$\boldsymbol{F_e = \frac{\pi^2 E}{\left(\frac{KL}{r}\right)^2}}$$

The buckling stress (F_e), helps to validate the linear buckling finite element models presented in this chapter and helps to gain understanding into the buckling limits of the SMA retrofitted column at elevated temperatures.

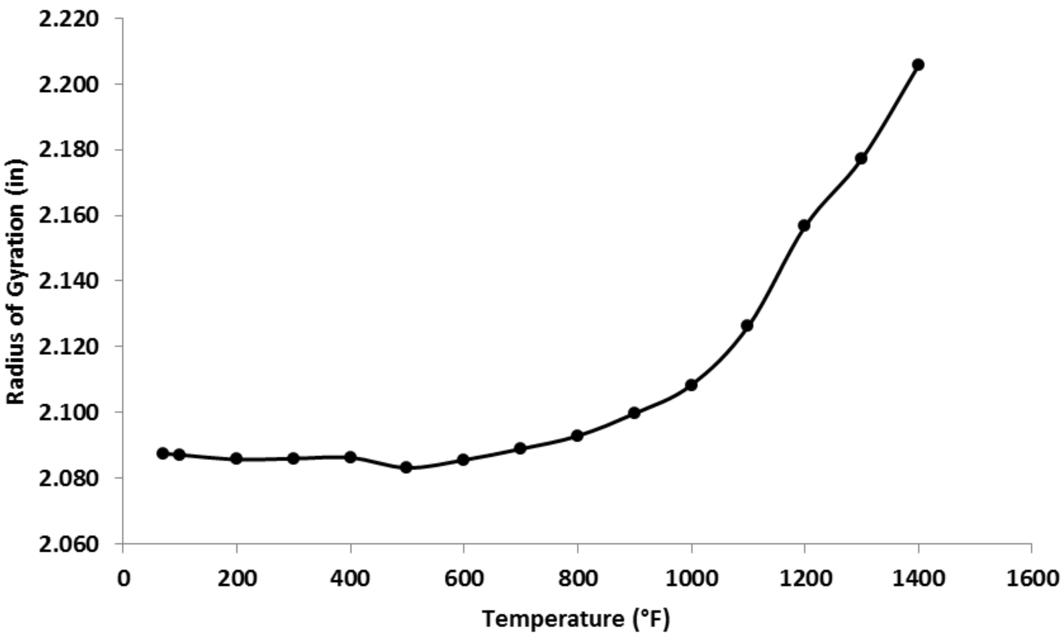

Figure 5.20: Radius of Gyration (Transformed Section) vs. Temperature

5.3.2.2. Finite Element Model and Analysis

The finite element model is similar to the actuation retrofit model presented in section 5.3.1. The geometry model incorporates an extruded wide flange section (W8x35 section) with extruded ¼" SMA continuous retrofitted plates. The total length of the geometry is 19 feet and the retrofit is continuous for the entire length of the column. The mesh model supports the simple bonded contact condition between the column and the retrofit and is meshed with quadrilateral elements distributed uniformly along the column.

A linear elastic buckling analysis is conducted for these simulations. This analysis simply interpolates the elastic buckling capacity of the giving geometry model in respect to applied external loads. For this simple column buckling scenario a 1 lb. axial load is applied to the top of the column. This load is allowed to be increased until the critical elastic buckling load is achieved. For the simple column model the critical buckling load can easily be calculated by hand, but in the interest of later more complicated models the finite element method can be rather useful in understanding critical buckling loads for not so simple structural component models.

The column boundary conditions applied are representative of a pinned-pinned column. The bottom of the column is fixed in all directions and fixed for axial rotation. The top of the column is fixed from perpendicular translation and fixed for axial rotation. The column is analyzed at temperatures ranging from room temperature (71.6°F) to typical building fire conditions of 1,400°F. The varying mechanical properties, shown in Figures 5.16 and 5.17, of both the steel column and the SMA retrofit are inputted into the material model at each temperature increment.

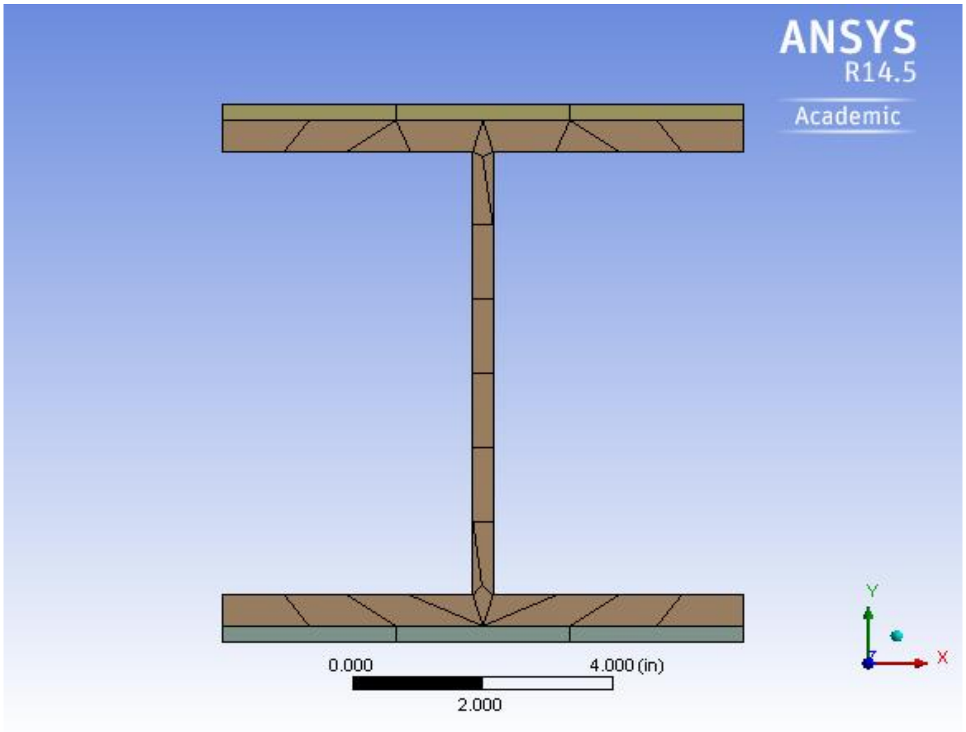

Figure 5.21: W8x35 Steel Wide Flange Column/SMA Retrofit FE Model

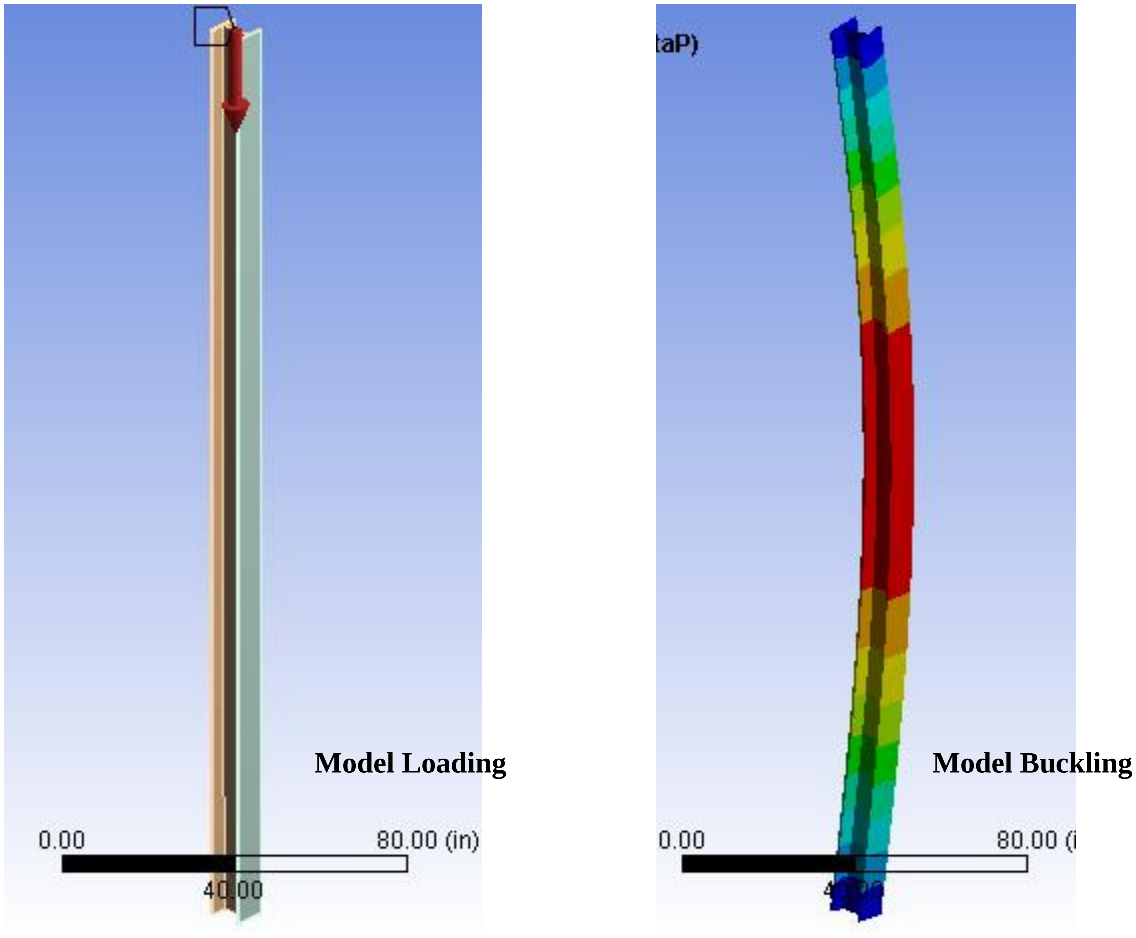

Model Loading **Model Buckling**

Figure 5.22: Finite Element Model (Loading and Buckling)

5.3.2.3. Simulation Results

The results show that the SMA retrofit provides a consistent benefit to the column as the temperature increases. Without taking into account the typical residual stress consideration that AISC Specifications takes into account, the purely elastic critical buckling loads are presented below. The results presented compare the critical buckling loads for the finite element SMA retrofitted column with the finite element control column (without SMA retrofit).

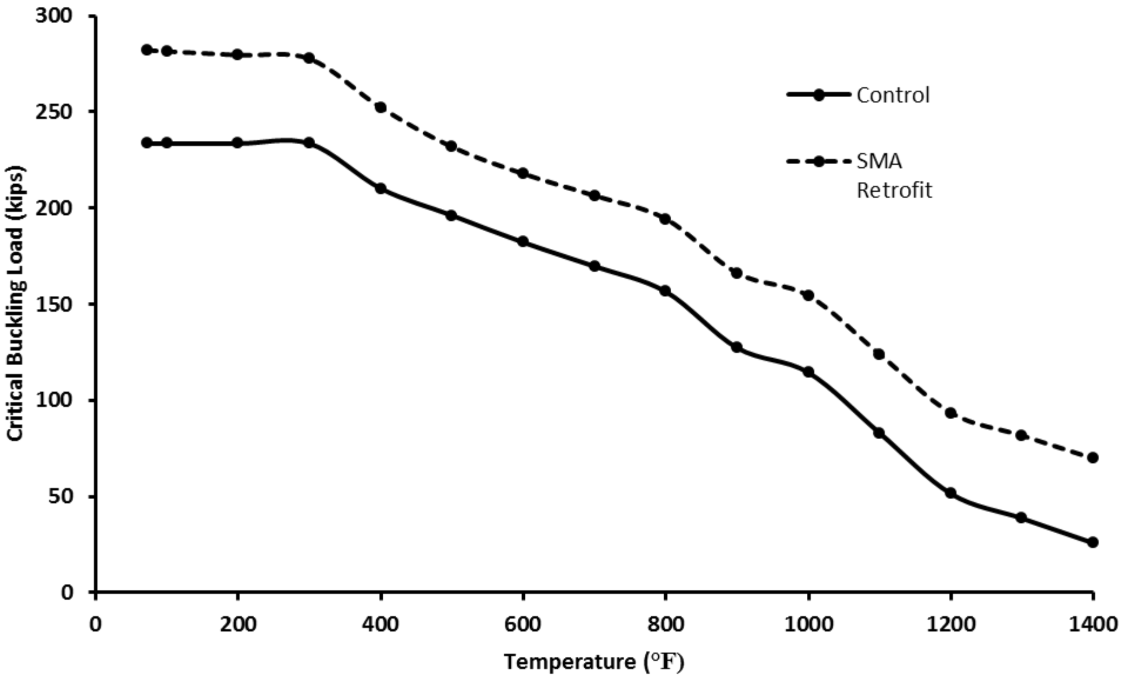

Figure 5.23: Elastic Buckling Critical Loads

A simple Euler buckling calculation for the critical buckling load for the W8x35 column is shown below. These calculations are presented for example purposes showing that the traditional Euler equations used to solve simple column buckling scenarios mimics the ANSYS finite element model of the SMA retrofitted steel column. The ANSYS simulation models both the SMA retrofit and steel column as separate materials. The hand calculations incorporate an equivalent steel section for the retrofitted column with respect to the material properties of the two materials. This equivalent section process is discussed earlier and can be seen in table 5.5.

Buckling Calculations for a SMA Retrofitted W8x35 (A36) Steel Column @ 1,100 °F

$W8x35$: $d = 8.12$, b_f=8.02", t_f=0.495, t_w=0.31",

$P_e = F_e A_g = \boldsymbol{124.55\ kips} \approx 123.91\ kips\ (ANSYS\ Results)$

$F_e = \frac{\pi^2 E_{Steel}}{\left(\frac{KL}{r}\right)^2} = \boldsymbol{8.8346\ ksi}$

$E_{Steel@1{,}100°\mathrm{F}} = k_E E_{Steel} = \boldsymbol{10{,}295\ ksi}$

$k_E\ from\ AISC\ Table\ A-4.2.1 = 0.355$

$E_{Steel} = 29{,}000\ ksi$

$K = 1.0$

$L = 19' \times 12" = 228"$

$r_y = \sqrt{\frac{I_y}{A_g}} = \boldsymbol{2.126}"$

$E_{SMA\ @\ 1{,}100°\mathrm{F}} = 10{,}127.6\ ksi$

$E_{Ratio} = \frac{E_{SMA}}{E_{Steel}} = 0.983739$

$t_{SMA} = 0.25"$

$t_{equiv.} = E_{Ratio} t_{SMA} = 0.245935"$

$t_{f-equiv.} = t_{SMA} + t_f = 0.740935"$

$d_{equiv.} = d + 2(t_{SMA}) = 8.611"$

$I_y = S_{y-eqiuv.}\left(\frac{b_f}{2}\right) = 15.89 in^3$

$b_f = 8.02"$

$$S_{y-equiv.} = \frac{{b_f}^2[d_{equiv.} - (d_{equiv.} - 2t_{f-equiv.})]}{6} + \frac{[b_{f-} - (b_f - t_w)]^3 (d_{equiv.} - 2t_{f-equiv.})}{6b_f}$$

$$A_g = 2(t_{f-equiv.} b_f) + t_w(d_{equiv.} - 2t_{f-equiv.}) = 14.094 in^2$$

The above calculations match the ANSYS results shown in figure 5.23 for each 100 degree temperature increment from room temperature to 1,400 °F. It can be concluded that the finite element buckling analysis produces results that mimic the traditional buckling analysis, using the equivalent section approach, very well. Euler critical buckling results of hand calculations and ANSYS simulations for each temperature increment are presented in table 5.6.

Table 5.6: Euler Critical Buckling Loads for Various Temperatures

	SMA Retrofit		P_e (Control Column no SMA Retrofit) (kips)
Temperature (°F)	P_e (ANSYS) (kips)	P_e (Hand Calculations) (kips)	
71.6	282.05	283.25	283.25
100	281.5	282.68	282.68
200	279.53	280.71	280.71
300	277.58	281.07	281.07
400	252.18	253.32	253.32
500	231.74	232.76	232.76
600	217.79	218.75	218.75
700	206.4	207.33	207.33
800	194.27	195.13	195.13
900	166.14	164.55	164.55
1000	154.38	155.11	155.11
1100	123.91	124.55	124.55
1200	93.418	93.98	93.98
1300	81.602	82.18	82.18
1400	69.7	70.37	70.37

5.3.3. Application Example

This example describes a situation where the SMA column retrofit serves as a means to prevent structural collapse during a high temperature building fire. The floor framing plan (Figure 5.24) shows a general floor framing layout for a 2 story building with interior columns terminating at the first floor and clear span roof members spanning the roof from grid A to grid C. The interior W8x35 wide flange column within the shaded area is analyzed using the dead and live loading scheme indicated below. This loading is typical of a conservative office loading which includes a variable partition dead load of 15 psf and a maximum live load of 100 psf. The effective height of the column is again 19’-0” as in section 5.3 and the column yield strength is 36 ksi which simulates an evaluation of an older structure.

The general scenario is that the existing building is being evaluated for an intended future use with the loads indicated in Figure 5.24. The existing columns, consisting of 36 ksi steel are deemed inadequate for the intended loading. The building plan is to have office space on the upper floor and laboratory space below. The laboratory space will be utilizing hazardous and extremely flammable materials and consideration for structural integrity during extreme fire conditions are of great importance. In order to strengthen the existing columns it has been suggested that the column flanges be retrofitted with additional steel plates to increase buckling capacity during normal loading conditions, it has also been suggested that an experimental, high temperature, shape memory alloy retrofit be used to increase buckling capacity of the column in the event of a building fire. The goal of this example situation is to analyze the column and compare the two retrofitting suggestions.

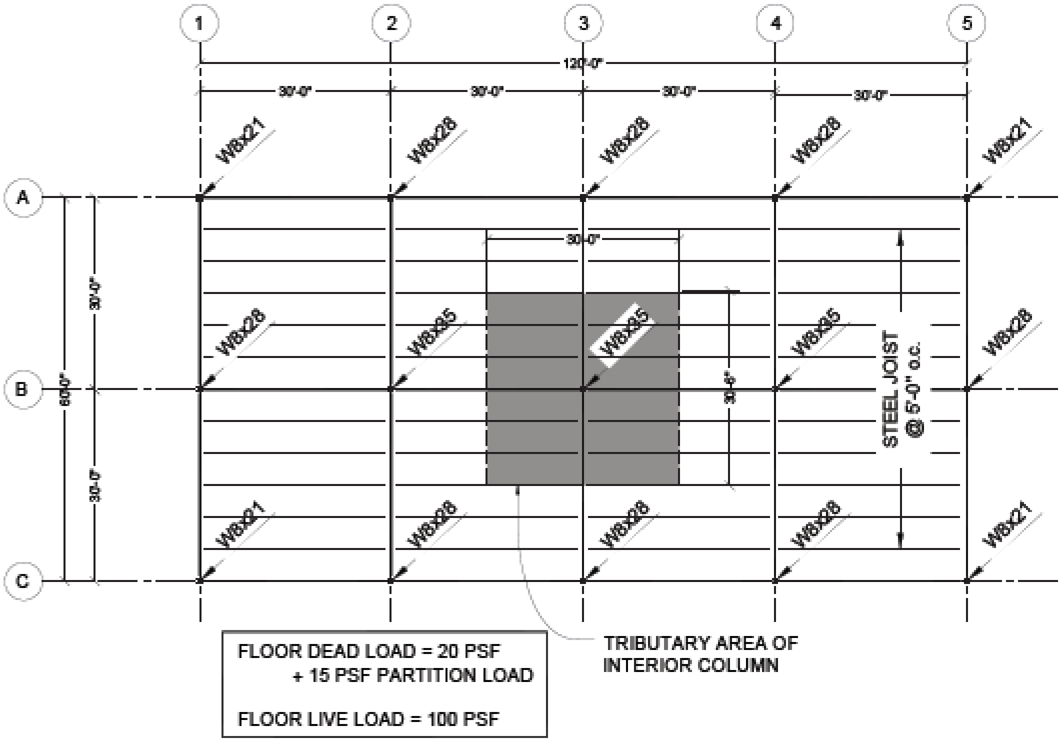

Figure 5.24: Floor Framing Plan

Evaluation Calculations and Results:

Existing W8x35 (36 ksi):

$\boldsymbol{AISC\ Section\ E3}$

$P_a = 135\, psf\ \times 900\, ft^2\ (trib. area) = \mathbf{121.5}\ \boldsymbol{kips}$

$P_n = F_{cr}A_g = 18.53\, ksi \times 10.3\, in^2 = \mathbf{190.86}\ \boldsymbol{kips}$

$$\frac{KL}{r} \leq 4.71\sqrt{\frac{E}{F_y}} \Rightarrow \frac{(1.0)(19ft \times 12\, in/ft)}{2.03\, in} = \mathbf{112.315}\ \boldsymbol{in} < 4.71\sqrt{\frac{29{,}000}{36}} = \mathbf{133.68}\ \boldsymbol{in}$$

$$F_e = \frac{\pi^2 E}{\left(\frac{KL}{r}\right)^2} = \frac{\pi^2(29{,}000)}{(112.315)^2} = \mathbf{22.689}\ \boldsymbol{ksi}$$

$$F_{cr} = \left[0.658^{F_y/F_e}\right]\left(F_y\right) = [0.658^{1.587}]36 = \mathbf{18.53}\ \boldsymbol{ksi}$$

$$\frac{\boldsymbol{P_n}}{\boldsymbol{\Omega}} \geq \boldsymbol{P_a} \Rightarrow \frac{\mathbf{190.86}}{\mathbf{1.67}} = \mathbf{114.29}\ \boldsymbol{kips} < \mathbf{121.5}\ \boldsymbol{kips}\quad (\boldsymbol{N.G.})$$

Existing W8x35 (36 ksi) with ¼" steel plate retrofit:

$\boldsymbol{AISC\ Section\ E3}$

$P_a = \mathbf{121.5}\ \boldsymbol{kips}$

$P_n = F_{cr}A_g = 19.54\ ksi \times 14.31\ in^2 = \mathbf{279.62}\ \boldsymbol{kips}$

$$\frac{KL}{r} \leq 4.71\sqrt{\frac{E}{F_y}} \Longrightarrow \frac{(1.0)(19ft \times 12\,in/ft)}{2.116\,in} = \mathbf{107.75}\ \boldsymbol{in} < 4.71\sqrt{\frac{29{,}000}{36}} = \mathbf{133.68}\ \boldsymbol{in}$$

$$F_e = \frac{\pi^2 E}{\left(\frac{KL}{r}\right)^2} = \frac{\pi^2(29{,}000)}{(107.75)^2} = \mathbf{24.652}\ \boldsymbol{ksi}$$

$$F_{cr} = \left[0.658^{F_y/F_e}\right](F_y) = [0.658^{1.46}]36 = \mathbf{19.54}\ \boldsymbol{ksi}$$

$$\frac{\boldsymbol{P_n}}{\boldsymbol{\Omega}} \geq \boldsymbol{P_a} \Longrightarrow \frac{\mathbf{279.62}}{\mathbf{1.67}} = \mathbf{167.44}\ \boldsymbol{kips} > \mathbf{121.5}\ \boldsymbol{kips} \quad (\boldsymbol{OK})$$

W8x35 (36 ksi) with ¼" SMA plate retrofit:

Using the equivalent section approach discussed in section 5.3 and taking into account the typical residual stress in wide flange members, the nominal strength (P_n) of the column with SMA plate retrofit is 226.79 kips. Please note that the SMA plate and the steel plate retrofits will not have residual stress the same as that of the actual column flanges. For the sake of the equivalent section approach the capacity of the retrofitted columns at room temperature will be calculated with the assumed residual stress for typical steel columns.

$$\frac{\boldsymbol{P_n}}{\boldsymbol{\Omega}} \geq \boldsymbol{P_a} \Longrightarrow \frac{\mathbf{226.79}}{\mathbf{1.67}} = \mathbf{135.8}\ \boldsymbol{kips} > \mathbf{121.5}\ \boldsymbol{kips} \quad (\boldsymbol{OK})$$

These results indicate that either retrofit method, be it SMA or steel, will increase the buckling capacity of the column enough to grant adequacy for the intended design loads. The retrofits are then compared at increasing temperatures to see if the column buckling capacity can be increased enough to be adequate during a potential building fire.

In order to compare the two retrofit methods at elevated temperatures the critical buckling loads (P_e) of the column are used. The retrofit material, be it SMA or steel, does not have residual stress consideration that the flanges of a typical wide flange column has, so it is not as simple as equating an equivalent section and applying the residual stress approach to column buckling. In the case of the SMA retrofit the yield stress of SMA at elevated temperature increases, so it can be predicted that the SMA grants more capacity to the column. Since this is difficult to attain the critical buckling load (P_e) is used.

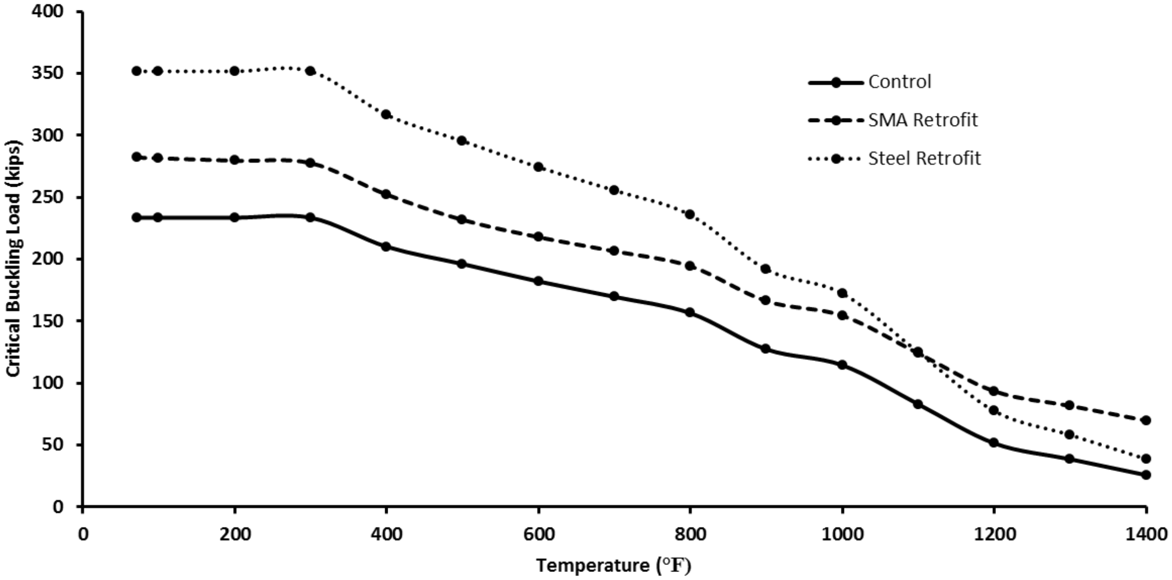

Figure 5.25: Critical Buckling Loads with Respect to Temperature

The results shown in Figure 5.25 show the three different column models and their critical (Euler) buckling loads (P_e) over a range of temperatures from room temperature (71.6°F) to 1,400°F. Both the SMA retrofit and steel retrofit initial increase, at room temperature, is substantial with the steel retrofit being significantly larger than the SMA retrofit. None the less, they both grant a large increase in buckling capacity to the column. Although, as the temperature increases the graph for the steel retrofit decreases faster than the SMA retrofit and at around 1,150°F becomes lower than the SMA retrofit. The final results are compared in Table 5.7. The design loads at elevated temperatures are modified to better simulate loading conditions at which the average building fire temperature reaches 1,400 °F. For a building fire to reach 1,400 °F the fire would have to be present for an extended period of time. It can be assumed that the initial design live load would not be fully present. The design live load for this simulation is 50 psf which is 50% of the intended live load. This is based upon the AISC Appendix 4.1.4. Load Combinations and Required Strength for fire conditions. This special load combination is used for the design of structural members for fire conditions and takes into account 50% of the total live load. The load combination is 1.2 dead load + 0.5 live load. In this case the total floor design load becomes 74 psf. With 900 square feet of tributary area contributed to the column the final applied load to the column during fire conditions is 66.6 kips. Also, it is important to note that the buckling loads, without reduction factors, are used in order to evaluate the point at which the column would theoretically fail and if the design load would indeed cause collapse of the structure or not.

Table 5.7: Application Example Results

	P_e		
	Control	**Steel Retrofit**	**SMA Retrofit**
Room Temp. (71.6°F)	233.52 kips	351.68 kips	282.05 kips
Fire Condition (1,400°F)	25.68 kips	38.68 kips	69.7 kips
Design Loads at Room Tempearture (P_a) = 121.5 kips			
Design Loads at 1,400°F (P_a) = 66.6 kips			

General knowledge, understanding and consideration of structural steel design for structures subjected to extreme (elevated) temperatures is taken from the following referenced materials: Agarwal and Varma (2011), Chen, Young and Uy (2006) and American Institute of Steel Construction (Steel Construction Manual: Thirteenth Edition).

CHAPTER 6. GENERAL SUMMARY & CONCLUSIONS

6.1. Mechanical Effectiveness

The overall effectiveness of piezoelectric actuators and shape memory alloys as stress mitigation mechanisms has been explored through a series of parametric studies and finite element simulations. The results and conclusions follow that the initial mechanical range can tell us a lot about the effectiveness of the material. Figure 2.1 in Chapter 2, illustrates the mechanical range in terms of strain versus stress present in the material during actuation. Piezoelectric actuators and shape memory alloys both have high actuation stress. The actuation stress is the amount of stress created with-in the material while actuation occurs.

One important difference between the two materials is that shape memory alloys have much larger actuation strains than piezoelectric materials do. When it comes to enacting the actuation stress onto a substrate surface the amount of actuation stress and the amount of actuation strain both play an important role in creating mechanical work with-in the substrate. The higher the combined actuation stress and actuation strain are the more mechanical work will be enacted on the substrate surface. In the long run the actuation stress does not have much to do with the amount of the stress enacted on a substrate, but rather it is the actuation strain combined with the stiffness of the material during actuation. The actuation stress is tied to the material stiffness through the elastic modulus of the material.

Through the simulations shown in this thesis it can be concluded that the mechanical effectiveness of shape memory alloy is far greater than that of piezoelectric material, primarily because of the high actuation strain. The shape memory alloys were able to enact high stresses within stiffer material simply because of the large strain associated with the material.

6.2. Implementation and Utilization

There are implementation limits for both shape memory alloys and piezoelectric material. Piezoelectric materials, as discussed in Chapter 2, are traditionally used in sensor applications for which the small strain can be easily recorded by the actuator as a sensor. In order to implement piezoelectric material as a structural enhancement mechanism, the application environment must be limited to small stress applications. This small amount of stress is quantified at about 2,000 psi to 3000 psi, seen through the parametric study conducted in chapter 3. One of the only structural applications that consider these small amounts of stress is wood construction. The typical wood member bending stress can range from 1,000 psi for typical dimension lumber to over 3,000 psi with engineered/manufactured lumber. Within this application the piezoelectric actuator can be used as a stiffening component as well as a sensor and response mechanism for countering non-consistent loads such as strengthening wind lateral support members.

Shape memory alloys, since they have higher actuation strains and can enact larger stresses on stiffer material than piezoelectric actuators, can be implemented in structural steel applications. Some of these applications are discussed in Chapter 5 of this thesis. Another benefit that shape memory alloys have is the large range of actuation temperatures. The building fire scenarios discussed in Chapter 5 are theoretically practical, but have some uncertainties in terms of implementation. These applications do not actually use the shape memory alloy as an actuator, but rather uses the increased stiffness at high temperatures to maintain structural stability during building fire conditions.

6.3. Conclusions

The general conclusions of this thesis are that both piezoelectric material and shape memory alloy are capable of enacting stress mitigation on structural substrates. The major difference as discuss before is the actuation strain exhibited by the material acting as an actuator. It has been concluded through finite element experimentation that shape memory alloys have significantly larger actuation strains than piezoelectric material. This does not rule out piezoelectric actuators as being effective stress mitigation mechanisms. Rather they can be possibly implemented in applications where structural member properties have lower failure stress (strength).

Shape memory alloys are theoretically sufficient in being effective stress mitigation mechanisms in larger structural applications where structural steel is involved. Through finite element analysis and implementation, it has been seen as rather effective in strengthening structural steel members. Although this may be true, there are many underlying factors that make the practical implementation of shape memory alloys difficult. Some examples of these things are the cost of retrofitting an entire column with two one quarter inch thick high temperature shape memory plate, the practicality of manufacturing a shape memory alloy this large and completely understanding the strain actuation of large scale shape memory alloy when compared to small scale for which was experimented on in Chapter 4.

Although both these materials have implementation problems they both are worthy of further exploration and experimentation. The applications discussed and show cased in the thesis, specifically the shape memory alloy applications, have potential to be effective applications for these materials.

REFERENCES

Agarwal, Anil. Varma, Amit H. "Design of Steel Columns at Elevated Temperatures Due to Fire: Effects of Rotational Restraints." *Engineering Journal* Fourth Quarter. (2011): 297-314. Print.

American Institute of Steel Construction, *Steel Construction Manual: Thirteenth Edition.* AISC: 2005. Print.

Bhalla, Suresh. Soh, Chee K. "Structural Impedance Based Damage Diagonsis by Piezo-Transducers." *Earthquake Engineering and Structural Dynamics* 32. (2003): 1897-1916. Web. Sept. 2014.

Cai, C.S. Wu, Wenjie. Chen, Suren. Voyiadjis, George. "Applications of Smart Materials in Structural Engineering." Department of Civil Engineering, Louisiana State University, Baton Rouge, Louisiana. 2003.

Chen, J. Young, B. Uy, B. "Behavior of High Strength Structural Steel at Elevated Temperatures." *Journal of Structural Engineering*. (2006): 1948-1954. Web. Sept. 2014.

Claeyssen, Frank. Letty, R. Le. Barillot, F. Sosnicki, O. "Amplified Piezoelectric Actuators Static and Dynamic Applications." *Ferroelectrics* 351. (2007): 3-14. Web. Nov. 2012.

DesRoches, R. Delemont, M. "Seismic Retrofit of Simply Supported Bridges using Shape Memory Alloys" *Engineering Structures* 24 (2002): 325-332. Web. April 2015.

El-Tawil, S. Ortega-Rosales, J. "Prestressing Concrete Using Shape Memory Alloy Tendons" *ACI (American Concrete Institute) Structural Journal* 101.6 (2004): 846-851. Web. April 2015.

Gaul, L. Lenz, J. Sachau, D. "Active Damping of Space Structures by Contact Pressure Control in Joints" *Mechanics of Structures and Machines: An International Journal* 26.1 (2007): 81-100. Web. 23 Mar. 2012.

Kamada, Takayoshi. Fujita, Takafumi. Hatayama, Takayoshi. Arikabe, Takeo. Murai, Nobuyoshi. Aizawa, Satoru. Tohyama, Kohtaro. "Active Vibration Control of Frame Structures with Smart Structures using Piezoelectric Actuators (Vibration Control by Control of Bending Moments of Columns)" *Smart Materials and Structures* 6 (1997):448-456. Web. 23 Mar. 2012.

Lagoudas, Dimitris C. Hartl, Darren J. Kumar, Parikshith K. Machado, Luciano G. Kiefer, Björn. Popov, Peter. Entchev, Pavlin B. Qidwai, M.A. Siddiq. *Shape Memory Alloys: Modeling and Engineering Applications.* New York: Springer Science+Business Media LLC, 2008. Print.

Li, Chunmei. *Elastic Properties and Phase Stability of Shape Memory Alloys from First-Principles Theory*. Doctoral Thesis. School of Industrial Engineering and Management, Department of Materials Science and Engineering, KTH, Sweden, 2011. Print.

Maji, Arup K. Negret, Ihosvany. “Smart Prestressing with Shape Memory Alloy.” *Journal of Engineering Mechanics* (1998): 1121-1128. Web. 10 May 2012.

Newman, Scott. *Active Damping Control of a Flexible Space Structure using Piezoelectric Sensors and Actuators.* Thesis. Naval Postgraduate School, Monterey, California. 1992. Print.

Nguyen-Van, N. Mai-Duy, N. Tran-Cong, T. “A Smoothed Four-Node Piezoelectric Element for Analysis of Two-Dimensional Smart Structures.” University of Southern Queensland, Engineering and Surveying, Toowoomba, Queensland, Australia. 2008.

Noebe, Ronald. Padula II, Santo. Bigelow, Glen. Rios, Orlando. Garg, Anita. Lerch, Brad. “Properties of a $Ni_{19.5}Pd_{30}Ti_{50.5}$High-Temperature Shape Memory Alloy in Tension and Compression.” *Smart Structures and Materials:Active Materials: Behavior and Mechanics.*(2006). Conference Presentation.

Ocel, J. DesRoches, R. Leon, R. Hess, W. Krummer, R. Hayes, J. Sweeney, S. “Steel Beam-Column Connections using Shape Memory Alloys*” ASCE Journal of Structural Engineering* 130.5 (2004): 732-740. Web. April 2015.

Piefort, Vincent. *Finite Element Modeling of Piezoelectric Active Structures.* Thesis. Active Structures Laboratory Department of Mechanical Engineering and Robotics ULB, Brussels, Belgium 2001. Print.

Song, G. Ma, N. Li, H.-N. “Applications of Shape Memory Alloys in Civil Structures.” *Engineering Structures* 28 *(*2006): 1266-1274. Web. May 2013.

Song, G. Olmi, C. Gu, H. “An Overheight Vehicle-Bridge Collision Monitoring System using Piezoelectric Transducers” *Smart Materials and Structures* 16 (2007): 462-468. Web. Feb. 2012.

Song, Gangbing. Kelly, Brian. Agrawal, Brij N. “Active Position Control of a Shape Memory Alloy Wire Actuated Composite Beam.” *Smart Materials and Structures* 9 (2000): 711-716. Web. 5 Oct. 2012.

Terriault, P. Viens F. Brailovski, V. “Non-isothermal Finite Element Modeling of a Shape Memory Alloy Actuator using ANSYS.” *Computational Materials Science* 36 (2006): 397-410. Web. May 2013.

Tichý, Jan. Erhart, Jiří. Kittinger, Erwin. Přívratská, Jana. *Fundamentals of Piezoelectric Sensorics-Mechanical, Dielectric, and Thermodynamical Properties of Piezoelectric Materials.* New York: Springer-Verlag Berlin Heidelberg, 2010. Print.

Tripathi, Prashant K. Gangadharan, K.V. "Design and Implementation of Active Vibration Control in Smart Structures." *International Journal of Research and Reviews in Mechatronic Design and Simulation* 2.1 (2012): 92-98. Web. May 2013.